Graphene on crystalline insulators: subsurface potentials and screening effects

Jones, Gavin

Award date:
2015

Awarding institution:
University of Bath

Graphene on crystalline insulators: subsurface potentials and screening effects

Gavin James Jones

A thesis submitted for the degree of Doctor of Philosophy

University of Bath
Department of Physics

October 2014

Contents

Acknowledgements

I would like to express my deepest appreciation to all those who provided me the opportunity to complete this report. I wish to thank my supervisor Dr. Adelina Ilie for all the help and guidance she has given me, and also Dr. Simon Crampin for his help with the theoretical side of the project. PhD students Ying Wu for her assistance with theoretical calculations, and Asieh Kazemi and Peter Lewis for their help with fabrication and measurement of graphene devices. Mick Philips and Chris Mulcahy from Asylum Research for their help and technical support with the Asylum Research AFM. I also want to thank the technical and administrative staff of the University of Bath Physics department for their support. A special thanks goes to my family and Charlene Edwardson for their love and support, making this thesis possible.

Abstract

In this work we examined the effect of localized electrostatic potentials generated by subsurface nanostructures on overlaid graphene layers of various thicknesses and the screening produced by such layers. Electrostatic Force and Kelvin Probe microscopies were used to investigate few-layer graphene (FLG) domains on top of ionic crystals. Step edges, pits and protrusions within the ionic surface create sizeable and local perturbations of the surface potential of graphene overlayers. These were within the tenth of eV range in FLG with up to three layers, and become considerably screened in thicker layers. A computational Thomas-Fermi model of screening by graphene layers was developed to specifically describe localized potential distributions (not modelled previously), and correlated successfully with the experimental results presented here, results from literature, as well as available ab-initio Density Functional Theory results. Engineering such nanostructures in a regular manner can allow the bottom-up creation of on-sheet p-n junctions and superlattices that exploit the Dirac nature of carriers in graphene, and provide a test bed for studying local screening.

Introduction, Aims and Thesis Outline

Motivation and Aims

Controlling and modulating the surface potential of the graphene sheet is important for producing on-sheet junctions and superlattices which are predicted to play an important role in building devices that exploit the novel Dirac nature of carriers in graphene, such as electron guides[1] different doping levels and, hence, surface potentials have to date been produced by electrostatic gates[2] top-down lithographic procedures. Other approaches based on exploiting the interaction with substrates with given symmetry and commensuration led to Moire superstructures and important associated effects, such as renormalization of group velocity of graphene electrons [3], anisotropic transport [4], or the emergence of new mini-Dirac cones [5].

To date graphene has been used in devices mostly in conjunction with amorphous insulators (e.g. SiO_2) on which it has been demonstrated that electron and hole puddles form [6]. These were found to strongly decrease carrier mobility. Only recently have atomically flat substrates such as boron nitride been employed in an attempt to improve carrier mobility [7]. Boron nitride was chosen in those works due to its weak, van der Waals interaction with graphene. Here we explore the opposite idea: we chose an atomically flat ionic substrate, whose interaction with graphene is based on short-range, local

electrostatic potentials, that can be sizeable and and which can be tailored through a variety of mechanisms.

This work investigates the effects on graphene overlayers of nanostructures within the surface of an ionic crystal. To our knowledge this has neither been proposed nor investigated previously. We show for the first time that naturally occurring steps, pits and protrusions create sizeable local perturbations within graphene overlayers, enabling the electrostatic potential and the doping level within the graphene sheet to be modulated at lateral length scales much smaller than can be obtained via lithographic processes. Such atomic scale structures can therefore offer the ultimate resolution of electrostatic patterning of graphene. Another crystalline, insulating substrate used with graphene, the covalently- bonded SiC, cannot provide such sizeable effects. Though ionic surfaces have the tendency to have significant water solubility due to their susceptibility to water (a polar molecule), work under controlled/inert environment and/or post annealing in vacuum can render these practical problems tractable. Our results were obtained with naturally occurring structures, but we propose that controlled atomic-scale engineering of ionic substrates, through a combination of electron/ion beam exposure [8] and stencilling [9], for example, can have practical importance towards the realization of atomically controlled superlattices and p-n junctions which are predicted to be instrumental in revealing and exploiting the Dirac physics of the graphene sheet.

Such ionic systems can also provide a test bed for the systematic study of local screening at the nanoscale within graphene, which is known to be complex on account of the unusual and strongly thickness-dependent electronic structure, with the vanishing density of states at the Dirac point resulting in significant non-linear effects and major impact from doping and thermal effects. Screening in graphene is currently a matter of debate even in the case of large equipotential graphene areas[10],[11] where a one-dimensional treatment is possible, whilst in our case the local electrostatic source means lateral variations are relevant[12] and need further atomic level investigations and special theoretical or computational implementations for modelling the screening.

We therefore implemented a computational model for screening by graphene layers using a Thomas-Fermi model for localized potential distributions, for which there is no analytical solution. The model allowed us to explore a large range of situations, such as doping and electron-beam supercollimators[13], or chemical functionalization[14]. Graphene regions with both strategies requiring complex regimes of graphene, wide range of external potentials (both regarding magnitude and types of distributions), and the role played by the electronic structure of multi-layered graphene films as opposed to considering these

systems as mere stacks of independent graphene monolayers. All these situations have not been treated theoretically previously. This model ultimately allowed us to estimate that the surface potential produced by the above mentioned ionic nanostructures within monolayer graphene overlayers can be sizeable, of about 0.3-0.4 eV, as well as to calculate the further screening that takes place in thicker layers.

Thesis Outline

The thesis is organized in the following chapters:

Chapter 1 gives the fundamentals of graphene physics, focusing on band structure, density of states, stacking order and effect of electric field on mono-, bi- and tri-layer graphene. This information is needed whilst implementing the computational modelling of screening by graphene layers.

Chapter 2 describes the methods applied for the identification of graphene films (by optical means and Atomic Force microscopy) laid on crystalline insulating substrates. These substrates are transparent and therefore identification methods that are suitable for the SiO_2/Si substrates are not useful any longer.

Chapter 3 presents sources of sizeable localized potential that can be generated by nanostructures of an ionic surfaces, considering both configurations that occur in vacuum as well as under atmosphere, in real environments.

Chapter 4 describes the techniques used for measuring the surface potential of the graphene films overlaid on crystalline ionic substrates, namely Electrostatic Force and Scanning Kelvin Probe microscopies (EFM and SKPM).

Chapter 5 presents the experimental measurements of such localized surface potentials, obtained above graphene layers of varying thickness, as well as in series of potential- distance dependencies.

Chapter 6 details the implementation of the computational Thomas-Fermi model of screening by graphene layers of localized potentials, which uses the experimental data to estimate the size of the local perturbation felt by the graphene electrons and produced by the nanostructured ionic surfaces.

List of publications and conference presentations covering this work

Gavin J. Jones, Ying Wu, Simon Crampin, and Adelina Ilie : A computational Thomas-Fermi model for screening of extended, localized potential distributions by graphene layers, in preparation.

Gavin J. Jones, Asieh Kazemi, Simon Crampin, Mick Phillips, and Adelina Ilie : Surface Potential Variations in Graphene Induced by Nanostructured Crystalline Ionic Substrates, **Applied Physics Express 5**, 045103 (2012)

Graphene 2012, 10-13 April 2012, Bruxelles (Belgium). Surface potential variations in graphene induced by nanostructured crystalline ionic substrates, G.J. Jones, A. Kazemi, Y. Wu, S. Crampin, and A. Ilie

Trends in Nanotechnology 2011, November 2011, Tenerife, Spain Surface potential variations in graphene induced by nanostructured crystalline ionic substrates, G.J. Jones, A. Kazemi, S. Crampin, and A. Ilie

Chapter 1

The electronic properties of graphene

This chapter presents the fundamentals of graphene physics, focusing on band structure, density of states, stacking order and effect of electric field on mono-, bi- and tri-layer graphene. This theory is needed whilst implementing the computational modelling of screening by graphene layers developed in Chapter 6.

1.1 Carbon bonding in graphene

Carbon exists in the ground state $1s^2 2s^2 2p_x 2p_y$, however for the case of graphene and graphite, with a little energy expenditure carbon can take the configuration of $1s^2 2s 2p_x 2p_y 2p_z$. The energy expenditure is offset by the release of energy in the formation of hybrid orbitals. The outer electrons share very similar energy and their wave functions mix readily, the one s orbital then hybridises with two of the p orbitals forming the state $1s^2 sp^2 2p_z$ (sp^2 hybridisation) forming a total of three sp^2 orbitals (see figure 1.1).

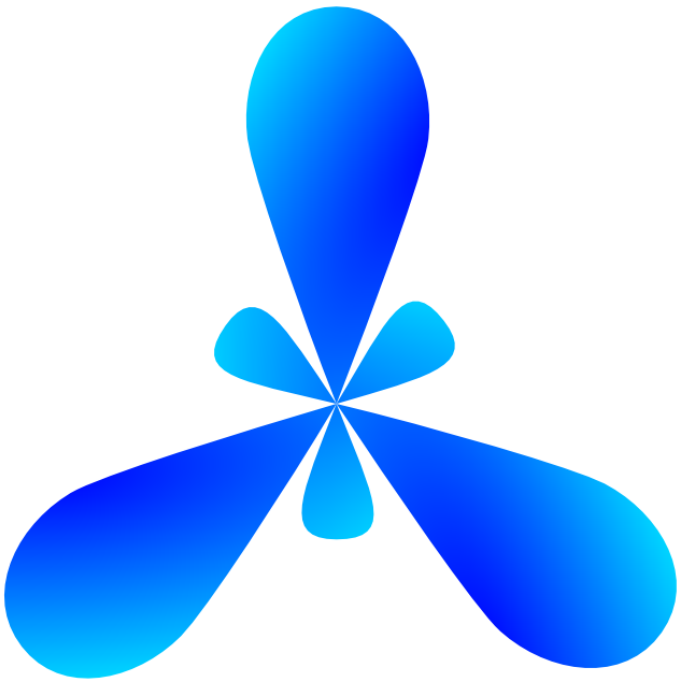

Figure 1.1: Three SP^2 hybridised orbitals. The $2P_z$ (not depicted) is perpendicular to the page.

These hybridised orbital's then form σ bonds within the graphene structure, where a single carbon atom is bonded to three other carbon atoms. Using VSEPR theory it is clear that this formation of atoms forms a trigonal planar geometry, where the bond angle is 120^o. This trigonal planar geometry can then be expanded to form a graphene sheet. The remaining $2p_z$ orbital forms a delocalised π bond around the carbon ring. Graphene can then be stacked into thicker structures such as multi-layer graphene and graphite bonded by van de Waals forces between layers. The properties of graphene systems vary dramatically depending on the number of layers in the stacks and the type of stacking. Therefore electronic properties of mono-, bi- and tri-layer graphene will now be discussed with the use of the tight binding approximation. The tight binding approximation refers to a system where electrons within the system are tightly bound to atomic cores, these electrons have limited interaction with neighboring atoms. As a result the wave functions of the electrons resemble that of electrons in a free atom. The model consists of the combination of neighboring wave functions. This model provides a good at approximating the band structure of a system, however has difficulty describing the conduction of the electrons themselves.

1.2 Tight binding approximation for mono-layer graphene

A description of mono-layer shall first be made, before extending the model to bi- and tri-layer graphene. A tight binding approximation will be made of mono-layer graphene to determine its dispersion relation [15][16][17][18]; this was first applied by Wallace[19] as a simplified model for describing graphite [20]. First the graphene lattice must be defined, as shown in figure 1.2. The full graphene lattice consists of two non-equivalent sub-lattices, A and B. The two non-equivalent sub-lattices occur as it is impossible to create a translation vector to reach every atom site in the honeycomb structure, as such the unit cell of graphene contains two non-equivalent atoms one from sub-lattice A and the other from sub-lattice B (shown as a dotted line in figure 1.2).

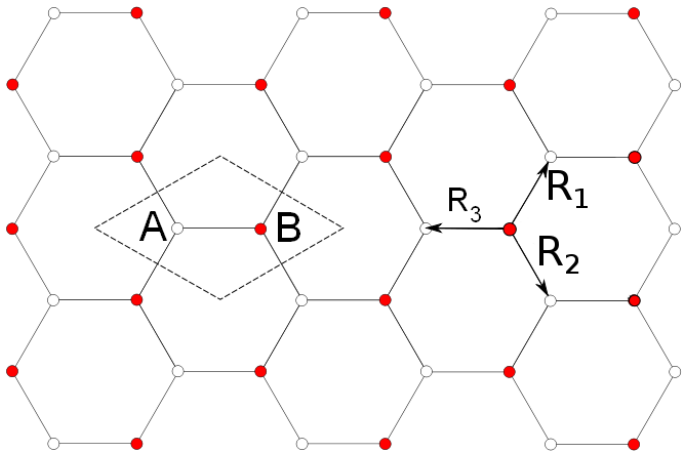

Figure 1.2: The graphene honeycomb structure. Non equivalent atomic sites are shown in red and white, while the dashed rhombus shows the graphene unit cell.

As there are two sub-lattices in graphene, both lattices must be considered when performing the tight binding approximation. The approximation uses a linear combination of atomic orbitals of nearest neighbors, defined by vectors R_1, R_2 and R_3 (shown in 1.2).The dispersion relation of graphene will now be derived, starting from the Schrödinger equation

$$\hat{H}\Psi(\mathbf{k}) = E(\mathbf{k})\Psi(\mathbf{k}) \tag{1.1}$$

$\hat{H}$ is the Hamiltonian of the system, E($\mathbf{k}$) is the energy eigenvalue as a function of the wave vector $\mathbf{k}$, and Ψ is the eigenfunction within the 2D-graphene. Ψ is constructed from the Bloch functions $\phi_{A,B}$ corresponding to each of the sublattices A and B

$$\phi_j(\mathbf{k},\mathbf{r}) = \sum_{i=1}^{n} e^{i\mathbf{k}\mathbf{R_i}}\rho_i(\mathbf{r}-\mathbf{R_i}) \qquad j = A,B \tag{1.2}$$

Here $\mathbf{R}_i$ is the position of the i^{th} atom and ρ_i is its atomic orbital. Ψ is then expressed as a linear combination of Bloch functions for the two sublattice.

$$\Psi_j(\mathbf{k},\mathbf{r}) = \sum_{\mathrm{j'}} C_{jj'}(\mathbf{k})\phi_{j'}(\mathbf{k},\mathbf{r}) \qquad j' = A, B \tag{1.3}$$

where $C_{jj'}$ are coefficients yet to be determined. Using Dirac notation the eigenvalues E_j can be expressed as

$$E_j(\mathbf{k}) = \frac{<\Psi_j|\hat{H}|\Psi_j>}{<\Psi_j|\Psi_j>} \tag{1.4}$$

where one defines the transfer and overlap integrals between neighboring atoms as

$$\mathbf{H}_{jj'}(\mathbf{k}) =<\phi_j|\hat{H}|\phi_j> \qquad \mathbf{S}_{jj'}(\mathbf{k}) =<\phi_j|\phi_j> \tag{1.5}$$

Substituting the transfer and overlap integral into the Schrödinger equation one obtains

$$E_i(\mathbf{k}) = \frac{\sum^{\mathrm{B}}_{\mathrm{j,j'=A}} C^*_{ij}\, C_{ij'}\, \hat{H}_{jj'}}{\sum^{\mathrm{B}}_{\mathrm{j,j'=A}} S_{jj'}\, C^*_{ij}\, C_{ij'}} \tag{1.6}$$

where $C_{ij'}$ and $C^*_{ij'}$ are coefficents yet to be determined. The coefficient $C^*_{ij'}$ are optimised to minimise $E_j(\mathbf{k})$ leading to

$$[H(\mathbf{k}) - E_j(\mathbf{k})S(\mathbf{k})]C_j = 0 \tag{1.7}$$

To obtain a wavefunction C_j must exist therefore the secular equation is obtained

$$det[H(\mathbf{k}) - E(\mathbf{k})S(\mathbf{k})] = 0 \tag{1.8}$$

The secular equation can be expressed for individual sublattice sites

$$\begin{vmatrix} \mathbf{H}_{AA} - E\mathbf{S}_{AA} & \mathbf{H}_{AB} - E\mathbf{S}_{AB} \\ \mathbf{H}_{BA} - E\mathbf{S}_{BA} & \mathbf{H}_{BB} - E\mathbf{S}_{BB} \end{vmatrix} = 0 \tag{1.9}$$

As the two atoms in the unit cell are identical $\mathbf{H}_{AA} = \mathbf{H}_{BB}$. Similarly $\mathbf{H}_{BA} = \mathbf{H}^*_{AB}$. Therefore one obtains

$$\begin{vmatrix} \mathbf{H}_{AA} - E\mathbf{S}_{AA} & \mathbf{H}_{AB} - E\mathbf{S}_{AB} \\ \mathbf{H}^*_{AB} - E\mathbf{S}^*_{AB} & \mathbf{H}_{AA} - E\mathbf{S}_{AA} \end{vmatrix} = 0 \tag{1.10}$$

For simplicity only the three nearest neighbors of a C atom, as shown in figure 1.2, are

considered in 1.5 and 1.10. This leads to

$$\begin{aligned} \hat{H}_{AA} &= <\phi_A|\hat{H}|\phi_A> \\ &= \tfrac{1}{N}\sum_{\mathrm{R_A}}\sum_{\mathrm{R_{A'}}} < e^{i\mathbf{kR_A}}\varphi_A(\mathbf{r}-\mathbf{R_A})|\hat{H}|e^{i\mathbf{kR'_A}}\varphi_A(\mathbf{r}-\mathbf{R'_A}) > \\ &= \epsilon_{2p} \end{aligned} \tag{1.11}$$

Here ϵ_{2p} is the energy of the $2p_Z$ orbital offset by the periodic potential of the lattice. The overlap integral S_{AA} is formed in the same way, setting it equal to one and normalising $S_{AA} = 1$ $\hat{H}_{AB}$ is given by

$$\begin{aligned} \hat{H}_{AB} &= <\phi_A|\hat{H}|\phi_B> \\ &= \tfrac{1}{N}\sum_{\mathbf{R}_\mathrm{A}}\sum_{\mathbf{R}_\mathrm{B}} e^{i\mathbf{k}(\mathbf{R}_B-\mathbf{R}_A)} < \varphi_A(\mathbf{r}-\mathbf{R}_A)|\hat{H}|\varphi_B(\mathbf{r}-\mathbf{R}_B) > \end{aligned} \tag{1.12}$$

The sums $\sum_{\mathrm{R_A}}$ and $\sum_{\mathrm{R_B}}$ are reduced only over the three nearest neighbors and using the vectors to the nearest neighbors as shown in figure 1.2 one obtains

$$\hat{H}_{AB} = \gamma_0 \cdot (e^{i\mathbf{k}\cdot\mathbf{R_1}} + e^{i\mathbf{k}\cdot\mathbf{R_2}} + e^{i\mathbf{k}\cdot\mathbf{R_3}}) = \gamma_0 \cdot f(\mathbf{k}) \tag{1.13}$$

where

$$\gamma_0 =< \varphi_A(\mathbf{r}-\mathbf{R}_A)|\hat{H}|\varphi_B(\mathbf{r}-\mathbf{R}_A-\mathbf{R}_1) > \tag{1.14}$$

is the carbon carbon interaction energy. Similarly, the overlap integral S_{AB} is calculated. Now the equation 1.8 can be solved

$$det\left[\begin{pmatrix} \epsilon_{2P} & \hat{H}_{AB} \\ \hat{H}_{BA} & \epsilon_{2P} \end{pmatrix} - \begin{pmatrix} E_1(\mathbf{k}) & 0 \\ 0 & E_2(\mathbf{k}) \end{pmatrix}\begin{pmatrix} 1 & S_{AB} \\ S^*_{AB} & 1 \end{pmatrix}\right] = 0 \tag{1.15}$$

where E_1 and E_2 are the eigenvalues corresponding to the conduction and valence energy bands, respectively. After solving the determinant an expression for the dispersion relation can be obtained, where S_0 is the overlap energy

$$E^{\pm}(k_x,k_y) = \frac{\epsilon_{2P} \pm \gamma_0\sqrt{f(k_x,k_y)}}{1 \pm S_0\sqrt{f(k_x,k_y)}} \tag{1.16}$$

with

$$\sqrt{|f(k_x,k_y)|^2} = \sqrt{1 + 4cos\frac{\sqrt{3}k_x a}{2}cos\frac{k_y a}{2} + 4cos^2\frac{k_y a}{2}} \tag{1.17}$$

Using this equation and values for γ_0 and S_0 a visualisation of the dispersion relation can be obtained, this is shown in figure 1.3.

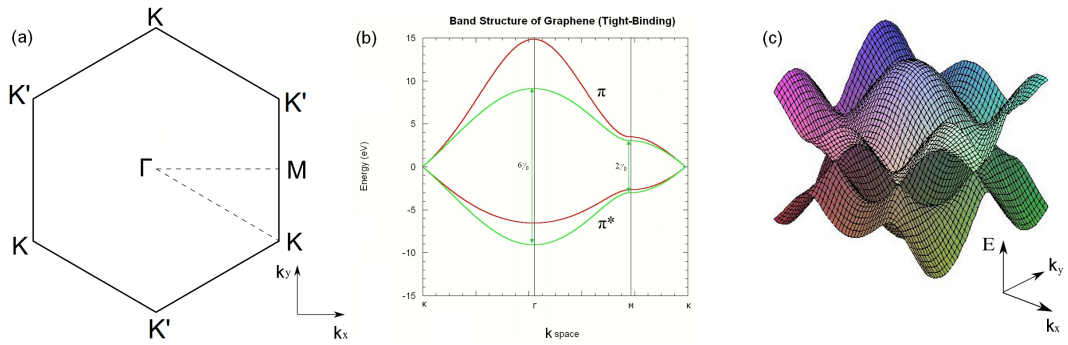

Figure 1.3: (a) the Brillouin zone of graphene with its high symmetry points. (b) the dispersion relation along the high symmetry directions in the Brillouin zone. (c) the dispersion relation plotted in the 2D k space and neglecting the overlap S_0.

Figure 1.3(a) shows the Brillouin zone of graphne with the high symmetry points Γ, M, K and K′, the K and K′ points are due to the non-equivalent sub-lattices A and B. Figure 1.3(b) shows a cross section of the dispersion relation between the high symmetry points, shown as a dotted line in figure 1.3(a), the cross sections shows the π and π^* bands. The two colours correspond to different sets of parameters used in the calculation of the dispersion relation: with green, parameters where the overlap S_0 is neglected (γ_0 = -2.7eV and $S_0 = 0$), while with the red line, parameters found through ab-initio calculations (γ_0 = -2.84eV and $S_0 = 0.07$). [21] Figure 1.3(c) shows a three dimensional depiction of the dispersion relation within the Brillouin zone, note the position of the K and K points (six points in total) where the π and π^* bands touch at which point the density of states (DOS) is at zero. The Dirac points is what gives graphene its unique properties. Around a K point, the dispersion relation for graphene is linear, as shown in figure 1.4[22], which resembles relativistic Dirac fermions and therefore this is a massless band [23][24]. The diagram shows that when the Fermi level is around the Dirac points the density of states is zero with no band gap, hence graphene is a semi-metal or a zero gap semiconductor.

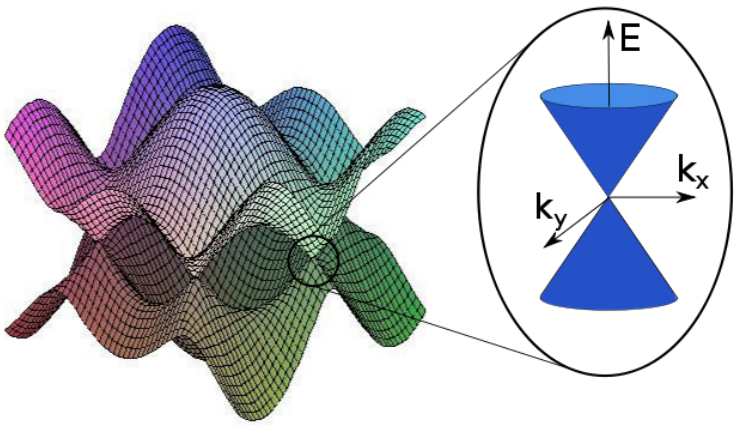

Figure 1.4: Around the K(K′) points the energy bands are linear.

1.2.1 Dirac formalism for the electronic structure of graphene

Now the consequences of the linear bands around the Dirac points (K and K′) will be explored. Around these points the Hamiltonian can be written either by developing the Schrödinger Hamiltonian using the $\mathbf{k}\cdot\mathbf{p}$ method[20], or noticing that the dispersion relationship $E(\mathbf{k})$ from figure 1.4 resembles that of relativistic fermions for which one uses the Dirac Hamiltonian [23].

$$H_K = \hbar v_F \hat{\sigma}\cdot\hat{\mathbf{k}} \tag{1.18}$$

$$H_{K\prime} = \hbar v_F \hat{\sigma}^*\cdot\hat{\mathbf{k}}$$

where $\hat{\sigma} = (\hat{\sigma_x}, \hat{\sigma_y})$ and $\hat{\sigma_x} = \left(\begin{smallmatrix} 0 & 1 \\ 1 & 0 \end{smallmatrix}\right)$ and $\hat{\sigma_y} = \left(\begin{smallmatrix} 0 & -i \\ i & 0 \end{smallmatrix}\right)$ are the Dirac matrices, $\hat{\mathbf{k}} = -i\hbar\cdot\nabla$, and $\mathrm{v}_F = 3{\cdot}10^8$cm/s is the Fermi velocity. The eigenfunction Ψ is the form of

$$\Psi_K(\mathbf{k},\mathbf{r}) = f_A(\mathbf{k})\cdot e^{i\mathbf{kr}}\cdot\phi_A(K,\mathbf{r}) + f_B(\mathbf{k})\cdot e^{i\mathbf{kr}}\cdot\phi_B(K,\mathbf{r}) \tag{1.19}$$

which can be written in a "spinor" form

$$\psi_K(\mathbf{k},\mathbf{r}) = \begin{pmatrix} f_A(\mathbf{k}) \\ f_B(\mathbf{k}) \end{pmatrix}\cdot e^{i\mathbf{kr}} \tag{1.20}$$

This "spinor" is a two-component, slow-varying envelope function, describing the wave function components on lattices A and B. $\phi_{A,B}$ are the Bloch functions corresponding to sub-lattices A and B evaluated at the K point. Throughout this section and the following ones $\mathbf{k}$ describes the departure from K, i.e. $\mathbf{K}+\delta\mathbf{k}$ where we redefine $\delta\mathbf{k} = \mathbf{k}$.

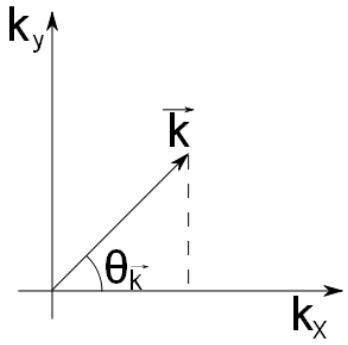

Figure 1.5: The chiral angle expressed as a function of the k_x and k_y components of the k vector.

The eigenfunction Ψ can be re-written so that the chiral angle $\theta_{\mathbf{k}}$is revealed

$$\Psi_K(\mathbf{k},\mathbf{r}) = \frac{1}{\sqrt{2}} \begin{pmatrix} 1 \\ e^{-i\theta_{\mathbf{k}}} \end{pmatrix} e^{i\mathbf{kr}} \tag{1.21}$$

where $\theta_{\mathbf{k}} = \arctan(\frac{k_y}{k_x})$ is shown in Figure 1.5.

Using (1.21) in the Dirac equation leads to the linear dispersion relationship

$$E(\mathbf{k}) = \pm\hbar v_F|\mathbf{k}| \tag{1.22}$$

.

where $\pm$ correspond to the conductance and valence bands respectively. This is the equation used when describing the low energy dispersion relation of graphene.

1.2.2 Density of states of monolayer graphene

The density of states can now be deduced. Starting with an area defined by L_x and L_y in the real space, one know considers the effects of quantisation in the reciprocal space (k_x, k_y). Quantization in the **k** space leads to the "surface" occupied by one state being

$$\frac{2\pi}{L_x} \times \frac{2\pi}{L_y} = \frac{4\pi^2}{S_{urf}} \tag{1.23}$$

The number of lattice points (allowed states) within the circle πk^2 is given by

$$N_T = g\frac{k^2}{4\pi}S_{urf} \tag{1.24}$$

where g is the degeneracy of each state. Combining this with the linear band E($\mathbf{k}$) = s($\hbar$V$_F$)| $\mathbf{k}$ | around a K point in graphene(where s $\pm$ 1 for the conduction and valence band respectivly), the total number of states within the graphene cone up to energy E is given by

$$N_T = g\frac{E^2}{(\hbar V_F)^2}\frac{1}{4\pi}S_{urf} \tag{1.25}$$

The density of states ρ can then be calculated from its definition as number of states per energy and surface unit

$$\rho_{DOS}(E) = \frac{d}{dE}\left(\frac{N_T}{S_{urf}}\right) \tag{1.26}$$

$$\rho_{DOS}(E) = \frac{g}{2\pi(\hbar V_F)^2} \mid E \mid \tag{1.27}$$

with g= g$_s$·g$_V$, where g$_s$ = 2 is the spin degeneracy and g$_v$ = 2 is the valley degeneracy due to there being two sublattices within graphene leading to two unequivalent types of Dirac points (K and K′). The DOS for graphene appears thus as a linear centred about the K point with zero DOS at the K point for low values of energy, as shown in figure 1.6.

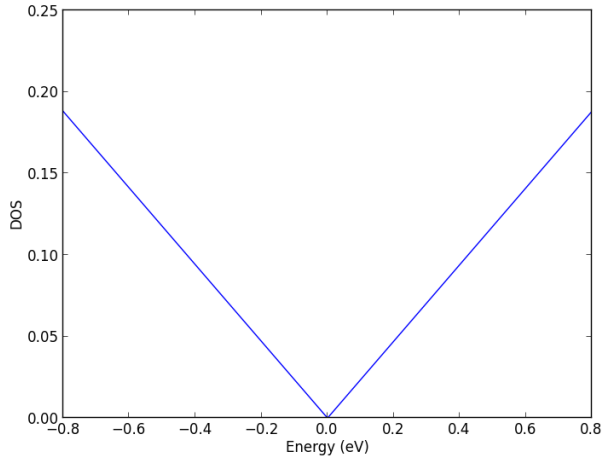

Figure 1.6: The density of states of graphene.

1.3 Bilayer graphene

Bilayer graphene consists of two stacked mono-layers of graphene bonded together through weak Van der Waals forces from the π orbitals. The most common stacking orientation is Bernal stacking (AB-stacking)[16],as shown in figure 1.7, however other forms of stacking exist (rhombohedral stacking). First Bernal stacking shall be examined to identify simi-

larities within the structure, which will then be used to compose the tight binding model for bilayer graphene. The band structure will then be examined and compared to single layer graphene. Finally the density of states will be examined.

1.3.1 Tight Binding model for Bernal-stacked bilayer graphene

The tight binding model for bilayer graphene is more complex than that for mono-layer graphene. Since the introduction of an additional layer adds many extra interactions that must be considered. Some of these interactions are weak and need not be considered for a minimal model, however some of the interactions form high energy bands which drastically alter the electronic properties of bilayer graphene and must be considered [25][26]. Figure 1.7 shows a side view of bilayer graphene; here the interaction between layers is clearer and, for clarity the A and B sites are now also associated with an index to identify their layer. As with the tight binding model for mono-layer graphene, only interactions between nearest neighbor atoms are considered. There are still intra-plane interactions, these are the interactions between A_1-B_1 and A_2-B_2 sites, parameterized as $\gamma_{A_1B_1} = \gamma_{A_2B_2} = \gamma_0$ Next are the inter-plane interactions: first the strongest interaction is considered, and for Bernal stacking this is for the atomic sites directly above and below each other, i.e. the A_2-B_1 interaction (note that these sites may be referenced differently in other sources). This strong coupling produces dimers from these pairs of orbitals, which leads to the formation of high energy bands, this is defined as γ_1. For this simplistic model, this interaction is ignored

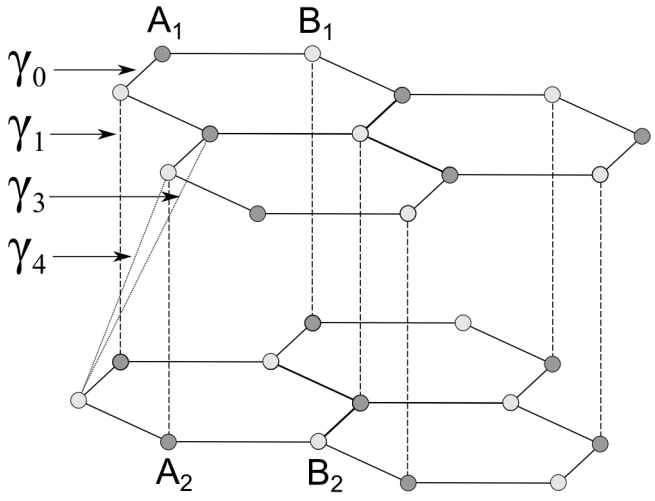

Figure 1.7: Bernal stacking in bilayer graphene.

γ_0 is defined as $\gamma_0 = (\sqrt{3}ta)/2$, where a is the graphene lattice constant. The in-

terlayer interaction between B1 and A2 are included in this approximation, forming $gamma_1$. However, other weaker interactions between the layers are ignored in this approximation[27], although the finer detials of the physics are removed, the larger more important physics that is relevant for this work is retained. From this the Hamiltonian can be written as

$$H_{AB} = \begin{pmatrix} 0 & f & 0 & 0 \\ f^* & 0 & -t' & 0 \\ 0 & -t' & 0 & f \\ 0 & 0 & f^* & 0 \end{pmatrix} \tag{1.28}$$

Here we will use f as the in-plane hopping energy and t′ as the hopping energy between planes. The Hamiltonian can be thought of as four smaller matrices, two of which contain information of the bonding within each layer (upper left and bottom right 2x2 blocks). The other two positions contain information about the coupling between the layers, where t′ is the hopping energy between planes. The characteristic polynomial can then be found, using the variable λ and the identity matrix I

$$det(H_0 - \lambda I) = 0 \tag{1.29}$$

$$(\lambda^2 - \left|f\right|^2)^2 - \lambda^2 t'^2 = 0 \tag{1.30}$$

In this form the structure of the energy bands can be deduced. There are four eigen values, with four electrons (one electron per atom) occupy the lowest two bands (spin up and spin down) and hence states with $\lambda \ll 0$ will be occupied while the states with $\lambda > 0$ will be unoccupied. If λ is small, the previous equation can be reduced by ignoring λ^4 to

$$-2\lambda^2|f|^2 + |f|^4 - \lambda^2 t'^2 = 0 \tag{1.31}$$

Therefore

$$\lambda^2 = \frac{|f|^4}{t'^2 + 2|f|^2} \tag{1.32}$$

Hence the lowest energy states occur when $|f|$ is smallest. Using the graphene lattice, it can be shown that f is

$$\gamma(\xi k_x + i k_y) \tag{1.33}$$

where $\xi = \pm 1$, and therefore

$$|f|^2 = \gamma^2(q_x^2 + q_y^2) = \gamma^2 q^2 \tag{1.34}$$

where $\vec{q}$ is a wavevector relating to the Dirac points. Returning to equation 1.30, the low energy states are when $|f|^2 \approx \gamma^2 q^2$, for a small q.

$$(\lambda^2 - \gamma^2 q^2) = \pm \lambda t' \tag{1.35}$$

giving the quadratic

$$\lambda = \frac{\pm t' \pm \sqrt{t'^2 + 4\gamma^2 q^2}}{2} \tag{1.36}$$

with roots

$$\lambda \approx \pm (t' + \frac{\gamma^2 q^2}{t'}, \pm \frac{\gamma^2 q^2}{t'}) \tag{1.37}$$

Here there are two sets of parabolic bands (two massive bands) , one set that touch at $\epsilon = 0$ and two additional bands that start at $\pm t'$, as shown in figure 1.8.

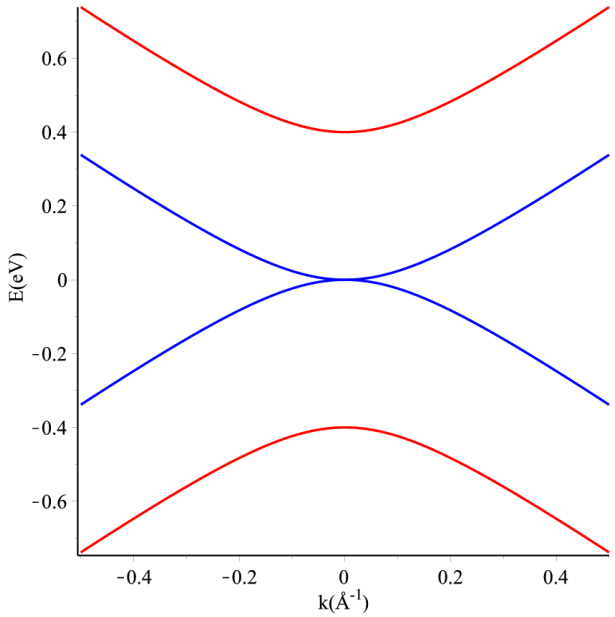

Figure 1.8: Band structure of Bernal stacked bilayer graphene.

From here the density of states can be found. Here there are two equations, equation 1.38 for engergy lower than t' and equation 1.39 for energy higher than t'.

$$\rho_{DOS}(E) = \frac{2E + t'}{\pi \hbar^2 v_F^2} \tag{1.38}$$

$$\rho_{DOS}(E) = \frac{4E}{\pi \hbar^2 v_F^2} \tag{1.39}$$

This results in figure 1.9, where the DOS never reaches zero because of the parabolic dispersion relation and jumps to a higher DOS at t' because of the second set of bands becoming occupied at this energy, this increases the gradient beyond this energy because of this additional occupation.

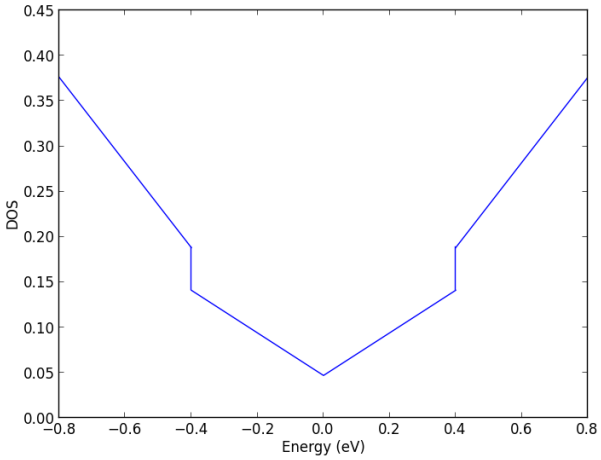

Figure 1.9: Density of states for AB stacked bi-layer graphene.

1.3.2 Breaking of symmetry within Bernal stacked bilayer graphene

When the two graphene planes in the bilayer graphene are subjected to different electrostatic potentials, there is a breaking of symmetry between the two layers and the simplistic model shown previously changes [28][29][30][31]. The new Hamiltonian becomes the following, where the onsite potential is defined as -V and +V for the top and bottom layers respectively.

$$H_{AB} = \begin{pmatrix} -V & f & 0 & 0 \\ f* & -V & -t' & 0 \\ 0 & -t' & +V & f \\ 0 & 0 & f* & +V \end{pmatrix} \tag{1.40}$$

This results in the following dispersion relation

$$\lambda \approx \pm\frac{1}{2}\sqrt{4|f|^2 + 4v^2 + 2t^2 \pm 2\sqrt{16v^2f^2 + 4f^2t^2 + t^4}} \tag{1.41}$$

Which is also shown in figure 1.10 where the potential is set to ± 0.5V. Notice here how both sets of bands are deformed compared to the dispersion relation in the absence the applied potential, with the low energy bands being more significantly deformed, and

the energy at k=0 being located at 0.5±eV. This allows a tunable bandgap to be opened in Bernal stacked bilayer graphene.

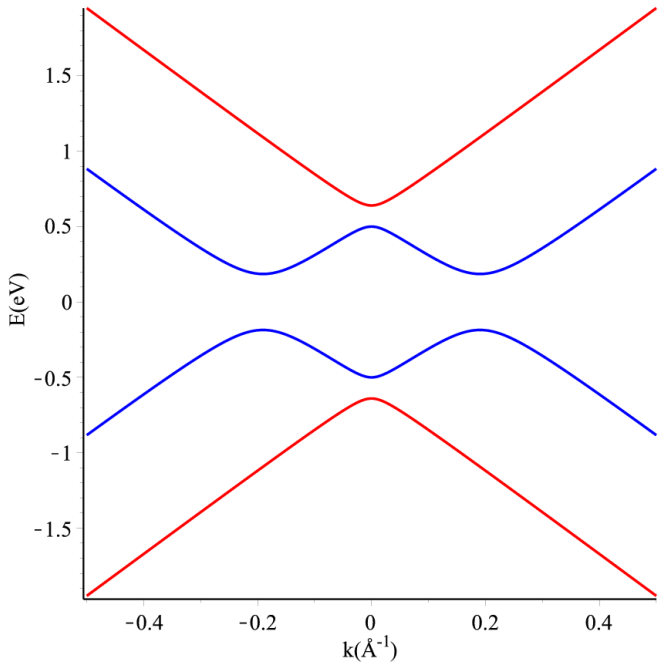

Figure 1.10: Band structure of Bernal stacked bilayer graphene with an applied potential difference between the two layers of 1V.

1.3.3 AA stacked bilayer graphene

Next the second type of bilayer stacking will be discussed, as well as the differences between AA and AB stackings [32][33]. Figure 1.11 shows the relative position of the graphene layers. This stacking order alters the coupling between sheets: here all atomic sites are directly coupled to each other, whereas in the AB stacking this only occurs between half the atomic sites. Therefore in the AA-stacks there are an increased number of parameters within the Hamiltonian. This has a dramatic effect on the band structure on bilayer graphene.

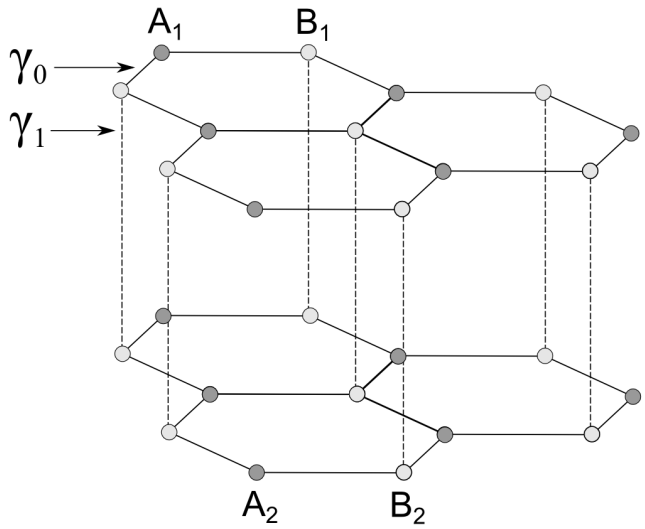

Figure 1.11: Stacking of AA stacked bi-layer graphene.

This structure results in the following Hamiltonian:

$$H_{AA} = \begin{pmatrix} 0 & f & -t' & 0 \\ f* & 0 & 0 & -t' \\ -t' & 0 & 0 & f \\ 0 & -t' & f* & 0 \end{pmatrix} \tag{1.42}$$

with the following eigenvalues

$$\lambda \approx \pm t' \pm f \tag{1.43}$$

which results in the two massless bands shown in figure 1.12

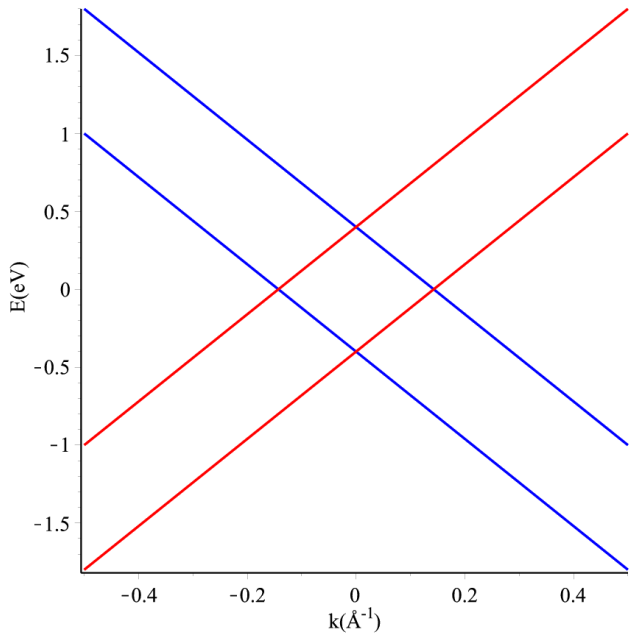

Figure 1.12: Band structure of AA stacked bi-layer graphene.

Notice that the bands are linear and not parabolic as with AB stacking, this resembles the monolayer band structure.

1.3.4 Biased AA stacked bilayer graphene

The effect of applying a potential difference between top and bottom AA-stacked layers will now be explored[33]. This will be performed in a similar way to AB-stacked graphene where the potential will be applied to the atomic sites that are situated along the diagonal of the Hamiltonian. This Hamiltonian results in the eigenvalues shown in equation 1.45

$$H_{AA} = \begin{pmatrix} -V & f & -t' & 0 \\ -V & f & -t' & 0 \\ f* & -V & 0 & -t' \\ -t' & 0 & V & f \\ 0 & -t' & f* & V \end{pmatrix} \tag{1.44}$$

$$\lambda \approx \pm f \pm \sqrt{t'^2 + V^2} \tag{1.45}$$

The result of biasing the layers is that of altering the k vector at which the bands cross the zero energy point, however since they will all still cross, there will never be an

opening of the band gap.

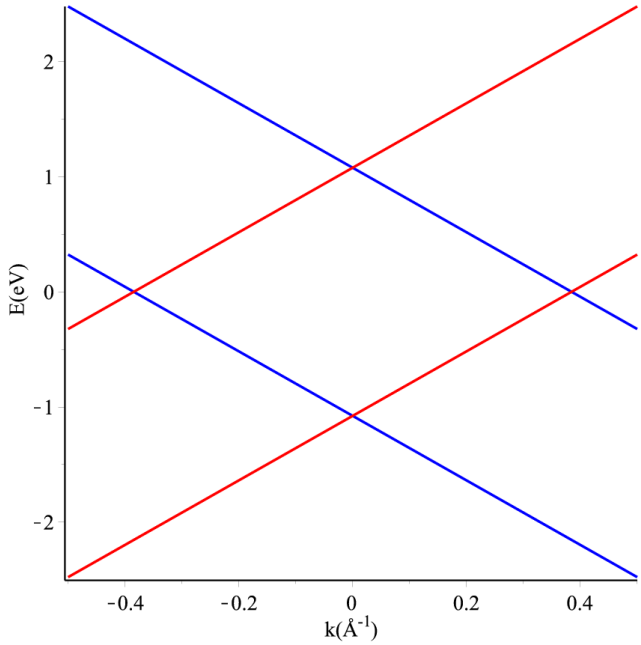

Figure 1.13: Band structure of AA-stacked bilayer graphene with an applied potential of ±0.5 V on top and bottom layers.

1.4 Trilayer graphene

Next the two most common forms of trilayer graphene will be discussed, Bernal (ABA) and rhombohedral (ABC) stacking. Again the difference between these two stacking types creates a striking differences between their low energy band structures.

1.4.1 Bernal stacked trilayer graphene

First the Bernal stacked form of trilayer graphene will be discussed. There are many different interactions within the trilayer system as shown in figure 1.14. However, as with Bernal stacked-bilayer graphene, some of these interactions can be ignored in a simple approximation, resulting in coupling terms between A and B atom sites on the same layer and interlayer coupling between atom sites that sit directly above and below each other (γ_1), where weaker interactions between adjacent planes (γ_3)and interactions between the third and first layers are ignored. The Hamiltonian created using these parameters is shown in 1.46.

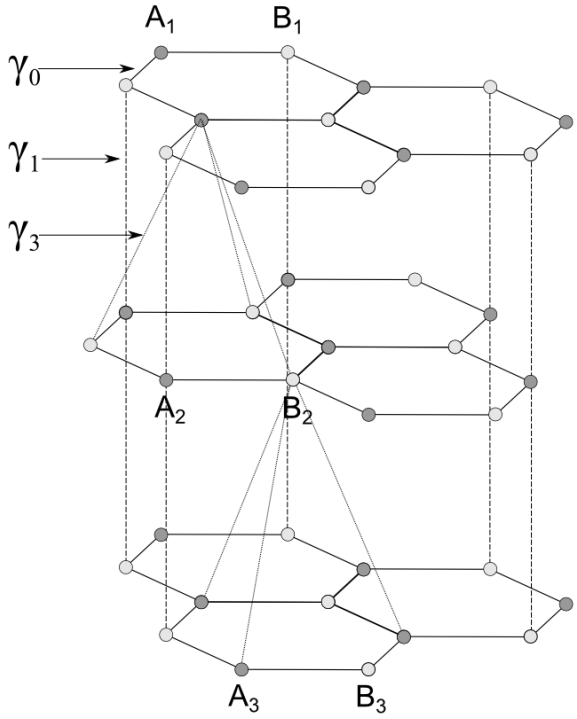

Figure 1.14: Bernal stacking of trilayer graphene.

$$H_{ABA} = \begin{pmatrix} 0 & f & 0 & 0 & 0 & 0 \\ f* & 0 & -t' & 0 & 0 & 0 \\ 0 & -t' & 0 & f & 0 & -t' \\ 0 & 0 & f* & 0 & 0 & 0 \\ 0 & 0 & 0 & 0 & 0 & f \\ 0 & 0 & -t' & 0 & f* & 0 \end{pmatrix} \tag{1.46}$$

This results in the band structure shown in figure 1.15. The bands are formed from two sets of parabolic bands and one set of linear bands, therefore there are two massive subbands and one massless band similar to single layer graphene. Therefore there cannot be a bandgap created through breaking of symmetry using an electric field. However work has shown that a tunable band overlap can be created on the lowest parabolic band [34][35].

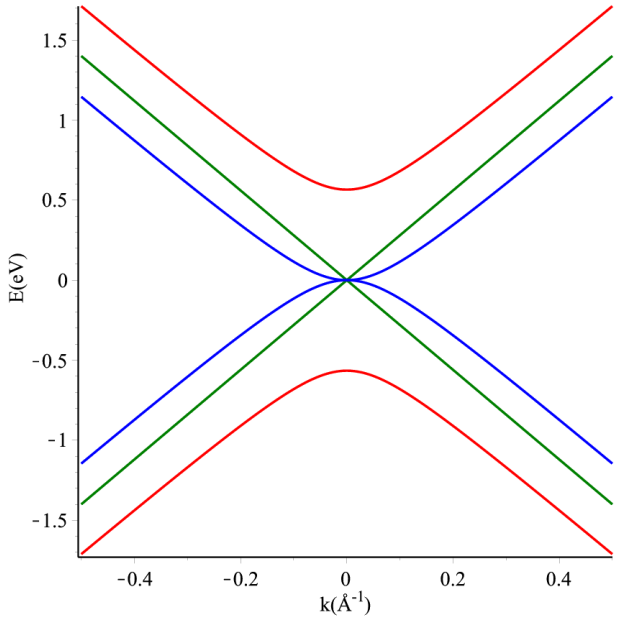

Figure 1.15: Band structure of Bernal stacked graphene.

1.4.2 Rhombohedral stacked trilayer graphene

Rhombohedral (ABC) stacking of graphene consists of three graphene layers that are all positioned differently (shown in figure 1.16). As with previous layouts there are many interactions in the system, however for simplicity only coupling between the atoms that are directly above each other and atoms that are in the same layer are considered, this results in the Hamiltonian shown in 1.17.

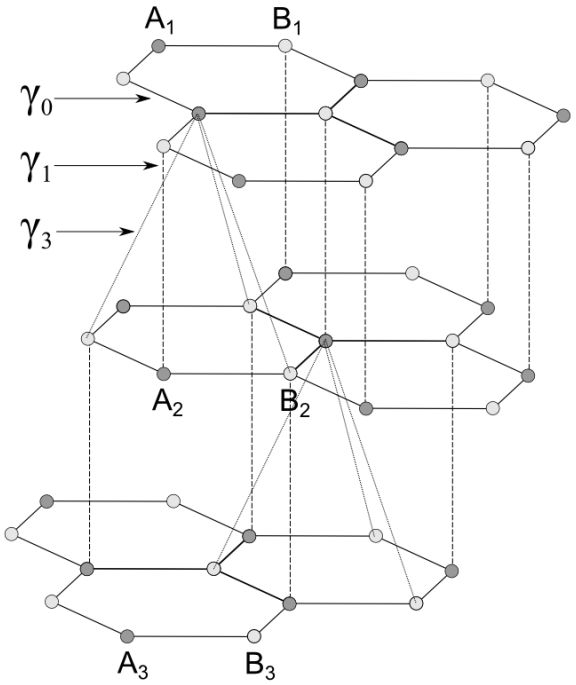

Figure 1.16: Rhombohedral stacking of trilayer graphene.

$$H_{ABC} = \begin{pmatrix} 0 & f & 0 & 0 & 0 & 0 \\ f* & 0 & -t' & 0 & 0 & 0 \\ 0 & -t' & 0 & f & 0 & 0 \\ 0 & 0 & f* & 0 & -t' & 0 \\ 0 & 0 & 0 & -t' & 0 & f \\ 0 & 0 & 0 & 0 & f* & 0 \end{pmatrix} \tag{1.47}$$

The band structure obtained is that of three sets of bands, two massive bands and a massless band, the lowest of these touching at the zero energy point, shown in figure 1.17. Applying an electric field between layers breaks the symmetry between layers and creates a tunable bandgap. Therefore Bernal and Rhombohedral stacked trilayer graphene are significantly different, not only in their bandstructure, but that a perpendicular applied electric field will create a band gap in Rhombohedral-stacked trylayer graphene where as it will create a band overlap in Bernal-stacked trilayer graphene.

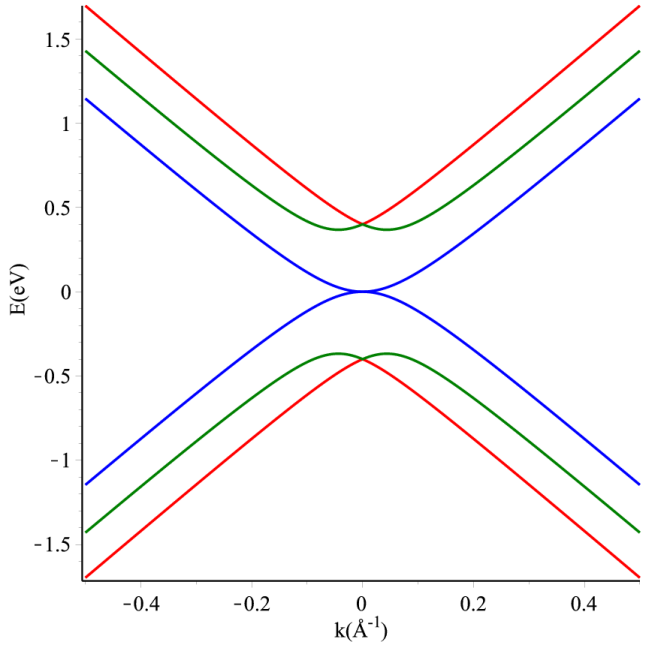

Figure 1.17: Band structure of Rhombohedral stacked graphene.

Chapter 2

Identification of graphene

Methods applied for the identification of graphene films laid on transparent, crystalline insulating substrates are described: optical identification using cross-polarized light, bubble formation through condensation, and Atomic Force Microscopy. The use of such methods was specific to this work. Optical identification methods that are suitable for opaque SiO_2/Si substrates are also described since they were used in the initial stages of this work.

2.1 Optical identification of graphene on silicon

For graphene the optical absorption of visible light is strong; this is due to the band structure of graphene. As the bands are linear and cross at the Dirac point there are a large range of energies that are able to be absorbed. On mono-layer graphene the total absorption is approximately 2.3% [36]. This value is extremely large for a material of its thickness, this is what enables graphene to be identified optically. The substrate graphene has been deposited onto also has a significant contribution to the contrast of graphene. For instance when exfoliating graphene onto a silicon wafer with a silicon dioxide layer, the optical system created between the silicon, silicon dioxide and the graphene alters the contrast of the graphene significantly

Consider graphene deposited onto silicon wafer, a tri-layer system is created between the silicon, silicon dioxide and graphene (shown in figure 2.1)[37]. The change in contrast of this system can be explained using Fresnels equations. Incident light can be reflected from different material boundaries within the system, there will then be interference due to the difference in length of the optical paths.

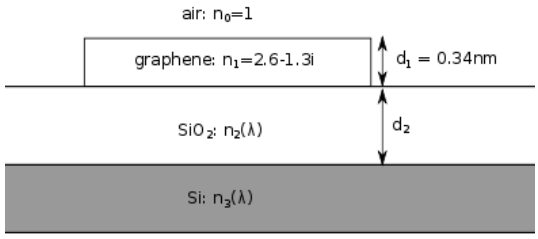

Figure 2.1: Figure shows the Graphene/SiO_2/Si trilayer system.

For this tri-layer system, the reflected light intensity can be written as:

$$\begin{aligned} I(n_1) &= |\,(r_1 e^{i(\phi_1+\phi_2)} + r_2 e^{-i(\phi_1-\phi_2)} \\ &\quad + r_3 e^{-i(\phi_1+\phi_2)} + r_1 r_2 r_3 e^{i(\phi_1-\phi_2)}) \\ &\quad \times (e^{i(\phi_1+\phi_2)} + r_1 r_2 e^{-i(\phi_1-\phi_2)} \\ &\quad + r_1 r_3 e^{-i(\phi_1+\phi_2)} + r_2 r3 e^{i(\phi_1-\phi_2)})^{-1}\,|^2 \end{aligned} \tag{2.1}$$

The relative indices of reflection from the interface between materials is then given by:

$$r_1 = \frac{n_0 - n_1}{n_0 + n_1}, r_2 = \frac{n_1 - n_2}{n_1 + n_2}, r_3 = \frac{n_2 - n_3}{n_2 + n_3} \tag{2.2}$$

$\phi_1 = 2\pi n_1 d_1/\lambda$ and $\phi_2 = 2\pi n_2 d_2/\lambda$

These are the phase shifts due to the changes in the optical path. Where n and d are the refractive index and the thickness of the different materials respectively, and shown in figure 2.1. The total contrast C can then be defined as the relative intensity of reflected light in the presence (n != 1) and absence (n1 = n0 = 1) of graphene [37].

$$C = \frac{I(n_1 = 1) - I(n_1)}{I(n_1 = 1)} \tag{2.3}$$

From here the contrast can be plotted as a function of variables incident light wavelength and oxide thickness, this produces the surface plot shown in figure 2.2, from here it is possible to observe an oxide thicknesses with greatest contribution to the contrast of graphene, it can be seen that 90 and 300nm oxide thicknesses are most suitable.

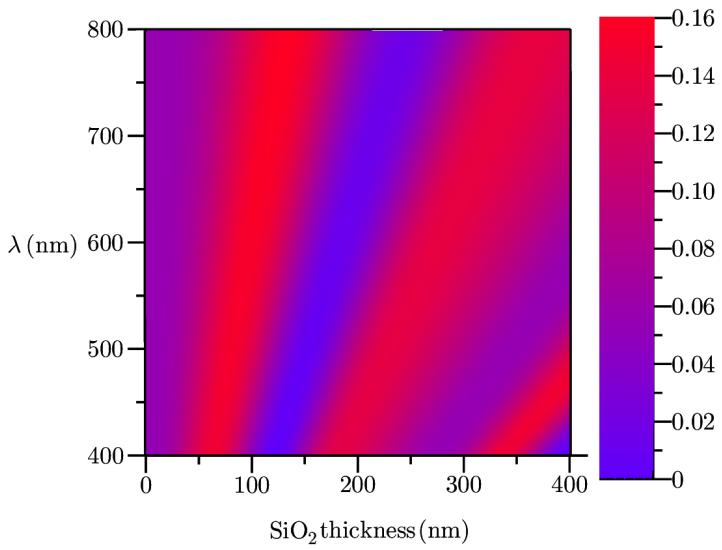

Figure 2.2: Colour plot of the contrast as a function of wavelength and SiO_2 thickness.

From here it is possible to identify graphene with the naked eye and experience using an optical microscope. It is also possible to calibrate a optical microscope to identify the number of layers of graphene using the contrast between the bare substrate and the graphene.

To test the quality of the graphene, tapping mode atomic force microscopy is employed. Tapping mode is used so that the shear forces do not destroy the graphene. A repulsive regime is used to access the thickness of the graphene, an attractive regime is also used to reveal the presence of contaminants on the surface of the sample. Organic contaminants from the exfoliation process sometimes remain and are difficult to remove from the sample, these contaminants will reduce the quality of the graphene and can cause devices created on such areas to fail. The best way to counteract these contaminates is to avoid them completely. The AFM is a powerful analysis tool, however for testing for contamination its weakness is its maximum scan size. This is best used for the area of interest on the sample as scanning surrounding areas would require multiple scans to be preformed. Multiple scans would prove to be far too time consuming, however the detection of surface contaminants is still an important step in the isolation of graphene. A simple way of detecting contaminates on a large scale is the use of image enhancement, using simple histogram corrections on images of samples taken through an optical microscope. A before and after image is shown in 2.3, as this shows that the contrast of regions of contaminates are greatly increased. The contrast of graphene is also increased using this method, these appear as dark regions with a sharp boundary. Regions where graphite

has been deposited onto the substrate appear as bright regions with a sharp boundary. Contaminates however, appear as purple regions without a sharp boundary.

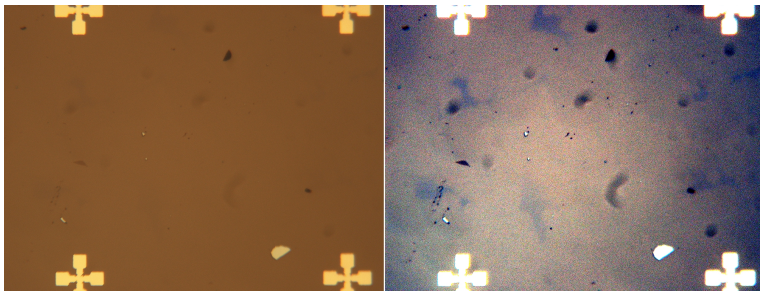

Figure 2.3: Substrate before and after image manipulation performed to enhance the visibility of contamination on substrate surface.

2.2 Optical identification of graphene on atomically flat insulators

Although silicon is a standard material used in microelectronic and is able to easily reveal the presence of graphene optically, it is less suitable for work with graphene in other ways. The problem with silicon is the oxide layer the graphene is deposited onto. Although the oxide layer is insulating it is also amorphous, when graphene is deposited onto this layer, the graphene deforms to follow the contours of the oxide surface. This deformation reduces the quality of the graphene, perturbing its electrical properties, thus making it less desirable for experimentation. This observation leads to the conclusion that substrates comprised atomically flat insulators will produce graphene with far better electrical properties than silicon substrates. Theses substrates however have their own set of problems, the foremost being that they are transparent, therefore making the isolation of single layer graphene much more difficult. As well as these substrates being atomically flat, they can also have other interesting features, which are discussed in later chapters. Recently it has been shown that graphene can be observed optically on mica using cross-polarized light [38], in a similar method cross-polarized light was used to isolate graphene on other optically transparent atomically flat insulators. This method uses an optical microscope with cross-polarizing filters and is illustrated in figure 2.4. Graphene is exfoliated onto a substrate and placed graphene side down onto a black background. The second polarizer is rotated until the contrast of graphene is maximised.

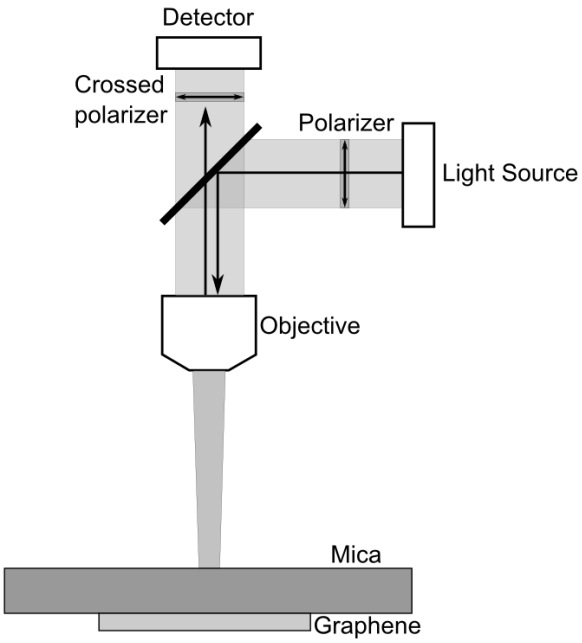

Figure 2.4: Figure shows the experimental setup for the optical identification of graphene on mica, with the use of polarizing filters.

This method of isolation can be explained with birefringence, the birefringence of a cleaved mica slab is approximately $4 \cdot 10^{-3}$ [38]. The light linearly polarized along the bisector of the mica optical axes becomes elliptically polarized upon transmission through mica. The change in polarization depends on the wavelength of light and the thickness of the mica substrate, however this will not be considered in detail, as it is unimportant for the isolation of graphene. First the contrast is considered in the absence of the polarizers, in a similar way to that of a silicon/silicon dioxide substrate. The Fresnel reflection coefficient at an interface is given by

$$r = \frac{n_1 - n_2}{n_1 + n_2} \tag{2.4}$$

Where n_1 and n_2 are the refractive indices of the media forming the interface. The change in polarization of light from the top surface of mica, taking into account equation 2.4 is negligibly small and the second polarizer can be adjusted to block it, effectively enhancing the contract of graphene.

$$C^* = \frac{(I_{mica\_bottom} + I_{mica\_top}) - (I_{graphene} + I_{mica\_top})}{I_{mica\_bottom} + I_{mica\_top}}$$
$$= \frac{I_{mica\_bottom} - I_{graphene}}{I_{mica\_bottom} + I_{mica\_top}}$$

Where C^* is the contrast in the absence of cross polarizers, when the polarizer is adjusted to block the light reflected from the surface, this equation becomes

$$C = \frac{I_{mica\_bottom} - I_{graphene}}{I_{mica\_bottom}} \tag{2.5}$$

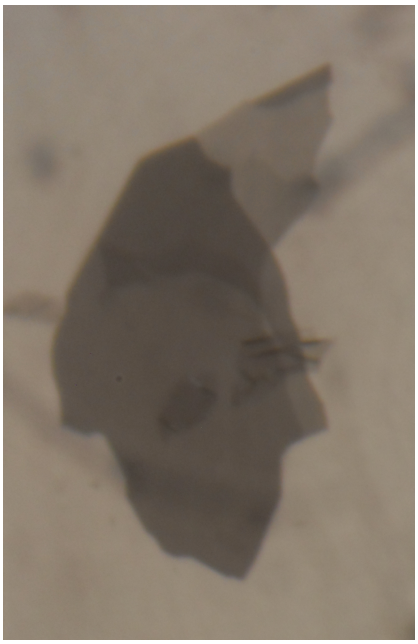

Figure 2.5: Figure shows an optical image of a region of graphene on mica. This region contains graphene with regions of differing thickness. Different thicknesses can easily be distinguished by contrast.

Figure 2.5 shows a graphene flake containing regions of differing numbers of layers, these different regions can easily be spotted due to the contrast difference between them. Single layer graphene can be observed as the near transparent region in the top right of figure 2.6a, Here one edge of the graphene is folded which is shown as the slightly darker boarder at the top of the flake. The dark regions at the bottom and top left of the image show regions of graphite. Figure 2.6b shows an enhanced version of the previous figure, this slightly increases the contrast of the graphene, however not as significantly as

graphene on a silicon substrate with a SiO_2 layer.

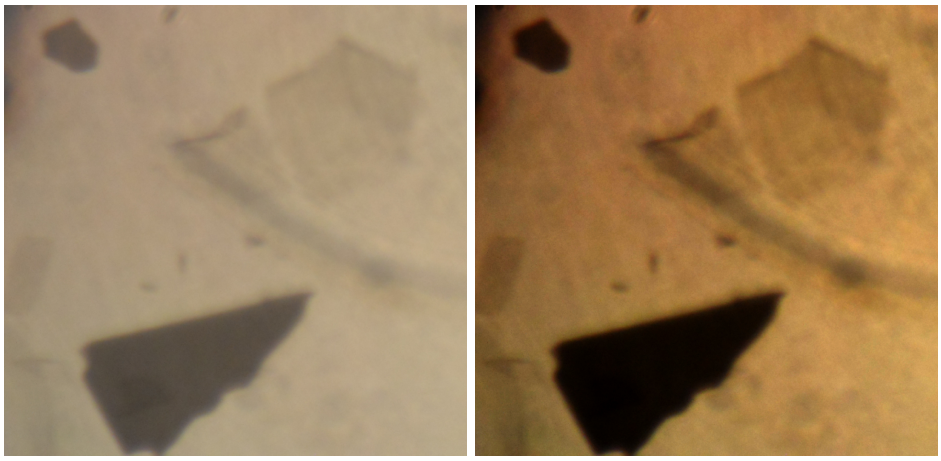

(a) (b)

Figure 2.6: Figure (a) shows an optical image of a region of graphene on mica. (b) is an enhanced version of (a), increasing the optical contrast of (a).

2.2.1 Condensation identification method

Another method of identification of graphene is proposed, the hydrophobic nature of graphene means that moisture will be expelled from its surface onto the surrounding substrate when exposed to moisture [39]. Here the sample is attached to the cold side of a Peltier module (shown in figure 2.7), the warm side is attached to a heat sink to dissipate heat. The sample was then cooled using the Peltier module. A Flow of nitrogen gas then flowed through a bubbler filled with DI water and onto the surface of the sample, the purpose of the bubbler was to introduce humidity to the gas flow.

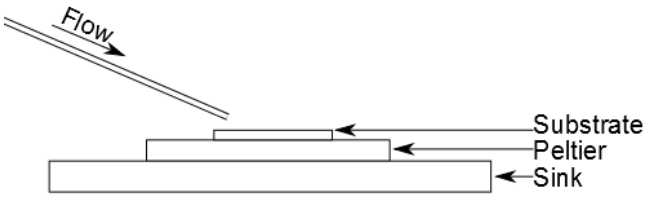

Figure 2.7: The setup used for the condensation identification method. The sample sits on top of a Peltier, which is connected to a heat sink. The heat sink keeps the warm side of the Peltier cool, allowing for the cold side to reach lower temperatures. Flow indicates a flow of nitrogen gas that has had its humidity increased.

The flow of hydrated nitrogen flowing onto the cooled sample causes condensation to form on the sample surface. The size of the condensation droplets was controlled using the flow time of the nitrogen and the temperature of the substrate, this created droplets with sizes ranging from approximately 5 to 20μm, which are visible through an optical microscope[40].

The droplets are expelled from the graphenes surface, thus creating an identification method. The goal of this method is to created bubbles of small size and high density, increasing the contrast between regions with and without graphene.

It was found that short flow times produced smaller droplets, whereas longer flow times allowed for the droplets to conjugate and grow in size. Cooler temperatures caused condensation to form without the nitrogen flow, this temperature corresponds to the critical condensation temperature of air. Below this temperature large sparse droplets tended to form. While droplets evaporated quickly with temperatures above this point.

The solution to this was to use a short flow time with the temperature above the critical point, to form small, densely arranged droplets. Once the droplets had formed, the flow of nitrogen was removed and the temperature of the Peltier was lowered to reduce the evaporation of the droplets. Figure 2.8 shows an example of this, the displacement in bubbles is easy to spot and therefore greatly reduces the time spent searching for graphene and graphene like materials.

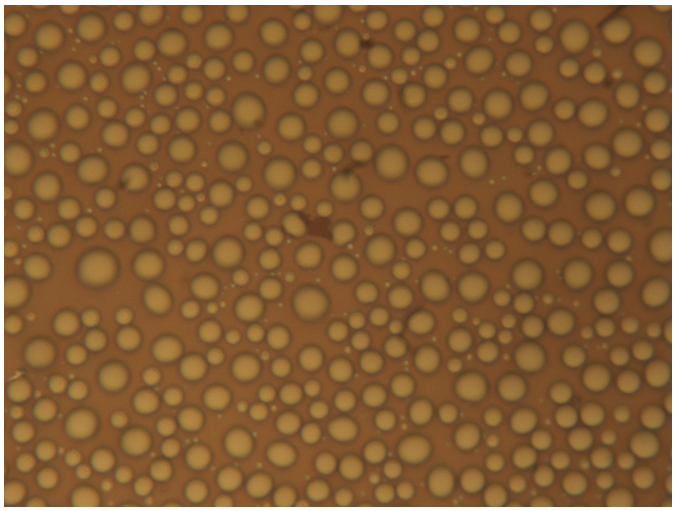

Figure 2.8: An optical image of moisture bubbles forming on the surface of a substrate, a thick graphitic layer can be seen in the centre. The hydrophobic nature of graphene causes the moisture not to form on its surface, therefore graphene can easily be identified by the absence of moisture bubbles.

As the bubbles size is fairly large, this technique works best when the graphene flakes

are significantly larger than the bubbles, here the graphene is of equivalent size of the bubbles and therefore the effect is less noticeable (Figure 2.8). This method has several problems however, firstly the technique is not compatible with all substrates, and for example the majority of the work in this thesis was performed on ionic crystals which evolve in humidity. Secondly, this method of identification does not reveal any information about the number of layers in the system, only that an area of graphene exists. Other methods would then be needed to identify the number of layer.

2.3 AFM characterization by tapping mode AFM

Tapping mode AFM involves the use of a piezo-drive to oscillate the AFM tip at near its resonant frequency, the range of forces acting on the tip then reveal information about the surface. This is widely used as it does not create frictional forces such as contact mode AFM, making the technique potentially non-destructive [41]. Characterization of graphene through tapping mode AFM is common practice, as it allows for topographic measurements over the entire graphene flake as well as being able to determine aspects of the quality of the graphene film. However, care must be taken with this method of characterisation as improperly chosen scanning parameters can introduce deviations in the measured thickness of graphene, as some literature is reporting deviations up to as much as 1nm [42].

The AFM cantilever-tip can be considered as a point-mass spring. In this way the motion of the tip can be described by a non-linear, second-order differential equation [43]

$$m\ddot{z} + kz + \frac{m\omega_0}{Q}\dot{z} = F_{ts} + F_0 cos(\omega t) \tag{2.6}$$

where F_0 and ω are the amplitude and angular frequency of the driving force. Q, ω_0 and k, are the quality factor, resonant frequency and the force constant of the cantilever. Here there are two forces acting on the tip, the driving amplitude $F_0 cos(\omega t)$, and the tip-sample interaction forces F_{ts}. There are different types of forces that can act upon the tip which arise from electrostatic interactions with the sample, attractive long range forces due to van de Waals interactions and short-range repulsive interactions from Pauli and ionic repulsion. Figure 2.9 shows a generic representation of the force-distance dependence of Lenard-Jones type, that contains long and short range forces. Without the tip-sample interaction the equation becomes that of a forced harmonic oscillator with damping.

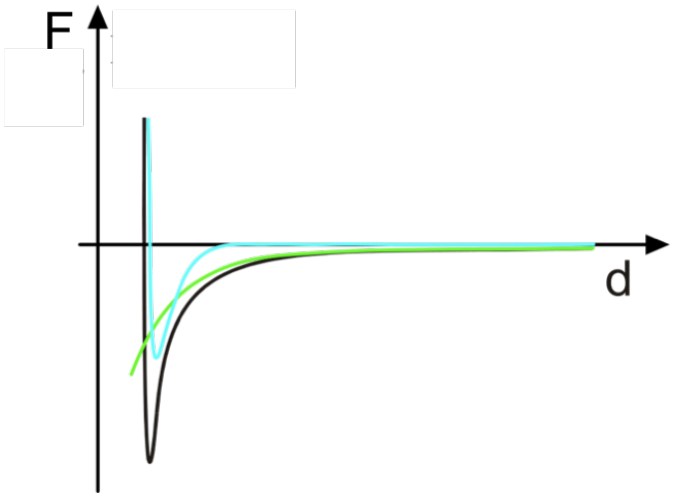

Figure 2.9: Figure shows the Lennard-Jones potential indicating the force on the AFM tip with tip-sample distance.

This leads to a solution for the amplitude of oscillation as a function of the ω excitation frequency of a Lorentzian type

$$A(\omega) = \frac{F_0/m}{[(\omega_0^2 - \omega^2)^2 + (\omega_0\omega/Q)^2]^{1/2}} \tag{2.7}$$

with phase shift given by

$$tan(\phi) = \frac{\omega\omega_0/Q}{\omega_0^2 - \omega^2} \tag{2.8}$$

where ϕ is the angle by which the driving force leads the displacement. Plotting both of these equations against driving frequency results in the curves shown in figure 2.10. When the driving frequency matches the resonant frequency of the tip the amplitude reaches is maximum and the phase is at 90°.

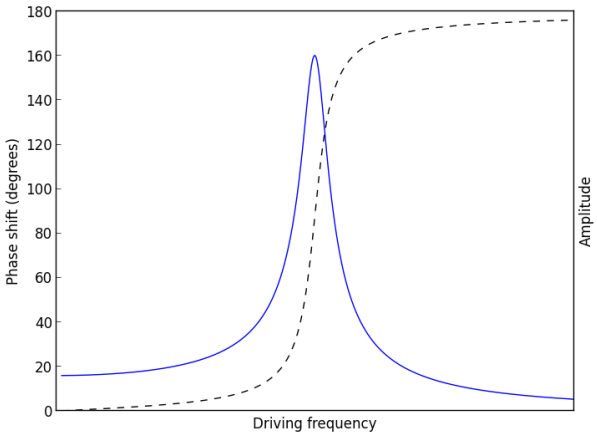

Figure 2.10: The phase (dashed) and amplitude (solid) of the oscillation of the AFM tip as a function of the driving frequency.

2.3.1 Amplitude modulation

Now that the mechanism of oscillation has been discussed, the effects of the tip-sample interaction force is discussed and how amplitude-modulated AFM is used to acquire topographic information about the sample. The method of measurement/scanning is based on measuring the amplitude of oscillation, while maintaining a fixed driving frequency.

Considering that the oscillating tip is subjected to a tip-sample interaction, then the tip-sample interaction force F_ts is added, and we are looking for a solution for the full equation 2.6.

The total force acting on the tip can then be expressed by

$$F = F_0 + \left(\frac{dF_{ts}}{dz}\right)_{z_0} (z - z_0) \tag{2.9}$$

for small displacements. This can then be used to calculate an effective spring constant of the oscillation.

$$k_e = -\frac{dF}{dz} = \left(k - \frac{dF_{ts}}{dz}\right)_{z_0} \tag{2.10}$$

resulting in a new effective resonance frequency.

$$\omega_e = \left(\frac{k - (dF_{ts}/dz)}{m}\right)^{1/2} \tag{2.11}$$

Therefore the forces acting on the tip at differing tip-sample distances alter the position

of resonance peak of the oscillator. Attractive and repulsive forces acting on the tip force the resonance peak to shift in different directions, an attractive force acts to lower the effective resonant frequency and a repulsive force raises the effective resonant frequency, as shown by figure 2.11

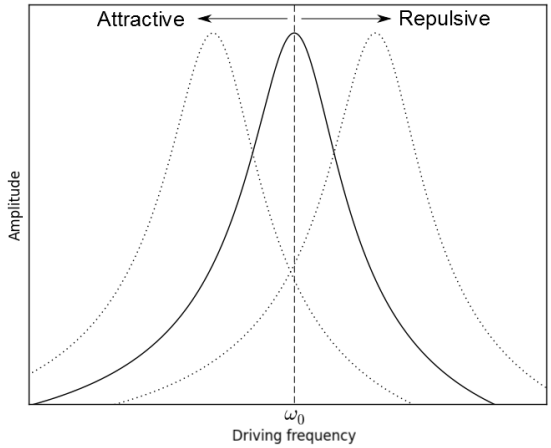

Figure 2.11: The shift in the tips resonance curve of the oscillating tip, under the effect of attractive and repulsive forces.

As the tip is being driven at a constant frequency, the shift in resonance will cause the oscillation amplitude of the tip to change. The system monitors the amplitude of the oscillation and attempts to maintain a constant amplitude while scanning.

Figure 2.12 shows the approach of the oscillating tip to the surface of the sample in terms of amplitude 2.12(a) and of force 2.12(b). Near the surface, as the tip further approaches the surface the force acting on the tip constantly increases, due to increasing atomic repulsion. This causes the effective resonant frequency to shift. As the AFM is driving the tip at its free amplitude resonant frequency the amplitude of oscillation will greatly decrease, due to this effective resonant frequency shift.

Further away from the surface, the tip only experiences attractive (long range) forces from the sample. This can be observed in figure 2.12(b) where the force acting on the tip goes negative. This causes a dip in the amplitude as the tip approaches the sample. The reason for this dip is due to the effective resonant frequency shifting from below the unaffected resonant frequency to above it. As the attractive and repulsive forces begin to balance each other the resonant frequency is brought back to its normal value, increasing the amplitude. Contact time between the tip and sample is also shown, figure 2.12(c). Here it can be seen that as the tip approaches the surface, the contact time

slowly increases, however there is a large reduction in contact time as the attractive and repulsive forces begin to balance and a contact time of zero where there is no repulsive force.

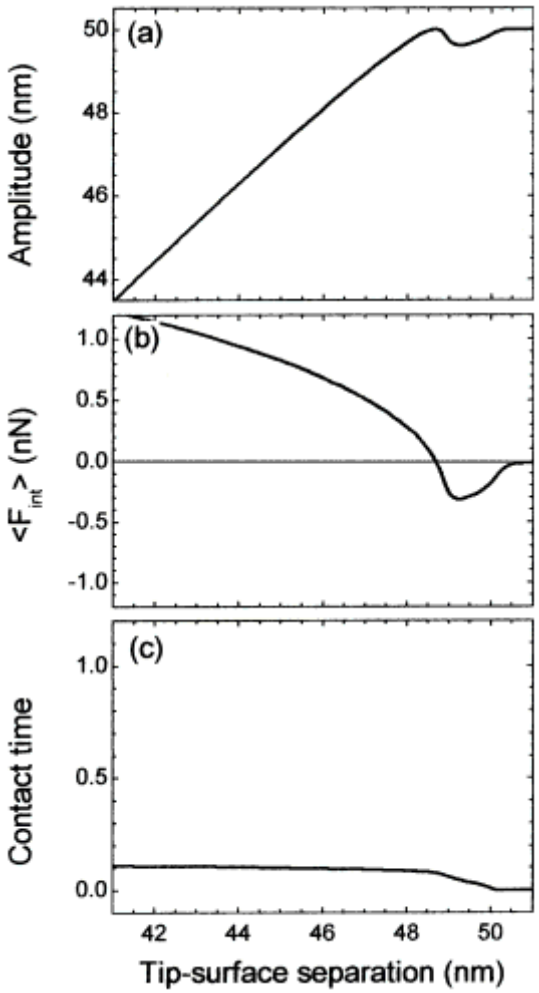

Figure 2.12: Figure (a) shows the tips amplitude of oscillation for tip-sample distance, (b) and (c) show the average force experienced by the tip during an oscillation period, and the contact time with the surface for the same tip-sample distance respectively. Figure taken from reference [43].

In amplitude modulated-AFM, as the topographic measurement is based on the measurement of the amplitude, care must be taken when determining heights from topography. If a sample surface contains regions where the nature of strengths of forces differs (such as a surface containing different materials), the imposed condition of scanning with

constant amplitude can cause an inaccuracy in the height measurement.

2.3.2 Graphene thickness from tapping mode AFM

Phase imaging can be used to monitor the amplitude of the forces the tip is experiencing. By combining information from figures 2.10 and 2.11 forces that in average are of attractive type (non-contact mode) give a phase larger than 90° (consistence with the driving frequency being above the resonance frequency), while forces that are in average repulsive give a phase lower than 90°, (consistence with the driving frequency being below the resonance frequency. This implements a new trace to the tapping mode scan, here lag between the signal that drives the cantilever and the cantilever oscillation is measured. As the cantilever is already being driven for tapping mode, phase imaging can be implemented without any disruption to the topography scan and is generally good practice to use as it reveals more information about the sample, such as areas of contamination.

It can be demonstrated that the thickness of a graphene layer can be measured as a range of values depending on the scanning parameters (up to 1nm about the true value), compared to the substrate, therefore proper precautions needed to be taken to ensure an accurate height measurement. Taking into account the phase scan, it is possible to monitor the forces the tip is experiencing as it moves across the samples surface. The scan can be set up so that the phase remains approximately constant across two regions of interest, in this way the forces remain similar between the two regions ensuring for an accurate reading of height. Figure 2.13 shows scans taken in attractive (b,d and f) and repulsive (a,c and e) regime, respectively over mono (a and b), bi- (c and d) and tri- (e and f) layer graphene. Images were obtained using a constant amplitude set point, with two different free amplitudes. Topographic scans show the height difference between scans in attractive and repulsive regimes. Scans in repulsive regimes approximate the accepted values of graphene thickness (approximately 0.34nm per layer), whereas the scans in repulsive regimes deviate by over 1nm[42].

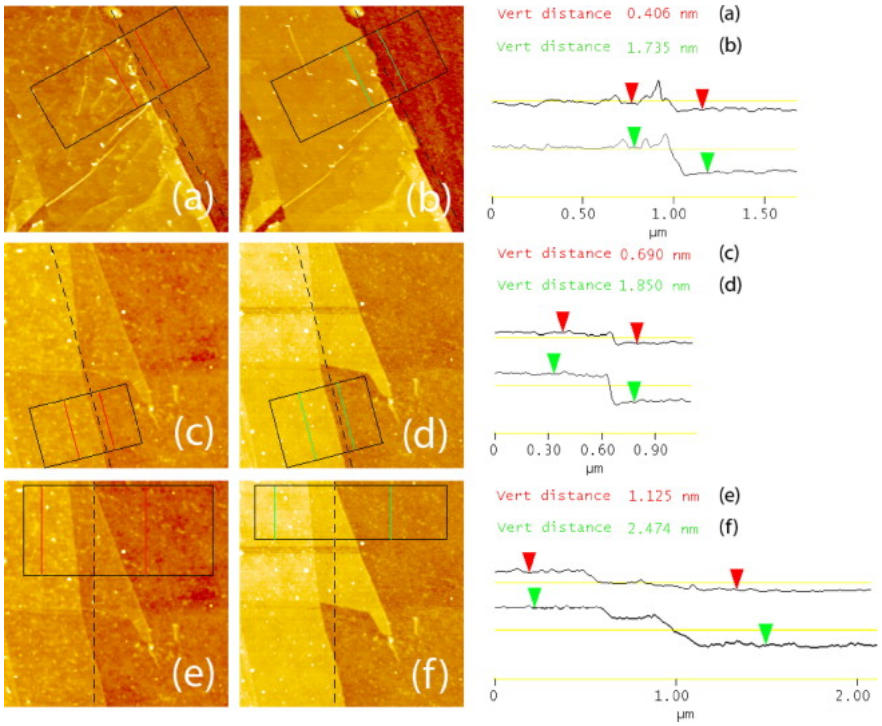

Figure 2.13: Scans in attractive (b,d and f) and repulsive (a,c and e) regimes over mono (a and b), bi- (c and d) and tri- (e and f) layer graphene. Topographic scans show the resulting thickness obtained in each case. Repulsive scans approximate the accepted values of graphene thickness (approximately 0.34nm per layer), whereas the attractive scans deviate by over 1nm. Figure taken from reference [42].

It was also reported that scanning between two different areas of graphene was not affected in this way. This is due to the two different areas being made of the same material, here the forces wont change relative to each other, therefore resulting in no observed thickness difference. When measuring the thickness of graphene layers throughout this thesis, phase is always taken into account. Figure 2.14 shows an enhanced optical image of multilayer graphene on a KBr substrate, the dotted box highlights a region scanned by the AFM and shown in figure 2.15.

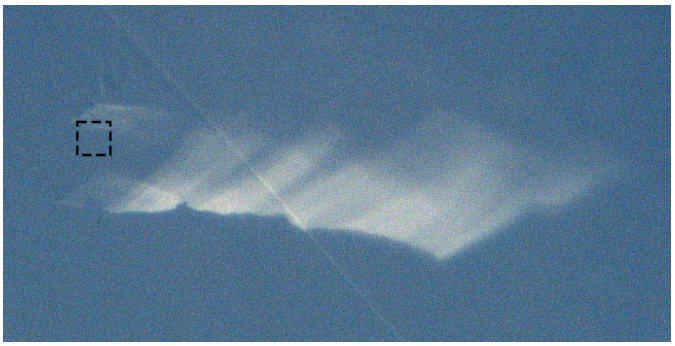

Figure 2.14: Optical image of a region of multilayer graphene on a KBr substrate. Image is enhanced to increase the contrast between the substrate and the graphene. Dotted box shows the region which was scanned with an AFM.

This scan of this region will be used to demonstrate the phase imaging, showing a scan where the phase remains relatively constant across the two regions and an accurate height trace being obtained. Figure 2.15 shows the topographic and phase image of a graphene-substrate boundary. We note that this boundary is easier to spot in the phase scan running almost horizontally across the figure.

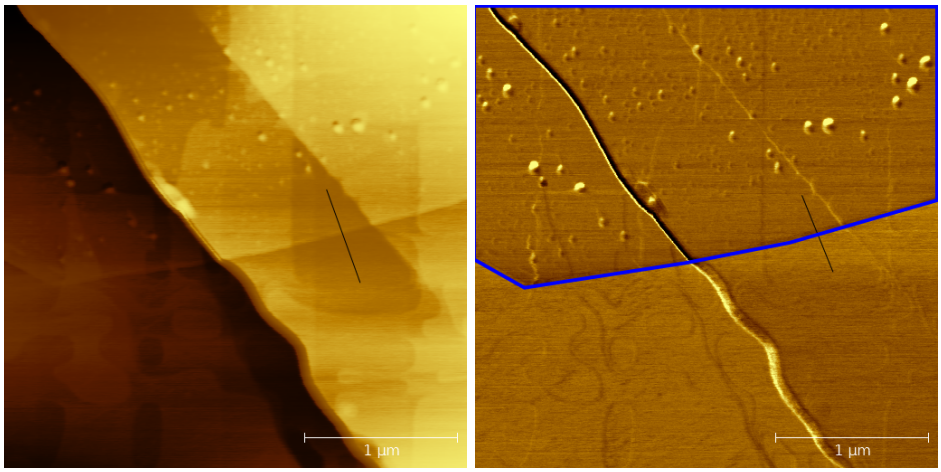

(a) (b)

Figure 2.15: Topographic and phase images taken from the dotted region from figure 2.14. The contained region is part of the graphene flake, while the remaining part of the image is the substrate. Black lines indicate where data is extracted from to measure the height and phase change between the substrate and graphene.

The data between regions will now be extracted for both the topographic and phase images. The region where the data is extracted from is marked with a black line on both

images, this region was selected as there are no nearby terraces which could affect the topographic or phase data. Figure 2.16 show the extracted data from both scans, the phase data shows that the phase remains relatively constant across both regions (less than a few degrees), indicating that the forces remain similar between regions. As the phase remains similar the extracted height data is accurate, and indicates that the region of graphene is two layers thick.

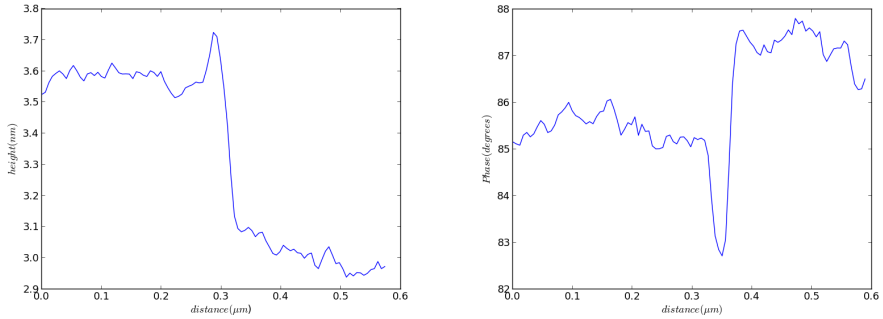

Figure 2.16: Data extracted from the height and phase scans shown in 2.15, here graphene is on the left of both graphs. The height trace clearly shows that the graphene is two layers thick, while the phase measurement shows that the measurement is performed in the repulsive regime(below 90 degrees) while maintaining a low deviation of phase (below a few degrees) ensuring that the forces remain similar across regions.

Chapter 3

Ionic crystals as substrates for graphene

This chapter will discuss the charge distributions produced by defects and nanostructures on the surface of ionic crystals. These can occur naturally but randomly after cleaving or can be induced in a controlled fashion by various irradiation processes. Various types of charge distributions will be described in a hierarchical manner, according to the expected magnitude of the local potential perturbation they can produce. The situations occurring in various environments will also be considered, whether in vacuum or under environmental conditions. Graphene deposited onto such substrates would experience substantial doping from the surface potential produced by the surface of the crystal.

3.1 Charge distribution and electrostatic field on non-polar planes of ionic crystals

The simple cubic structure of potassium bromide (KBr) shown in figure 3.1 will be considered, the lattice consists of positively charged potassium atoms (Red) and negative charged bromine atoms (Blue).

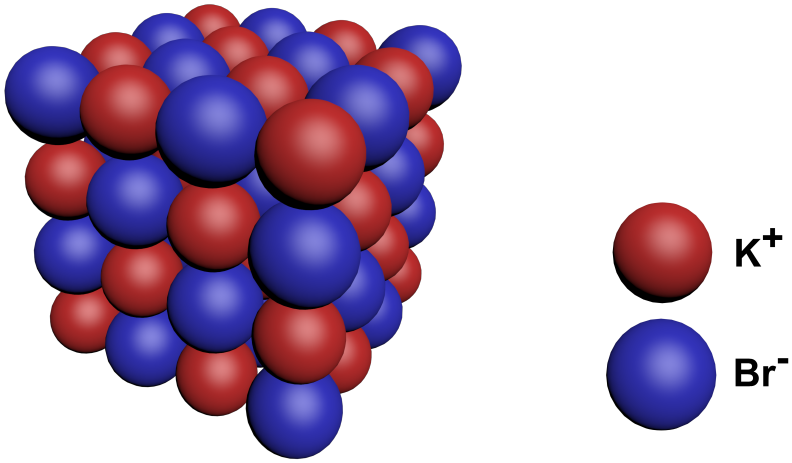

Figure 3.1: Potassium bromide lattice.

On such a surface, positive and negative charges are disposed in a periodical manner, and each of the ions feels a symmetric environment of ions of opposite charge. Such a charge distribution will not produce a sizeable potential perturbation at distances larger than an inter-atomic distance, d, as argued below. To begin with, a distribution of same sign point charges separated by distance d in both x and y directions (shown in figure 3.2) is considered. For this lattice the electric field is given by equation 3.1 [44]

$$E_z = \frac{\sigma}{2\epsilon\epsilon_0}\left[1 + 2\left(cos\frac{2\pi x}{d} + cos\frac{2\pi y}{d}\right)e^{-2\pi z/d} + ...\right] \tag{3.1}$$

Here higher order terms are decay much more rapidly with distance z. The first order term is the same as a uniform surface potential. The second order shows that the periodic extent of the field decays rapidly, with a decay length of $d/2\pi$. This will now be used to calculate a lattice of repeating positive and negative charges, where the net surface charge becomes zero. This approximates well the situation at non-polar low index ionic surfaces. A negative charge is placed in the centre of each square shown in figure 3.2(b). By superimposing the charges, the field at a positive site (at $x = 0$ and $y = 0$) is [44]

$$E_z = +(4q/\epsilon\epsilon_0 d^2)e^{-2\pi z/d} + \tag{3.2}$$

And at a negative site (at $x = \frac{1}{2}d$ and $y = \frac{1}{2}d$)

$$E_z = +(4q/\epsilon\epsilon_0 d^2)e^{-2\pi z/d} + \tag{3.3}$$

Here the field decays exponentially away from the surface, thus yielding a short range field.

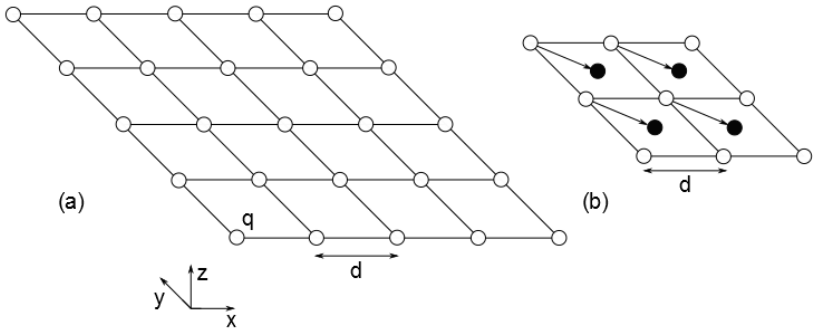

Figure 3.2: Graphical representation of a lattice of charge, (a) with the same polarity charge and (b) with opposite polarity added to the centre of each square.

These simple electrostatic considerations show that a perfect non-polar ionic surface is not expected to induce a significant potential on a graphene sheet placed at approximately 0.34 nm above it, and even less in subsequent graphene layers within a multi layer system.

3.2 Step edges

3.2.1 Low-index step edges

Now terraces in the crystal surface are considered, here their step edges can exist as high or low index. As low index planes require low energy to cleave, their formation occurs readily on the crystal surface. These low index planes can produce non-polar and polar edges, for example figure 3.3 (a) non-polar and 3.3 (b) polar edges.

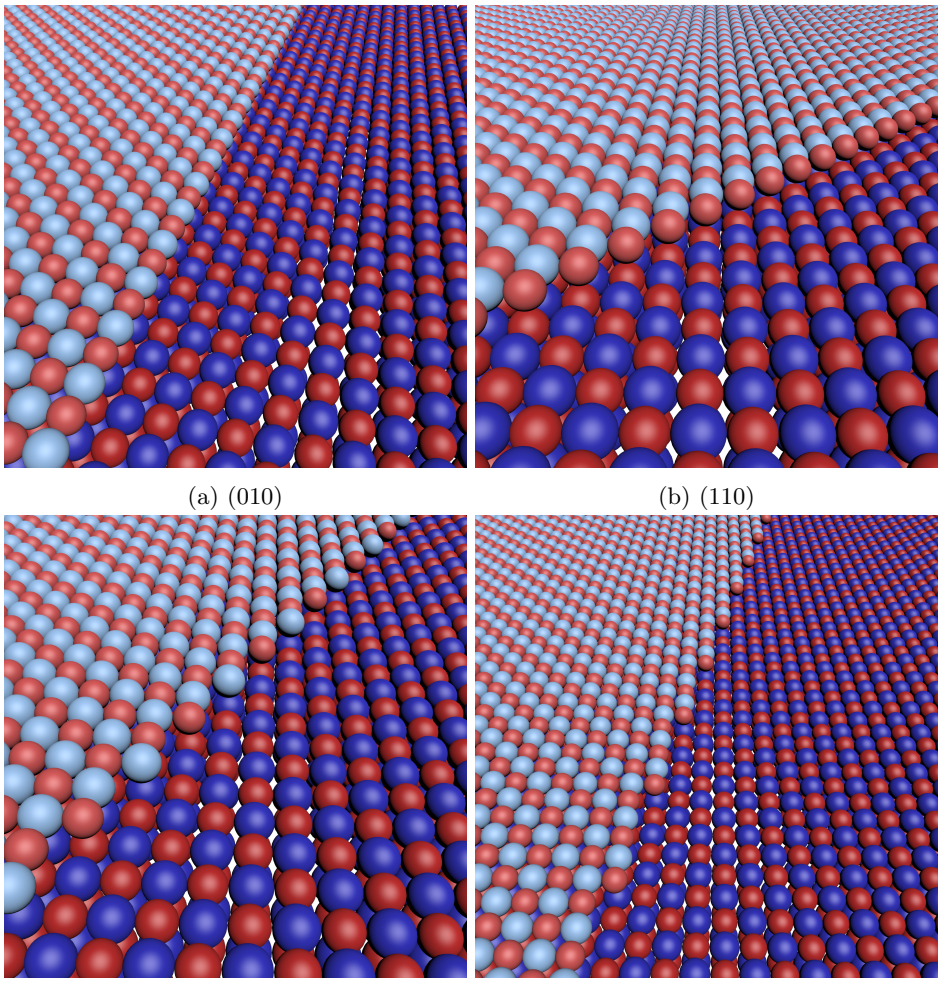

(a) (010) (b) (110)

(c) (120) (d) (150)

Figure 3.3: Examples of low index terrace edges forming on the (001) surface of KBr. With (a) and (b) showing examples of non-polar and polar edges.

Figure 3.4 shows an AFM scan of many terraces forming along the same plan in KBr. Within KBr these terraces can stretch for tens of microns, however the formation of this surface is heavily influenced by the cleavage angle and energy of the crystal.

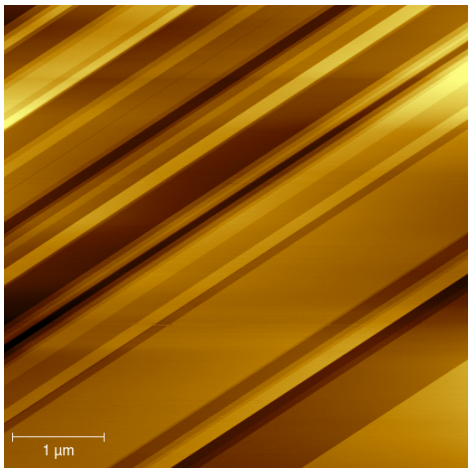

Figure 3.4: AFM topographic scan of an example of a cleaved surface which is highly ordered over many microns.

3.2.2 High-index step edges

High index step edges can be shown to be made up of a succession of (100) and (010) edges. Due to the uncompensated charge from the polar kinks involved in their formation, these edges produce significant local potential. Figure 3.5 shows an example of such an edge, where a edge close to that of (110) is made up of a succession of (100) and (010) planes due to polar kinks in the (110) edge.

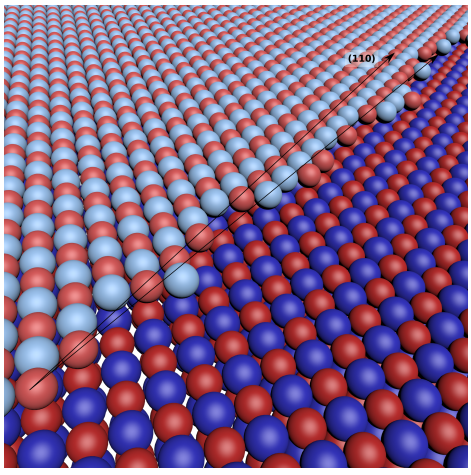

Figure 3.5: Example of a high indexed plane made from series of smaller (100) and (010) planes.

3.2.3 Polar kinks

Polar kinks can from in the terrace step edges, this is where an atom or multiple atoms are missing from the step edges. This creates an area of large surface charge due to the uncompensated charge on the atoms around the kink. Figure 3.6 shows a bromide atom missing from the step edge, this creates a vacancy which is surrounded by potassium ions, creating an area of positive charge over the kink

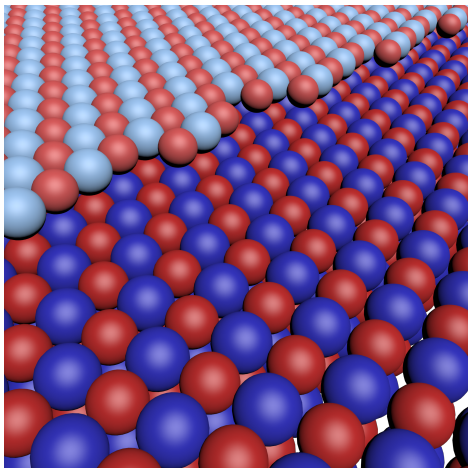

Figure 3.6: A bromide atom missing from a (150) terrace edge, creating a simple edge kink.

A much more complex kink is shown in figure 3.7. Here a kink is shown in a (110) edge. Many atoms are missing in this kink creating significant charge to develop around the kink. Kinks of this magnitude have been observed experimentally on islands on NaCl crystals using atomic resolution force microscopy techniques [45].

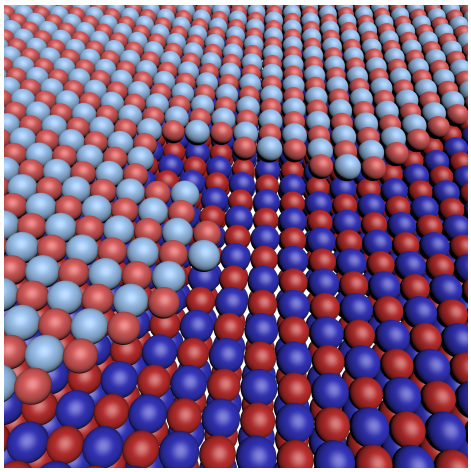

Figure 3.7: Example of a large polar kink on a (110) edge.

Pits, protrusions and high index steps and have been shown to be produced during the cleaving along the (001) face of KBr face, these are produced through a succession of polar kinks

3.2.4 Pits and protrusions

Pits and protrusions have the greatest potential to create the largest surface over a minimal lateral extent[46] (compared to other surface formations). The surface charge can build to greater values than that of a terrace edge as depending on the formation of the pit or protrusion, multiple terrace steps build to a point in a cone like shape. The surface charge produced by such a structure is much greater than that of a step edge due to the large number of uncompensated charges around the edges, the magnitude of this surface charge will be dependant on the density of terrace steps within the pit or protrusion

3.3 Theoretical evaluation of potential distribution around non-polar and polar step edges

Non-polar edges are formed from an equal ratio of positive and negative charges and therefore does not produce significant surface field due to the charge compensation. Polar edges however, are formed from a non-equal ratio of positive and negative charges. This produces uncompensated charge around the step, thus producing a larger surface potential than that of non-polar steps. Calculations using density functional theory (DFT)[47][48][49] estimated the effect of such a step on graphene[50]. As an example,

DFT calculations were performed on a (220) edge with a graphene overlayer (shown in figure 3.8). The potential at the surface of graphene reached an approximate value of 0.2eV, indicating significant surface potential produced by these type surface features. A charge dipole model was also applied to this edge [51]. Here atoms were described by dipoles in a fully classical method, this produced a value of potential at the graphenes surface of approximately 0.5eV.

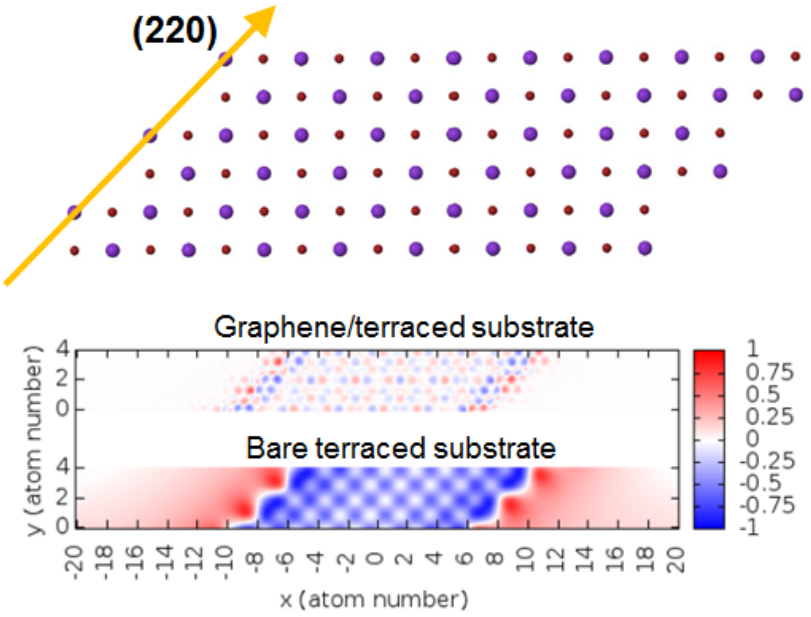

Figure 3.8: Lattice showing a (220) terrace edge, with the accompanying DFT calculations using graphene as an over layer[50].

Edges with foreign species can also form[52][46][53]. Edges become decorated with atoms with higher ionic charges, such as Ca^{2+} and Mg^{2+}, which exist as intentional or unintentional dopants in these crystals. Due to the higher ionic charge, these ions induce larger surface potentials, Figure 3.9 shows an atomic resolution non-contact AFM image of such an edge, where the edge is decorated with atoms of higher ionic charge (indicated by the bright points).

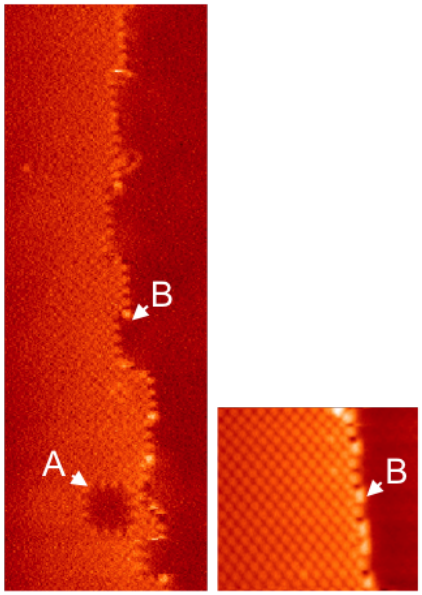

Figure 3.9: Step edges of a KBr terrace showing non-polar regions, polar-kinks (A), and foreign species (B).

3.4 Environmental effects

The exposure of ionic crystals to humidity will now be discussed[54][55][56]. The effects of humidity on ionic crystals alter the properties of the surface charge distributions developed, therefore it is an important topic when considering graphene which has been deposited onto substrates cleaved under non-vacuum conditions. It is a well known phenomenon that freshly cleaved ionic crystals are always negatively charged at their surface. This is due to the formation of an electric dipole layer at the surface of the crystal, known as the Debye-Frenkel double layer. This is formed due to the difference between the formation energies of the cation vacancies and that of the anion vacancies at the surface

3.4.1 High humidity

Ionic crystals have two critical humidity points (characteristic to the crystal), referred to as point A and point B. These critical points define the humidity at which there is significant increase in ion dissolution from the ionic surface. Point A defines the humidity at which there is preferential dissolution of anions, due to water adsorption. This preferential dissolution of cations is what causes the negative to positive shift in surface charge over time when exposed to environmental conditions, this also increases the surface conductance. When the humidity rises above point A, the dissolution of cations causes

terrace step motion. The motion of the steps is slow at this point, as it is limited by the dissolution of the anions. Above critical point B, both positive and negative ions dissolve at similar rates, this removes the negative charge accumulated at the step edges and causes rapid step displacement. For KBr the point A occurs at 55% relative humidity respectively [57]

3.4.2 Low humidity

For relative humidities below the critical point A for the crystal, surface potential changes are localised to the terrace step edges. This is believed to be due to preferential dissolution of cations occurring near the step edge. The solvated ions remain near the step due to its negative charge. This leads to the creation of a dipole at the step, depicted in figure 3.10[57]. The dipole formed points perpendicular to the surface of the crystal, creating a significant amount of surface charge along the step edge, while maintaining a narrow lateral extent.

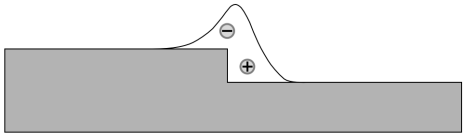

Figure 3.10: Example of a dipole forming at a step edge from ions where the substrate has been exposed to humidity.

This is the situation in which our experiments fall, as our samples were produced and measured in non-vacuum conditions. Other experiments in the group dealt with the case when step edges were reconstructed by annealing in vacuum, which resulted in a situation like in figure 3.9. To demonstrate the formed dipole at the edge of the terrace, scans were taken of freshly cleaved (111) surface of calcium fluoride (CaF_2) and repeatedly scanned over time in a low humidity. Calcium fluoride was used as it is less soluble in water, therefore the formation of the dipole will take longer than that of potassium bromide. Figure 3.11 shows two images, 3.11a directly after cleavage of the crystal and 3.11b one hour after the initial cleaving of the crystal. Nucleation points also occur on the flat of the terrace, which can be seen in figure 3.11b. As the tip passes over the mobile ions along the step, the ions move towards/away from the tip depending on the electrostatic interaction. This creates the enhanced step edge seen in 3.11b.

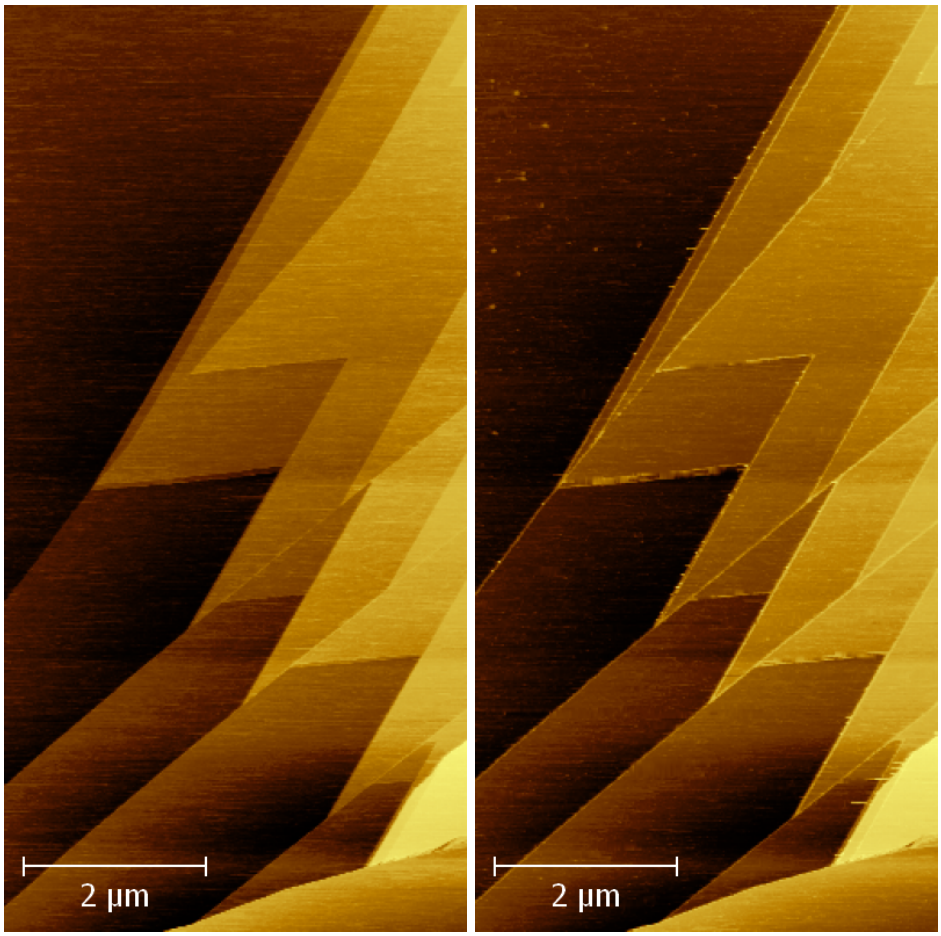

(a) Directly after cleavage. (b) One hour after cleavage.

Figure 3.11: Topography scans over the (111) surface of CaF_2 3.11a directly after cleavage and 3.11b one hour after cleavage.

Even at a low humidity there is still slow step displacement and step rounding. This step rounding is shown in figure 3.12 In figure (b) there is significant step rounding, this formation is possible due to the large steps formed from cleavage of the crystal, seen here passing from the top to bottom of the scan. These steps will be several atomic layers in height, thus creating a highly reactive surface for the atmospheric humidity to react with. There is also an occurrence of two screw type dislocations within this scan (expanded image of a differing screw defect shown in figure 3.12(c)), this is where a part of the lattice is formed with a slip in the surface, part of the layer is moved out of its atomic plane with the other part remaining in the plane. This type dislocations could be interesting to study, as the changing height with its lateral extent would create an

interesting potential distribution, however the formation of a screw defect is rare thus making the change of graphene being exfoliated onto a screw defect extremely rare

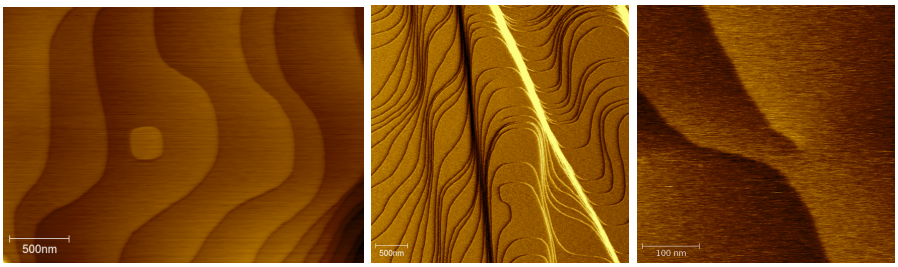

(a) (b) (c)

Figure 3.12: Examples of terrace step rounding, with a screw defect shown in (c).

Chapter 4

Scanning force microscopy (SFM) techniques

This chapter introduces the experimental techniques used to investigate local potential perturbations induced in graphene layers by bottom-up nanostructured ionic substrates. Fundamentals of Electrostatic Force and Scanning Kelvin Probe microscopy (EFM and SKPM) are given, as well as a description of the way SKPM is implemented in our measurement set-up. Factors that affect the measured quantities are also discussed, in particular in relationship to the measurement of a surface potential originating from a localized source and its decay with distance to the surface.

4.1 Electrostatic force microscopy (EFM)

Electrostatic force microscopy (EFM) is a non-contact AFM technique which involves the use of an oscillating biased, conductive tip to map potential variations on the surface of a sample. The technique measures the electrostatic force gradients between the tip and sample induced by interactions between the samples and the biased tip. Attractive and repulsive forces between the tip and the surface induce phase variations between the driving mechanical oscillator and the oscillation of the tip. The degree of phase shift is dependent on the magnitude of the surface charge. The EFM technique works by measuring the phase shift of the biased tip as it raster scans across the samples surface.

The technique involves a two-step process. First a topography line scan is taken across the surface in a standard tapping, amplitude modulated AFM mode (section 2.3.1). This first line scan is used as feedback for a EFM scan over the same topographic line of the sample, as shown in figure 4.1. For the EFM scan, the tip is passed over the same line,

but this time with the tip biased and raised at a constant distance Δz above the previous scan. The distance Δz is sufficiently large so that the tip does not make contact with the surface, so that the measurement does not include short range interactions and is based solely on electrostatic interactions. Electrostatic forces between the tip and the sample cause phase shifts between the oscillation of the cantilever and the oscillation of the drive. The degree of phase shift is proportional to the difference in potential between the sample and the tip.

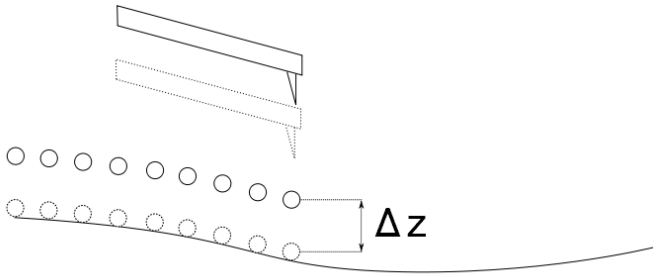

Figure 4.1: Topography scan in amplitude-modulated tapping mode, followed by EFM scan.

For the second (EFM) scan the cantilever is driven mechanically at its free oscillation amplitude and biased with a DC bias. This can be modeled as a parallel plate capacitor-like set up, where the plates are the oscillating tip and the sample. The potential energy stored within this system is given by

$$U = \frac{1}{2}CV^2 \tag{4.1}$$

The force is given by the derivative of the potential U as a function of position.

$$F = \frac{1}{2}\frac{dC}{dz}V^2 \tag{4.2}$$

This force depends on the applied voltage and the capacitance, which are independent and dependant on distance respectively. The changes in the force will modify the resonant frequency of the cantilever and will be observable as a phase shift of the cantilever. For small force gradients, the resonant frequency and phase shifts can be expressed as the following [58]

$$\Delta\omega = -\frac{\omega_0}{2k}\frac{dF}{dz} \tag{4.3}$$

and

$$\Delta\phi = -arcsin\left(\frac{Q}{k}\frac{dF}{dz}\right) \tag{4.4}$$

where k is the spring constant and Q is the quality factor. Since

$$\frac{dF(z)}{dz} = \frac{1}{2}\frac{d^2C}{dz^2}\Delta V^2, \tag{4.5}$$

the phase shift becomes

$$\Delta\phi = -arcsin\left(\frac{Q}{k}\frac{d^2C}{dz^2}\Delta V^2\right). \tag{4.6}$$

The phase shift is a function of the potential difference ΔV between the tip and the sample. The resolution of the EFM phase method is determined by the lateral distribution of d^2C/dz^2 and can reach lateral resolution of better than 20nm [59].

4.1.1 EFM Spectroscopic measurements

This set up allows for spectroscopy measurements to be taken of the surface potential of the sample. This involves positioning the tip above a point of interest on the sample and measuring the phase of the cantilever as a function of tip bias. For small values of bias, these measurements appear parabolic, with the phase shift always negative as d^2C/dz^2 is positive. Obtaining the actual surface potential of the region involves relating the phase shift of the spectroscopy measurement to the tip bias according to a parabolic law [60].The maximum of the curve is the difference between two work function, that of the tip, and that of the surface. Taking spectroscopic measurements over different regions of the surface charge will result in spectroscopic curves where the shape of the parabola and the position of the maxima of the curves are different.

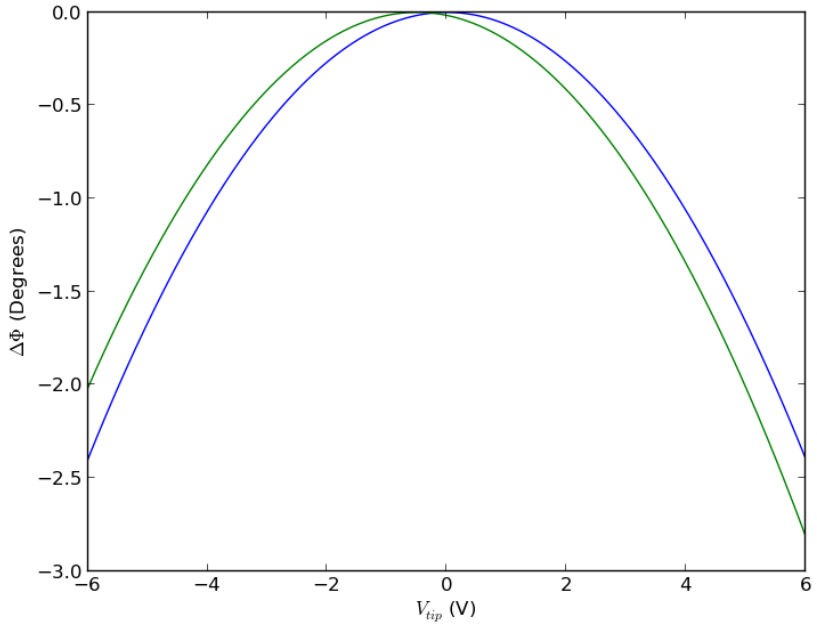

Figure 4.2: Spectroscopic measurement of different regions with different surface potentials, showing the shift between measurements.

Not only is this measurement useful for studying the surface potential under the tip, it can also be used to increase contrast on the EFM images. After spectroscopic measurements have been taken on the regions of interest, the contrast of the EFM scan can be significantly increased and even inverted by selecting a tip voltage that causes the biggest phase shift between the regions. The procedure has been applied to measurements on graphene regions of different number of layers as discussed in section 5.2.1.

4.2 Scanning Kelvin probe microscopy (SKPM)

Kelvin probe is a non-contact variation of AFM. Similar to EFM the surface potential of the sample is measured, however this technique allows for continuous mapping of the surface potential. This method is based on the force between the tip and sample rather than the force gradient as with EFM. This reduces the resolution of the technique when compared with EFM due to the long range property of the Coulomb force, as stray fields from all parts of the whole tip and cantilever can contribute to the total interaction [59]. As with EFM, Kelvin probe imaging involves a two scan process. The first scan records the topography of the sample. The topography scan is then retraced with a height of Δz

above the topography trace (figure 4.1). On the Kelvin probe scan there is no mechanical drive of the tip, instead a AC and DC bias is applied to the tip. The electrostatic interaction between the tip and sample induced by the AC bias drives the oscillation of the cantilever. The total bias in the system is given by the sum of the AC driving bias V_{AC}, the DC offset bias V_{DC} and the surface potential difference V_{SP} which the method measures.

$$V = V_{SP} + V_{DC} + V_{AC} \sin \omega t \tag{4.7}$$

Using equation (4.2) one states the interaction force

$$F = \frac{1}{2}\frac{dC}{dz}\left(\left[(V_{DC} - V_{SP})^2 + \frac{1}{2}V_{ac}^2\right] + 2\left[(V_{DC} - V_{SP})V_{AC}\sin(\omega t)\right] - \left[\frac{1}{2}V_{AC}^2\cos(2\omega t)\right]\right) \tag{4.8}$$

This equation shows that there are three components to the force, the first with no frequency dependence, the second at the AC frequency ω, and the third occurring at twice the AC frequency 2ω. For Kelvin probe, the component at ω is the most important as it depends on the potential difference between the tip and the sample. The signal at the frequency ω is isolated using a lock-in amplifier. The DC bias is then adjusted until the signal at ω is minimised: at this point the DC bias matches the surface potential difference and can be directly recorded. With this method V_{SP} is mapped independently of the scanning parameters [61]. The frequency of the driving AC voltage is set to the frequency of the first resonance of the tip (typically 300kHz). This high modulation frequency allows for shorter integration times of the lock-in amplifier without loss of precision [62].

4.2.1 Implementation of SKPM

The SKPM is digitally implemented within an Asylum Research MFP-3D system. Figure 4.3 shows a schematic of the digital implementation of the Kelvin probe. The dashed line outlines the lock-in amplifier used to measure and control the Kelvin probe. An AC bias is generated with a DC offset and sent to the tip, passing through a digital to analog converter, this bias is used to cause the tip to oscillate. The voltage from the photodiode within the AFM is passed to an analog to digital converter. This signal is passed to two frequency mixers (crossed circle) using the i and q components of the reference signal. The signal is then sent through low pass filters (LPF) to remove noise. The lock-in then measured a two component signal against the reference signal V_d, for the 'in-phase' component

$$i = V_d cos\theta \tag{4.9}$$

and the 'quadrature' component

$$q = V_d sin\theta \tag{4.10}$$

where θ is the phase difference between the reference and the measured frequency. From this the magnitude (R) of the voltage can be calculated by

$$R = \sqrt{i^2 + q^2} \tag{4.11}$$

where $R = V_d$, and the phase (θ) by

$$\theta = arctan\left(\frac{q}{i}\right). \tag{4.12}$$

These two parameters are then used to describe the surface, where magnitude relates to the surface potential. The q component of the signal is then sent to the feedback loop, which instructs the instrument on how to generate the tip bias.

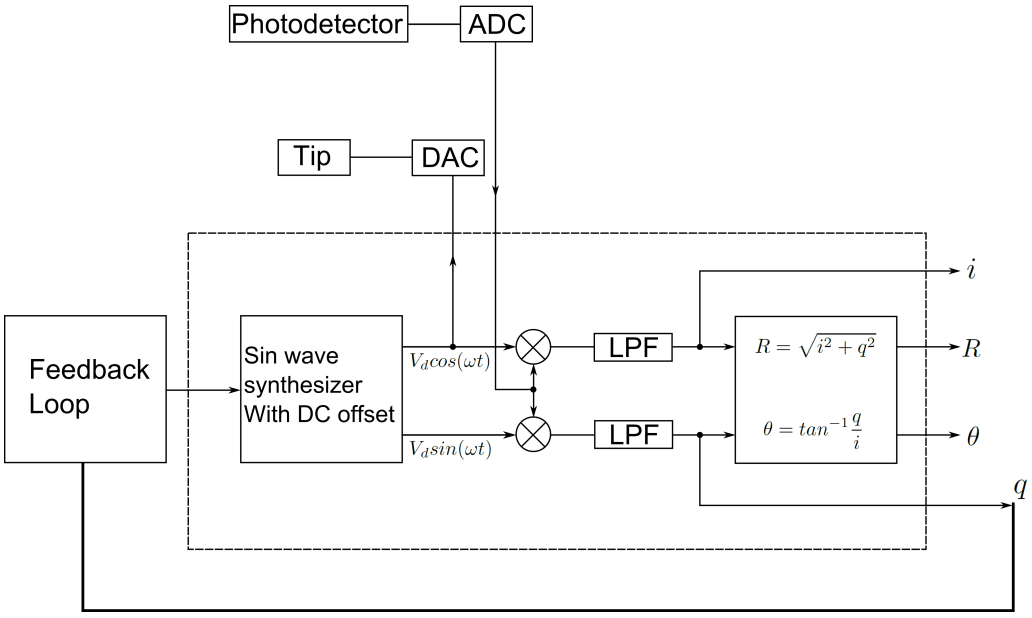

Figure 4.3: Schematic of the Kelvin probe system.

4.3 SKPM measurement procedure

Several steps are involved in the preparation and scanning when using scanning Kelvin probe microscopy. For conductive samples, grounding is essential to remove the build up

of charge from the surface during the scan. For semiconducting and insulating samples however, grounding is not required. Specialised tips are required for Kelvin probe, these tips must be coated with a conductive material, such as iridium. The shape of the probe will be a limiting factor on the sensitivity of the technique. Keeping the apex radius of the probe low is essential to obtaining high lateral resolution, as the electrostatic interaction becomes weaker with distance between charges, therefore a blunt probe will decrease resolution as more of the probe interacts strongly with the sample.

First the target location is located using standard amplitude-modulated tapping mode AFM, with the tip mechanically tuned to -5% of its resonance frequency, this increases sensitivity of measurements as any change in the tip's frequency results in a larger change to the oscillation amplitude than that of a tip tuned to its resonance frequency. This increases the sensitivity of the measurement is demonstrated in figure 4.4. The two blue lines represent the change in the effective resonance point and the two Lorentzians represent two tunes of the AFM tip, one on the resonance peak (solid) and one slightly off the resonance peak (dotted). The shift of effective resonance occurs over a much steeper gradient on the off peak tune, and therefore any change to the effective resonance peak results in a much larger change to the oscillation amplitude and thus allows for a much more sensitive scan.

Once the target location is found and scanned using tapping mode AFM, the location is then analysed for its suitability for Kelvin probe. Several factors can make a site unsuitable for Kelvin probe. Factors such as contamination and density of terraces in the ionic substrates cannot be observed optically and can only be observed after navigating the AFM probe to the target location. This first step is generally done using a standard non-conductive probe over several locations. Once the best location is chosen, the probe is replaced using a conductive probe and re-navigated to the location. As conductive tips wear extremely fast when compared to non-conductive tips it is generally advantageous to use non-conductive tips for initial navigation. Also a fresh, sharp conductive tip will also produce electric field lines with a smaller lateral extent, increasing resolution of the Kelvin probe scan.

Next, several steps need to be preformed in preparation for the Kelvin probe scan. First a force spectroscopy measurement is taken, the oscillating tip is pushed closer to the sample. A trigger point is given, once the deflection falls below the trigger point the tip is retreated to a position above this trigger point given by the user. The trigger point is set around the same value as that of the scanning amplitude to ensure that minimal damage is caused to the sample and tip. The height above the trigger point is used to tune the tip for the Kelvin probe scan. This tune differs from the mechanical tune, an AC and DC bias are applied to the tip with no mechanical drive. The DC bias induces an electrostatic interaction with the substrate and the AC bias induces a

secondary electrostatic interaction which causes the tip to oscillate. For a conductive substrate the DC bias is generally set to +3v as this will induce an opposite charge on the surface of the sample, however for an insulating sample the potential on the tip must differ from the charge on the surface of the sample to induce a potential gradient. The AC bias is set to the same as the frequency of the mechanical drive with an amplitude of 1-3v. The AC is now tuned to -5% of its resonance, which will be similar to that of the mechanical tune.

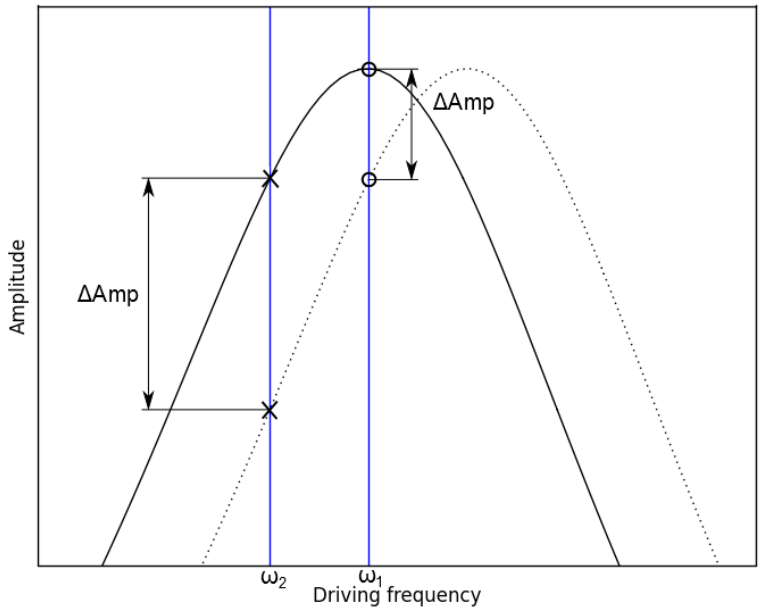

Figure 4.4: The amplitude change with shifts in frequency for an on resonance tune and a slightly off resonance tune

The surface potential is determined by the potential on the tip when the tip potential and the potential below the tip are in equilibrium, at this point the oscillation of the tip is nullified at its first resonance frequency, where the tip is driven with an AC excitation. The input for the feedback loop to control the tip potential will now be discussed. To explain the feedback input, a sample with a surface potential of -1V is considered. Figure 4.5 shows a graph containing the phase and amplitude of the tip electrically driven with a DC voltage sweep of +- 5V.

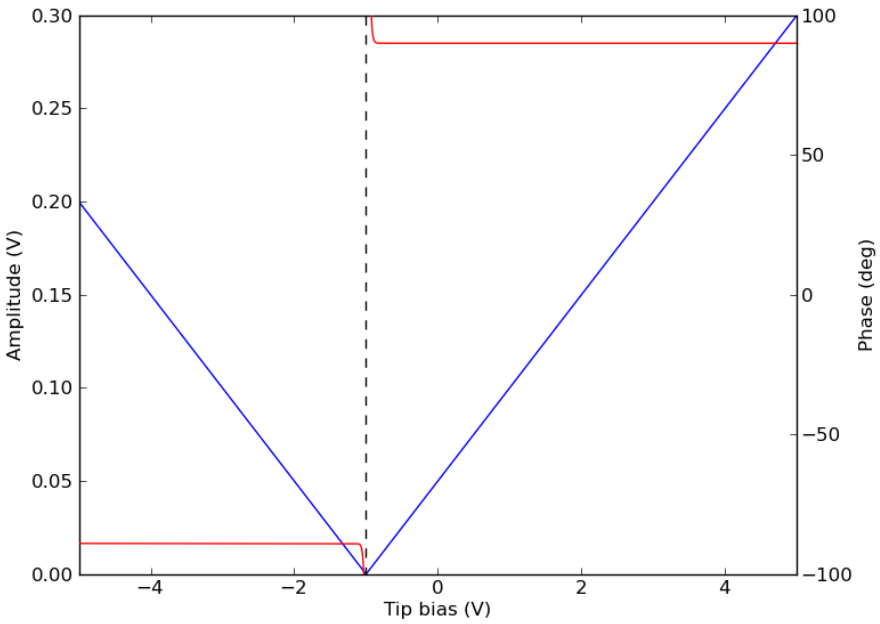

Figure 4.5: The amplitude (Blue) measured by the photodiode and the phase (Red) of the cantilever with tip bias.

As the surface potential is -1V, the amplitude is nullified at -1V as shown in figure 4.5. This appears to be appropriate for the feedback input as the response to tip bias is linear however, the amplitude always increases whether the difference between the tip bias and surface potential is positive or negative, therefore it's difficult to determine in which way the tip must be biased to nullify the oscillation. A similar result comes from the phase measurement, it's possible to determine the direction in which the tip must be biased as the phase jumps from -90 to 90° as is passes through the nullification point. The phase however does not yield information on the bias change required to reach this point. Figure 4.6 shows a graph displaying i and q against the tip bias. The Red line shows q, here when the tip is in phase with the driving oscillation, q becomes zero. As q is linear and passes through the zero to become negative, both direction and the difference to the zero point can be determined, therefore making this a perfect input for the feedback loop.

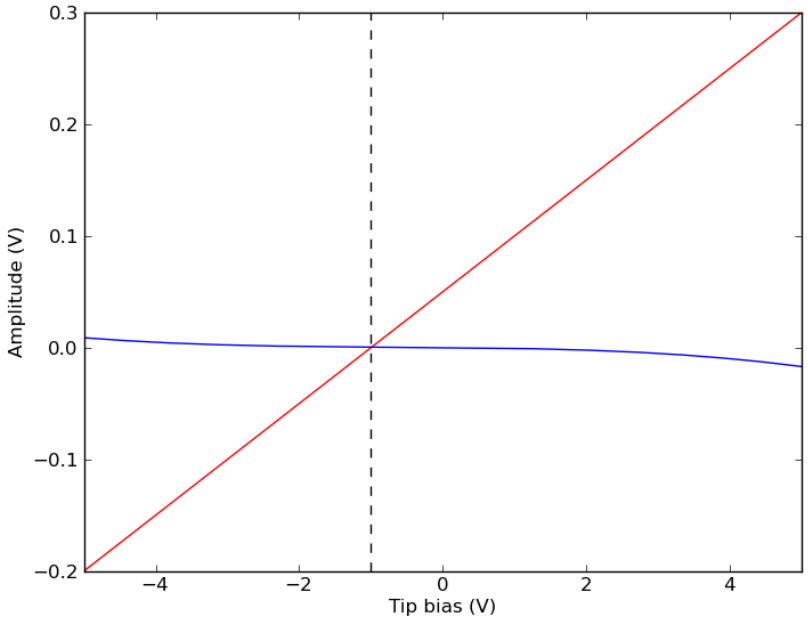

Figure 4.6: The in-phase (i) (Blue) and quadrature (q) (Red) components of the cantilever with tip bias.

The phase offset between the topography and Kelvin probe scan is now calculated with the tip at a set height above the surface so that the electrostatic interactions between the tip and sample take place. During the Kelvin probe scan this phase offset is accounted for. This is essential for the feedback loop to function correctly. The amplitude-distance spectroscopy measurement (figure 4.7) is now used to calculate the distance between the tip and the sample during the topography scan. The flat region of the graph is where the free air oscillation amplitude of the tip is smaller than the tip sample distance. When the tip sample distance is brought below the free air oscillation amplitude, the oscillation amplitude decreases due to the shift in the resonance curve induced by the interaction with the sample. The gradient of this region (shown by the fit in figure 4.7) is called the inverse optical lever sensitivity (InvOLS), this term yields information about how the amplitude of oscillation of the cantilever changes in nm with the voltage measured on the photodiode. Therefore it is possible to estimate the distance between the tip and sample from the amplitude of oscillation measured at the photodiode For example, in figure 4.7 the InvOLS can be calculated from the inverse gradient of the dotted line. In this case the InvOLS is calculated to be 248nm/V. This would give a tip sample distance of 186nm with a set point of 750mV.

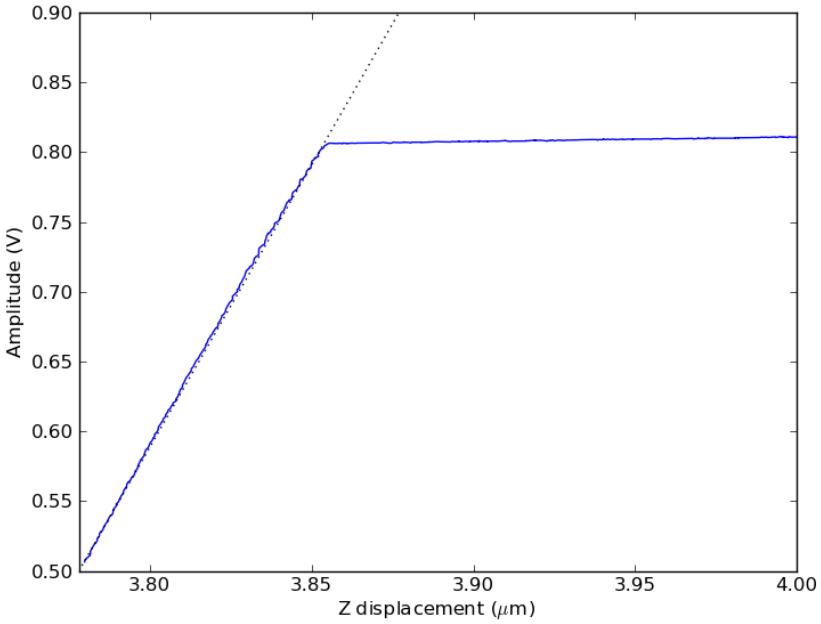

Figure 4.7: Force curve, amplitude against distance (Solid line). The gradient (Dotted line) where the tip begins to interact with the surface is used to calculate the optical lever sensitivity (OLS).

On the Kelvin probe pass the amplitude of oscillation of the tip will greatly decrease when compared to that of the topography trace, due to the different mechanisms of excitation of the cantilever. The parameter Δz is used to alter the tip sample distance during the Kelvin probe pass. As shown in figure 4.1, Δz is the distance between the zero oscillation point of the cantilever during the topography scan and that of the Kelvin probe scan. The value for InvOLS is now used with the current set point to assign an appropriate Δz. Due to the lateral spread of charge at distances above the surface, the tip should be brought close to the surface to increase lateral resolution. Kelvin probe can now be preformed.

The potential measured during the Kelvin probe pass is not that one would measure at the surface level, but the potential decay at the current z position of the tip. For a localised charge distribution, a very rough approximation would be to divide the source potential V of the surface by z, the position of the tip above the surface. Having the tip at distance z above the surface also effects the lateral extent of the Kelvin probe image, the larger z distance the larger the surface features will appear, therefore to obtain a high resolution scan a low z must be sought. The limit on z is approximately 10nm, below

that and the oscillations of the electrically driven cantilever begin to interact with the sample.

The size of the tip is also a factor influencing the resolution of the Kelvin probe image. The 1/z dependence relies on the assumption that the two interacting charges are point charge. This produces a problem with the measurement as the tip is significantly large. Even when only considering the very end of the AFM tip there is still the fact that the tip is not atomically sharp. Cantilevers used for electric measurements in AFM tend to have a tip curvature radius much larger than standard tips as they require a coating of a conductive material. The tips used in these measurements have a tip curvature radius of 33$\pm$ 10 nm, this is only their starting condition and will wear to a larger radius with use. There could then be additional contribution to the electrostatic interaction from the tip, which is 17.5$\pm$25 μm in height which is also attached to a cantilever of 240 μm long and 35 μm high. When including all of these interaction and the 1/z fall off of the potential. The lateral extent of the measured potential in the Kelvin probe image is significantly larger than that of the source potential distribution at the surface level. Chapter 6 will relate these two quantities, measured (at a given z above the surface) and real (at the surface level) through rigorous mathematical analysis.

Chapter 5

Surface potential variations in graphene induced by nanostructured crystalline ionic substrates

We used Electrostatic Force and Kelvin Probe microscopies (EFM and KPM) to investigate few-layer graphene (FLG) domains on top of ionic crystals. Step edges, pits and protrusions within the ionic surface create sizeable and local perturbations of the surface potential of graphene overlayers. These were stronger in FLG with up to three layers, and become considerably screened in thicker layers. As KP measurements were taken at distances to the sample that are in the range of a few nm and beyond, a true value of the surface potential generated by the source nanostructure is not directly measurable, but would need to be inferred from the experimental distance dependency of the surface potential and via further modelling (as performed in Chapter 6). Hence, surface potential-distance measurements were performed over FLG flakes of various thickness on top of ionic crystals terraces. As an order of magnitude, simple considerations point to nanostructures in the ionic surfaces being able to generate several tenths of eV of potential perturbation within monolayer graphene.

5.1 Kelvin probe of cystal surfaces

5.1.1 Ionic crystals

Using Kelvin probe microscopy, the surface potential of the sample can be accessed. However, the potential measured is the convolution of many effects. To obtain the maximum lateral resolution of the charge profile the tip of the Kelvin probe must be as close as possible to the samples surface. Figure 5.1 shows an example of a KBr surface topography (a) with its associated Kelvin probe image (b) of the cleaved KBr crystal, where the tip was positioned at 9nm above the surface for the Kelvin probe pass. The Kelvin probe image shows the variation in potential created by the step edges shown in the topography trace.

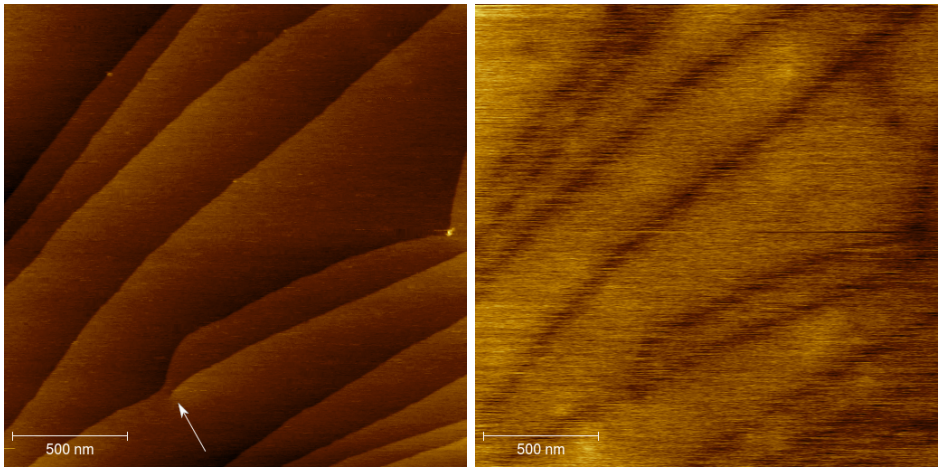

(a) (b)

Figure 5.1: (a) shows the topography image of a freshly cleaved (001) surface of KBr, (b) shows the associated Kelvin probe image: a potential has developed around the step edges, which can be seen by the contrast in the Kelvin probe image. A screw dislocation can be seen in (a) and has been marked with an arrow.

The potential measured during the Kelvin probe pass is not that of the charge at the surface, but that of the decay of the charge from the surface at the current height of the tip. The rate of decay is dependent on the shape and lateral size of the surface charge, therefore it is not only the measured potential that changes with height but also its the measured lateral size. Therefore to obtain a high resolution Kelvin probe scan a low scanning height must be used. Figure 5.2 show the topography image over a freshly cleaved KBr substrate. Kelvin probe image were then taken over the same area (figure 5.3). The profile shows the terrace heights within the scan, all of the terraces apart from

one are one atom high.

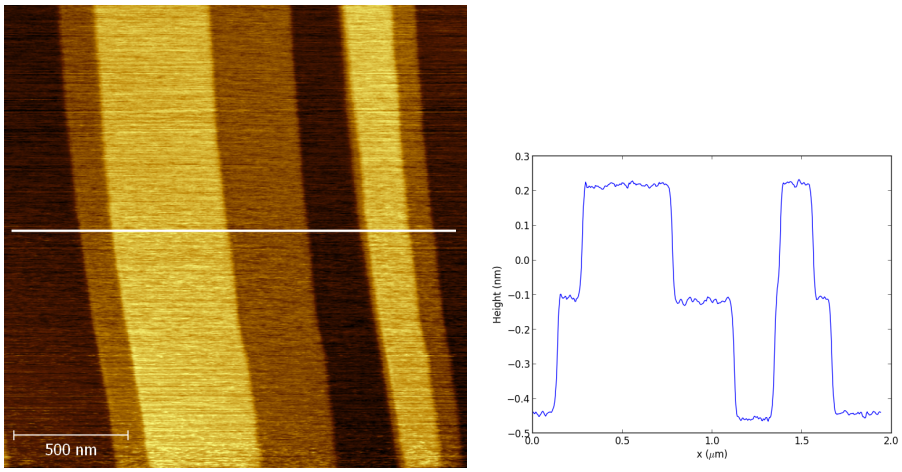

Figure 5.2: Topography scan of a freshly cleaved KBr substrate with a line profile showing atomic height terraces. White line in the topography scan marks where the line profile was taken.

The Kelvin probe scans of the same area as in figure 5.2 are now shown, The scans are taken at increasing heights (Δz) above the surface (figures 5.3), the height (Δz) being determined according to the procedure discussed in section 2.3.2. The sharpest of these scans is that corresponding to $\Delta z = 11$nm, where the tip is closest to the surface; beyond that and the measured lines of potential begin to broaden, which can be observed in the later images as features begin to merge into each other. The falloff of potential relative to the surface can be observed with increasing Δz, as the potential profiles over the terraces edges become less distinguished and begin to disappear into the background noise.

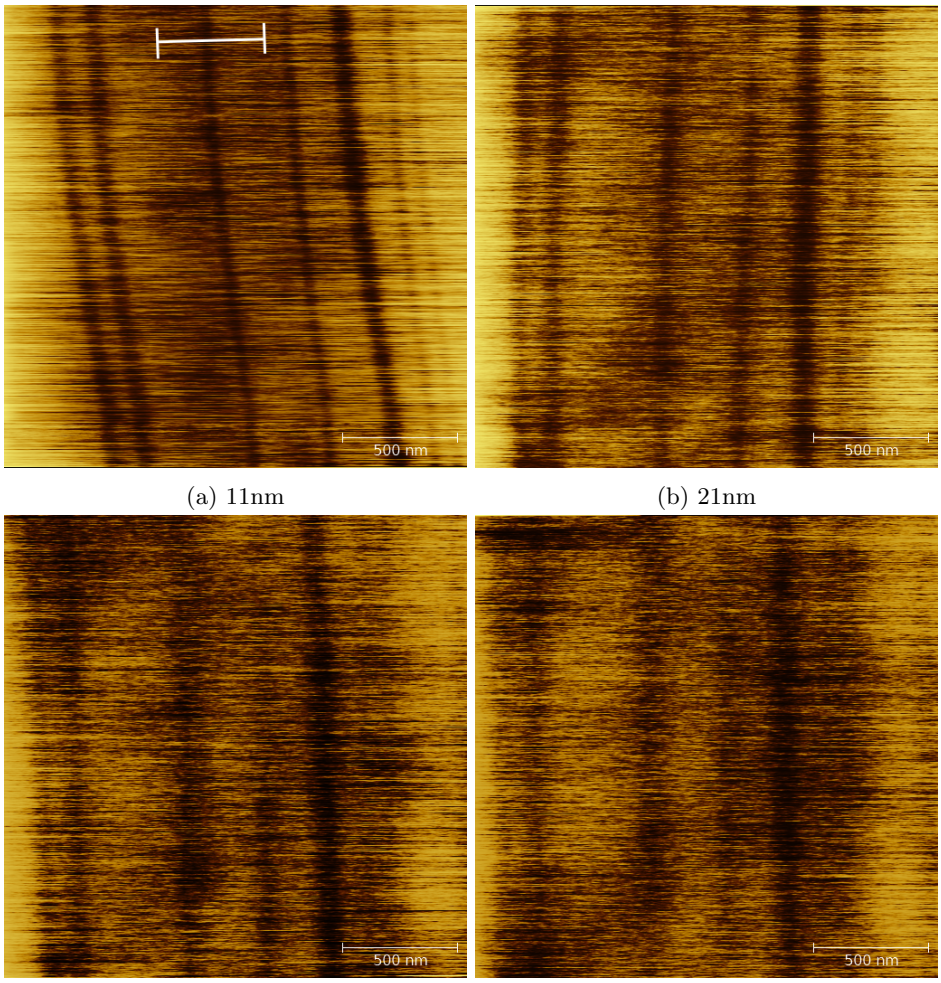

(a) 11nm (b) 21nm

(c) 31nm (d) 41nm

Figure 5.3: Four Kelvin probe scans over the same area as the previous topographic scan. The distance Δz between the tip and sample is 11, 21, 31 and 41 nm respectively. White line on image (a) indicates the terrace edge where data was extracted from for figure 5.4.

The magnitudes of the measured potentials were then extracted from the scans using Gaussian fits and then were plotted in figure 5.4 to show observed potential fall off from the surface. Here the data was extracted from the set of scans shown in figure 5.3, the extracted data was taken from a single terrace (indicated by the white line shown in figure 5.3(a)). This data was averaged along the length of the terrace to remove noise, and fitted with a Gaussian to obtain the magnitude of the potential. The data point pairs at each height are due to there being a trace and retrace scan taken at each height. A fitting attempt is made using 1/z, as 1/z is the approximate decay of potential generated

from a point charge. Clearly this fit does not give a good estimation of the potential decay, and therefore is unsuitable for calculating the value of the source potential at the surface as the deviation at the surface between the fitted and real value will likely be significant. The reason for 1/z not being a good fit to the data is most likely due to several factors, including the tip size and the lateral size of the surface potential. A more detailed investigation into the nature of the potential decay is discussed in chapter 6.

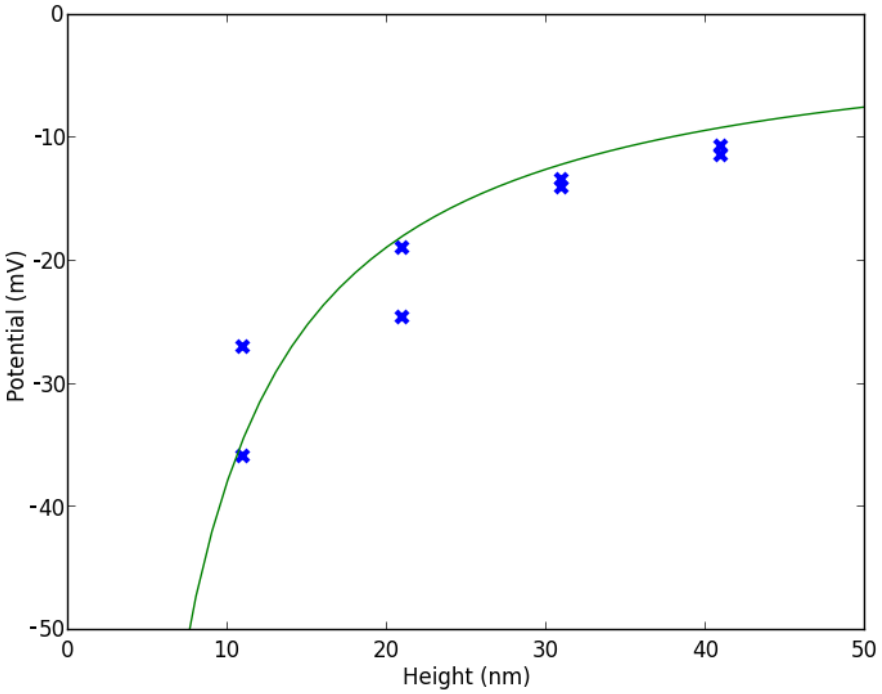

Figure 5.4: Experimental decay of potential with height above the surface (extracted from the Kelvin probe image 5.3).

Figure 5.5 shows another sample of the same substrate. This time measurements were taken over a double atomic step, with a much greater number of scanned heights. Here the minimum height reached was 8nm and measurements were taken every 2nm to a total height of 36nm. Once again this has been fitted with 1/z and once again it is noted that this fit most likely deviates heavily at the surface compared to the true value of the surface potential.

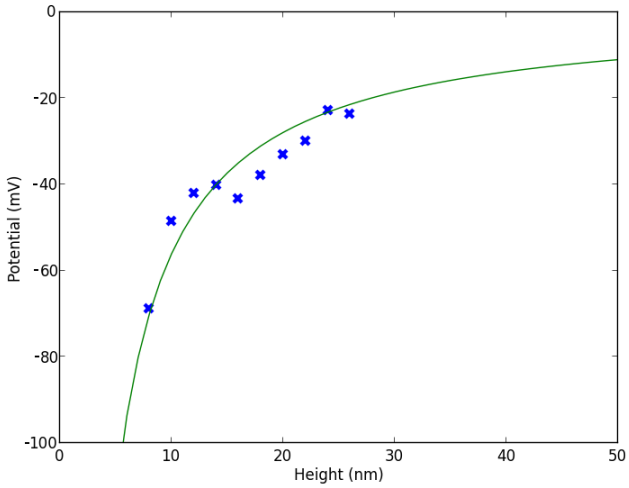

Figure 5.5: Potential data taken with 2nm height steps above a double atomic step in a KBr surface. This set of data was taken from another set of Kelvin probe scans (not shown).

5.1.2 Comparison with covalent surfaces

To verify our measurements on ionic crystals we also considered covalent substrates for comparison. In this case one expects very little or negligible effects of terraces on the surface potential. Ionic surfaces have some disadvantages, mainly their solubility in atmospheric conditions and the random direction of their terraces when cleaved. Sapphire was investigated because of its ability to reconstruct its surface into millimeter length atomic terraces after annealing. This would provide an ideal substrate as the terraces run for very long distances, are very well ordered and the substrate itself is insoluble in water. Figure 5.6 shows the topographic and accompanying Kelvin probe scan of a sapphire substrate.

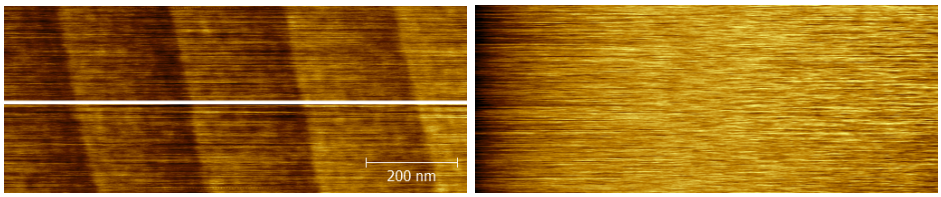

(a) (b)

Figure 5.6: Topographic (a) and SKPM (b) scan over the surface of sapphire. Although the sapphire surface reconstructed to form many large terraces, there was no detectable potential variation above the step edges in the SKPM scan. White line on topographic scan indicates where the topographic trace was extracted from for figure 5.7.

Although the surface creates very ordered terraces, they do not produce any measureable potential variation, meaning that they are unsuitable for this work. This is similar to work performed on SiC substrates[63]. Although SiC substrates are desirable because of their ease of creating graphene (through annealing), the terraces on SiC substrates also do not create sizable potential variations. Figure 5.7 shows the topographic trace taken from the sapphire topographic image 5.6, to show the uniformity of the steps.

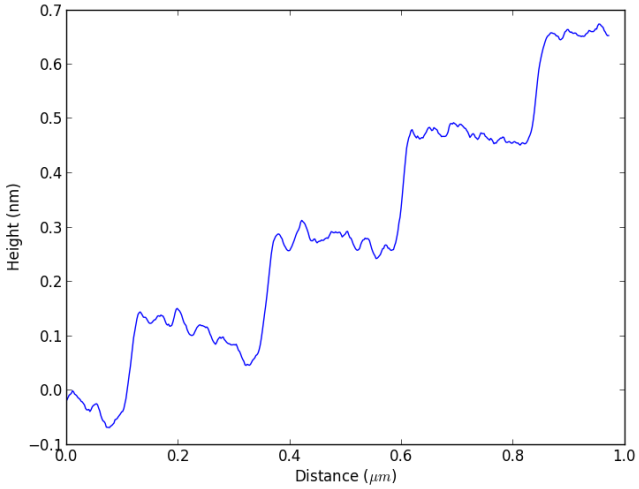

Figure 5.7: Topographic data of sapphire taken from the topographic image 5.6.

5.2 Screening induced by graphene

Mechanically exfoliated few-layer graphene (FLG) flakes were deposited on cleaved KBr(001) crystal surfaces and used to investigate the effects of terraces, steps and pits on the surface

potential of graphene, as well as its variation with number of graphene layers, through electrostatic force (EFM) and Kelvin probe (KP) microscopies. EFM measures the phase shift of a driven cantilever due to the electrostatic force between sample and a biased tip,[64]) while KP, the contact potential difference between tip and sample.[65]) EFM has been used recently to reveal the charge screening behavior of FLG deposited on disordered SiO_2 substrates, and good agreement with a nonlinear Thomas-Fermi theory for screening was found.[11]) EFM imaging has allowed identification of graphene domains for epitaxial graphene grown on SiC surfaces[66]) but being a technique that measures forces, edges and structured features can introduce undesired topographic cross-talk. Moreover, to measure the surface potential V_s, spectroscopic measurements relating phase shift to tip bias according to a parabolic law[64]) are required, and not just mere images at constant bias. In comparison, KP imaging directly maps V_s (through an additional controller that adjusts tip-sample bias until the electrostatic force is cancelled[65])) and topographic features such as nanostructures do not introduce sizeable contrast if there is no real change in their associated surface potential.[67])

Cleaving of KBr crystals, graphene deposition and subsequent imaging were performed in air, in conditions below 50% humidity to limit step edge evolution[57]) (discussed below). FLG flakes were identified using cross polarized light which enhances the contrast of graphene layers (not shown) in a similar manner as demonstrated for graphene on mica.[38]) Flakes thicker than three layers were easily detected, but distinguishing between mono-, bi-, or tri-layers was ambiguous.

5.2.1 EFM measurements

EFM phase images at constant bias (Figure 5.8(a)) were therefore acquired (in a two-pass sequence[68]) with an Asylum MFP-3D) to unambiguously detect and enhance contrast for FLG domains with less than four layers. Figure 5.8(a) shows that domains of similar thickness are readily distinguished among the quilt aspect of the flake, in contrast to the corresponding topographic image (Figure 1(c)). By magnifying the highlighted area one can see that even within domains of constant thickness that extend over several flat substrate terraces (crosses on Figure 5.8(d)) there are weak variations in colour that indicate a non-uniform surface potential and resulting doping profile (Figure 5.8(b)). Separate spectroscopic measurements (taken also on a different flake, Figure 5.9) showed that such surface potential variations can reach tens to hundreds of meV. This can be the result of the FLG being in van der Waals contact with the highest terraces, while being suspended over the lower ones leads to a lower potential as the distance to the substrate is a parameter of screening theories for graphene.[11] That graphene domains have different properties whether in contact with the substrate or, in contrast, suspended has also been

observed in graphene on SiC by friction mapping and current-voltage spectroscopy.[63]

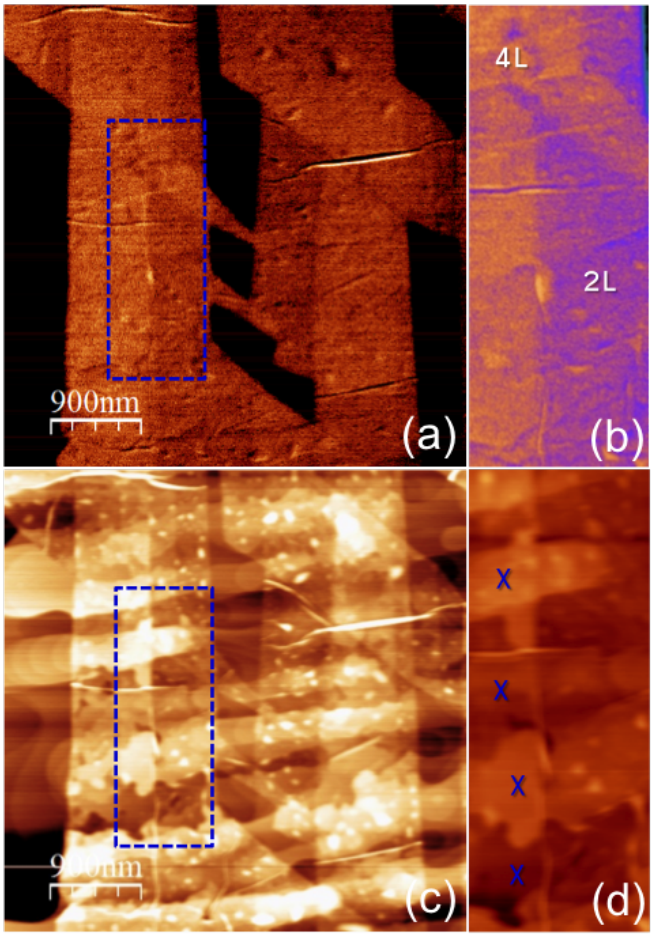

Figure 5.8: EFM (phase) (a),(b) and topographic maps (c),(d) of a FLG flake on a KBr terraced surface. -5V was applied to the tip in EFM, a value within the expected parabolic regime of the phase-bias dependence.[64],[68]. EFM clearly delineates domains of same thickness (colour): darkest domains are monolayer graphene. (d) Topography and (b) EFM of region framed in (c),(a) showing that graphene regions within a uniform thickness domain have different surface potentials if the underlying KBr terraces (crosses in (d)) have different heights.

5.2.2 Kelvin probe measurements

KP imaging (performed with an Asylum Cypher) was then used to directly measure changes in the surface potential induced by nanoscale features of the ionic surface, whose effects would be otherwise masked by topographic cross-talk in EFM[69]. Cleavage along the (001) KBr face was shown to reveal high index steps[70] and wavy steps[71] these can

only be obtained through a succession of polar kinks.[71],[45] Additionally, exposure to ambient conditions leads to rounding of the nonpolar edges, and an evolution dependent on the humidity level.[57] In our conditions of moderate humidity (<50%) there is preferential dissolution of the cations in the adsorbed water layer and their segregation in the step edge vicinity to create identical dipoles that decorate the steps[57] and would point towards an overlaying graphene sheet. All these phenomena specific to ionic surfaces are expected to yield substantial changes in the surface potential at step-edges, and figure 5.9(a) shows local variations ΔV_s of -100 to -120 meV above the step edges of the bare surface. Topographic effects were excluded by scanning in KP mode at various angles relative to the step edges, with identical results. Such step edges, along with nanoscale pits and protrusions (Figure 5.9(c)), affect the graphene domains (e.g., Figure 5.9(b) shows bi- and four-layer domains) by inducing sharp local variations of their surface potential. Figure 5.9(d) shows that each nanoscale feature of the substrate produces a clear localized potential modulation in the bi-layer, while their effect is strongly suppressed in the four-layer; e.g. following the step edges E1-E2-E3 which extend from the bare substrate underneath both the bi- and 4-layer graphene domains, ΔV_s changes from -140 meV (above E2, substrate), to -60 meV (above E3, bi-layer) and to -15 meV (above E1, four-layer). This is evidence of screening by FLG.

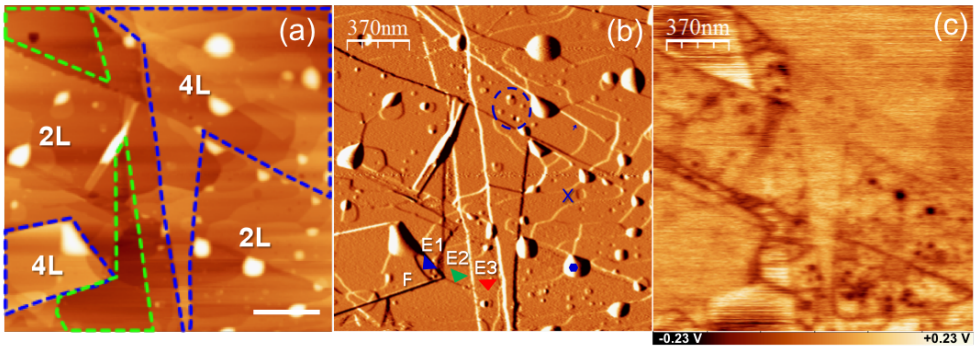

Figure 5.9: FLG flake on a KBr terraced surface investigated by KP microscopy. (a) Topography, with boundaries of FLG domains and substrate highlighted: green, KBr zones; blue, four-layer graphene; bi-layer graphene, between the two. Scale bar is 370nm. (b) Amplitude image of the FLG. Labeled representative features: step edges (triangle), pits (cross), protrusions (encircled), and organic contaminations (hexagon). (c) Surface potential image corresponding to (b). Graphene folding F did not produce additional potential variation.

Figure 5.10 contains collected data points (from Figure 5.9(c) and a further image) from steps, pits and protrusions of similar height and diameter, respectively, showing the potential being screened with increasing number of layers. Values group on two curves,

one for edges, the other for pits/protrusions. Pits/protrusions induce larger potential modulations than step edges due to their higher density of polar kinks (instrumental to their formation).

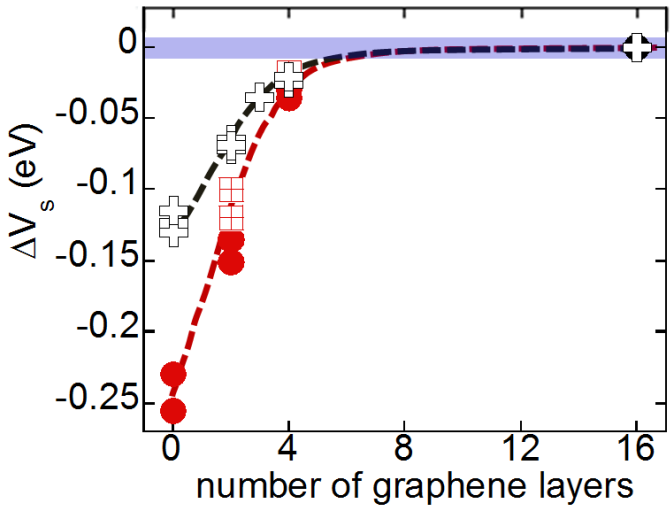

Figure 5.10: Surface potential ΔV_s originating from edges (crosses), and pits/protrusions (circles/squares) of approximately 40 nm diameter, as a function of number of graphene layers, measured with the tip 8 nm away from the surface. Band around 0 marks the noise level of the KP measurement.

Next the ΔV_s values from figure 5.10 are normalised to that of the same substrate, for both edges and pit/protrsions and presented in figure 5.11. It can be seen that the screening on both of these nano-scale features is approximately the same, although the surface potential is different between the two types of feature.

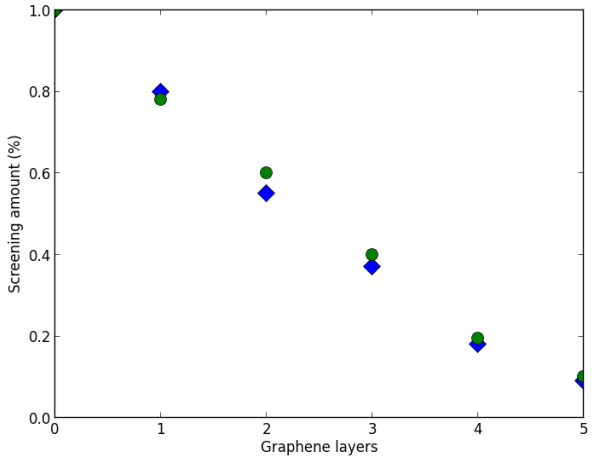

Figure 5.11: Normalised screening through graphene layers above edges (diamonds) and pits/protrusions (Circles).

The surface potential dependence on the number of layers is non-linear, reminiscent of that reported for FLGs deposited on large area, homogeneous SiO2 substrates,[11] however, the values recorded here are smaller. Here, the measured electrostatic potentials generated by nanostructures vary with tip-surface distance, unlike the measurement of the work function of flat surfaces. For the case of a line of dipoles the electrostatic potential decays as 1/z. Consequently, the values measured in Figure 5.10, where the tip was approximately 8 nm above the surface, are reduced due to this height dependency, and reflect on-sheet potentials that are tenths to 1 eV in magnitude when scaled back to the location of the graphene layer. This is evidence that the potential within the graphene in the vicinity of the nanostructures is sizeable, with concomitant effects to be expected on the local doping. Note that for graphene grown on SiC, a covalent substrate, KP measurements around step edges did not detect changes,[72] while theory estimates only negligible modifications (approximately 10 meV) in the graphene work function resulting from associated mechanical deformations.[73] A more precise estimation of the magnitude of these nanoscale electrostatic sources is complex but could be achieved by measuring ΔV_s(z) spectroscopic curves (as performed in section 5.3 and further relating them to atomic scale details of the nanostructures (through atomic resolution AFM techniques, as shown in section 2.3.1. One possibility then would be the study of local screening by graphene, which is known to be complex on account of the unusual and strongly thickness-dependent electronic structure, with the vanishing density of states at the Dirac point resulting in significant non-linear effects and major impact from doping and thermal effects. Screening in graphene is currently a matter of debate even in the case of large

equipotential flakes[10],[11] where a one-dimensional treatment is possible, whilst in our case the local electrostatic source means lateral variations are relevant[12] and need further atomic level investigations. Only then can a screening law be given. From the KP images the in-plane extent of the potential modulations within our FLG layers does not exceed that of the corresponding lateral topographic profiles, which are, however, dominated by tip convolution effects that give an experimental resolution of approximately 20nm. Our numerical calculations of the effects of an external dipole on monolayer graphene using Thomas-Fermi theory indicate a lateral potential variation extent of the order of 1nm for typical doping levels (see also ref. [12]). This established the spatial range expected for potential modulations induced by nanoscale features of ionic substrates, which may represent the ultimate resolution achievable for the electrostatic patterning of doped regions within graphene.

5.3 Decay of measured potential with tip-surface distance

The decay of measured potential with tip-surface distance will now be investigated. Here different regions with different numbers of layers of graphene regions are scanned at varying tip-sample distances in order to better understand the screening through graphene. The same process applies as to previous work. Graphene is deposited onto an ionic substrate then located and scanned using Kelvin probe microscopy. It is advantageous to obtain a graphene flake which has regions of different thickness deposited along the same terrace edge, as the magnitude along will be approximately constant in this case.

In the next sections three surface potential measurements were extended to incorporate $\Delta V_s(z)$ data, although the z range covers the large distances and does not include the sub-nm range (as obtained in non-contact AFM). Chapter 6 will include the screening through graphene layers, in an attempt to access the surface potential from the $\Delta V_s(z)$ data.

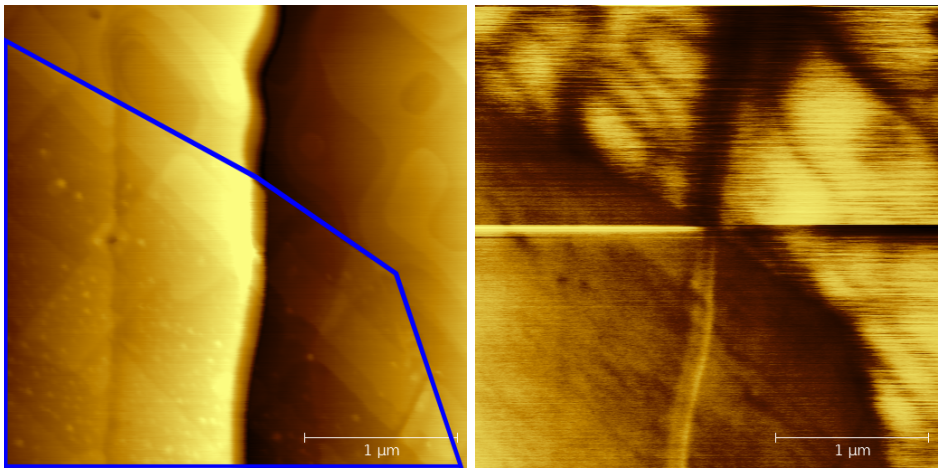

(a) (b)

Figure 5.12: Topographic (a) and SKPM (b) scans over a region of four layer graphene on a KBr surface. The region in the bottom right contains the graphene (marked by the blue outline), the rest of the image is that of the bare substrate. The graphene causes a strong suppression of the surface potential, which can be observed in the SKPM scan.

Figure 5.12 shows topography and SKPM images of four-layer graphene with transitions to the bare substrate covering many terraces, where the four layer graphene domain can be seen in the left side of both images (marked with a blue outline). Here it can be seen that the underlying potential is strongly suppressed in the four-layer domain. Terraces which were similar were used for measurement. The potential above step edges was then measured at differing tip-sample distances. From this two things can be extracted, firstly the potential decay above the substrate and graphene with tip-sample distance can be extracted, and secondly the amount of apparent screening with tip-sample distance can be extracted. 5.13

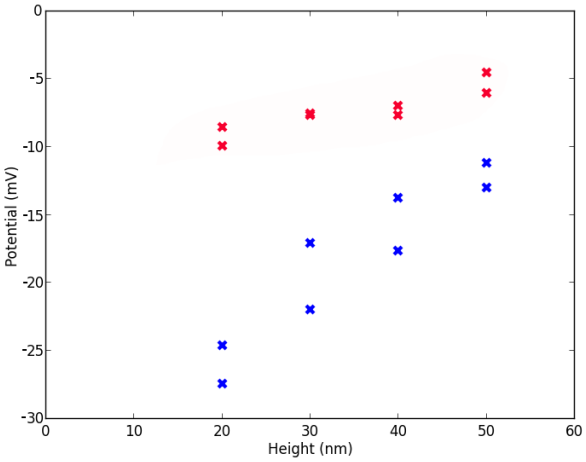

Figure 5.13: Potential measured above varying heights above the step edges, over the bare substrate (red) and above the graphene (blue).

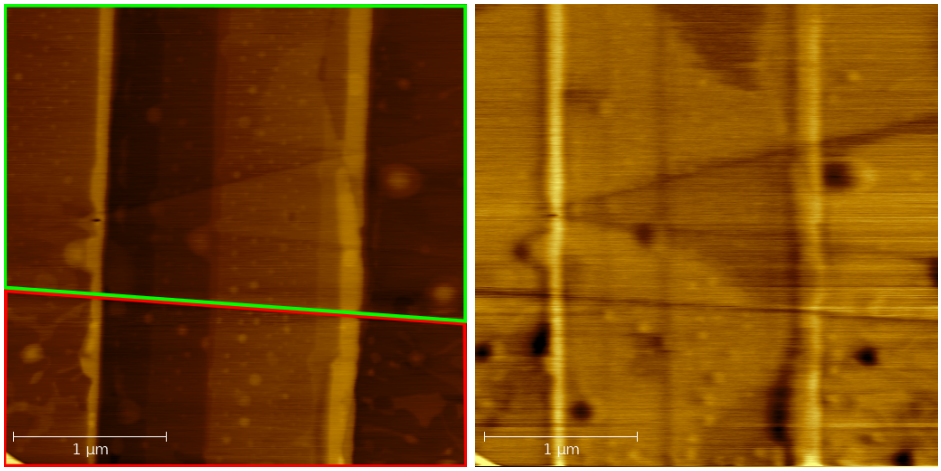

(a) (b)

Figure 5.14: Topographic (a) and SKPM (b) scans over a bi- and tri-layer graphene. Here the boundary between the bi- and tri-layer graphene can be seen as the almost horizontal line that spans both images (marked by the green outline). The bi-layer is contained in the bottom portion of the scan (marked by the red outline).

Figure 5.14 shows a topography image of domains of bi- and tri-layer graphene on an ionic substrate. These graphene domains cross many step edges, which can be seen in the figure as the vertical lines. The potential decay is then measured above step edges which extend underneath both graphene domains measured against tip-sample distance,

as shown in figure 5.15. Although there are no transitions between the graphene and the bare substrate, the bare surface potential measured at 8nm can be approximated from previous work that measures the screening amount between the bare substrate, bi-layer and tri-layer graphene.

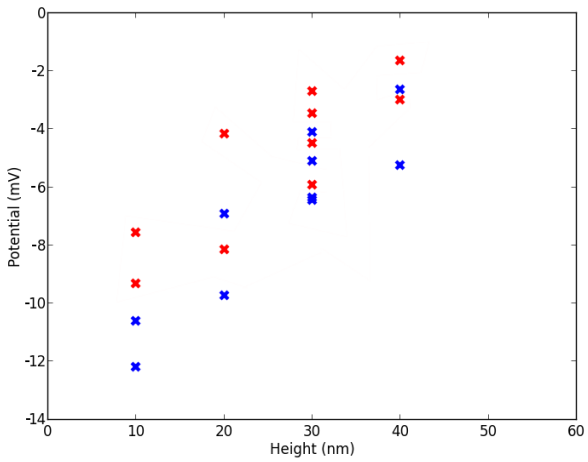

Figure 5.15: Potential decay taken above the step edges over the bi- and tri-layer graphene domains , shown as red and blue markers, respectively .

Although the potential decays above the surface of graphene, the amount of measured screening remains approximately the same for all domains. Now that the experimental results have been discussed, the next chapter will introduce a simulation that will replicate the experimental system in an attempt to reveal more information about them, such as the surface potential and the surface potential width generated by nanostructures in the ionic substrate and the potential screening through graphene, as well as graphene parameters (such as doping levels).

In general, ionic substrates might be exploited to produce atomically controlled superlattice effects within graphene sheets, with local doping provided by the local change in the surface potential associated with the step edges. Alternatively, nanostructures such as lines and rectangular pits can be created with atomic precision on surfaces of ionic crystals by electron beam irradiation in vacuum.[71],[45] These are known to produce strong local electrostatic fields, sufficient to guide the preferential self-assembly of polar molecules.[74],[75]

Chapter 6

Modelling of screening of localised potentials by graphene layers

A theoretical modelling of the screening of localized potentials - as are present in our experiments with nanostructured ionic surfaces - by graphene layers was implemented based on the Thomas- Fermi (TF) model. Analytical implementations of the TF model for graphene screening of single point charges or planar, uniform charge distributions exist for some specific cases (i.e. low doping levels of graphene, and few-layer graphene modeled as independent layers) [11][10][76]. Here we use a computational approach to implement TF for situations that do not have an analytical solution, such as lines of charges or dipoles, and in the most general way possible. This involves considering the full space of parameters for the chemical potential of graphene (resulting in various doping regimes) and magnitude of the source potential, as well as describing multi-layer graphene as systems with specific electronic structure (i.e. mono-, bi-, tri-layers etc.) and stacking order, as opposed to stacks of independent mono-layers. In conjunction with our sets of experimental potential- distance data, obtained above graphene layers of various thickness, it was possible to determine the unknown magnitude of the localized source potential, as well as the potential value on the surface of mono- or few-layer graphene, i.e. as felt by the graphene electrons. Hence, modelling shows that nanostructures in ionic surfaces are able to create sizeable localized potentials, of about 0.3-0.4 eV, in monolayer graphene, and describe the screening quantitatively.

6.1 Computational approach to Thomas-Fermi model for electrostatic screening

First theorised by Thomas and Fermi shortly after the introduction of the Schrödinger wave equation, the Thomas-Fermi model is a semi-classical model able to describe the electron density of a many body system by making a direct relation to the total potential of the system. In this way, the Thomas-Fermi model is able to describe the electrostatic screening through a material[77][12][78][79].

Normally the electron density is calculated using the construction of many one-electron wave functions. The Thomas-Fermi model bypasses this step using the assumption that the total potential within the system $\phi(\mathbf{r})$ is a very slow varying function of $\mathbf{r}$. This allows the model to be applied to very large systems, which would be otherwise impossible to calculate. However, it limits the calculation to a larger scale, with effects which take place over smaller distances (such as Friedel oscillations) being lost in this model.

The model uses several assumptions in order to find the relation between electron density and total potential. First the bulk system is considered as a uniform electron gas with total potential ϕ. This potential is considered to be uniform over a small scale, but can vary over a larger scale when modified by other potentials within the system. For a simple example of screening, a charge is placed within the system, this external potential is defined as ϕ^{ext}. The total potential now becomes $\phi = \phi^{ext} + \phi^{ind}$, where ϕ^{ind} is the potential induced by the external potential within the electron gas. Electrons tend to gather around a site of attractive external potential, therefore the model shifts the electrons within the system, thus inducing a charge density change within the system ρ^{ind}. The full charge density is now given by

$$\rho = \rho^{ext}(\mathbf{r}) + \rho^{ind}(\mathbf{r}) \tag{6.1}$$

where ρ^{ext} is the density of the external charge. The density ρ is related to the total potential by the Poisson equation, given by

$$\nabla^2\phi(\mathbf{r}) = -4\pi\rho(\mathbf{r}) \tag{6.2}$$

where ∇ is the Laplace operator, or explicitly

$$\left(\frac{\partial^2}{\partial x^2} + \frac{\partial^2}{\partial y^2} + \frac{\partial^2}{\partial z^2}\right)\phi(\mathbf{r}) = -4\pi\rho(\mathbf{r}) \tag{6.3}$$

in Cartesian coordinates for three dimensions. The total density induced, ρ^{ind} is given by the internal electron density n_0 considered as a function of the chemical potential μ modified by the potential $\phi(\mathbf{r})$, with the uniform background compensating density

subtracted from it;

$$\rho^{ind} = -e\left[n_0(\mu + e\phi(\mathbf{r})) - n_0(\mu)\right] \tag{6.4}$$

In some cases, this equation can be expanded and the Poisson equation linearized, enabling an analytical solution to the Thomas-Fermi model. Due to the complex nature of the geometries discussed in this thesis, an analytical solution of the Thomas-Fermi model is not generally available, therefore an iterative method was used to reveal extra information about the potential decay.

This uses a relaxation method, which consists of a matrix to represent three dimensional space. A potential can then be applied to the grid, to simulate the external potential acting on the system ϕ^{ext} which is then coupled with the induced potential ϕ^{ind}. The model then calculates an induced density from the combined potential ρ^{ind} using Poisson's equation, this in turn is used to calculate a new induced potential. This process is repeated until the calculated internal potential is the same as the previous iteration and thus the relaxation process is completed[79][78].

To begin with, simple geometries have been considered, to test for consistencies between the simulation and expected physics, for exapmple they can be compared with analytical solutions. The relaxation method used in the numerical work is that of successive over relaxation (SoR)[80], which allows for quick convergence times, while maintaining simplicity. This relaxation method will now be discussed in greater detail. Before the iterative process starts, boundary and initial starting conditions are set. An array is generated to represent the system and external potentials are applied to the system.

The SoR process works by linearising Poisson's equation, by considering that the grid points are close enough together that the change between each point is linear. In this way, the complex problem is broken down into many easy to calculate problems. Seven points are taken on the three dimension grid, one centre point and its surrounding neighbours, shown in figure 6.1.

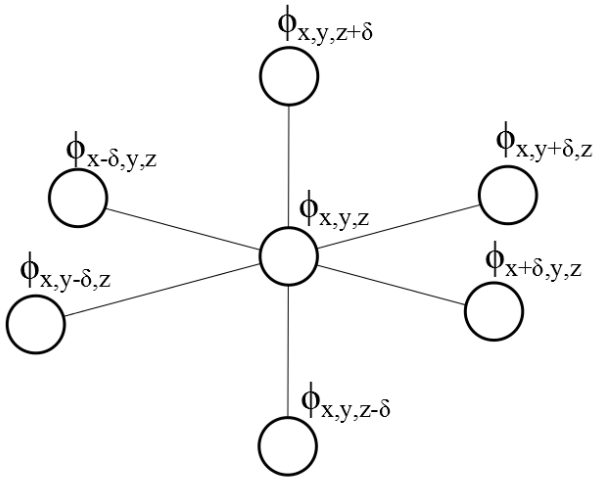

Figure 6.1: The seven point star shows the neighbours surrounding the centre point, which are used to calculate the new potential at the centre point using the SoR process.

The model is based on the discretisation approximation, where second order differentials are approximated by linear combinations of point values that describe the function, as shown by the following equation

$$\frac{\partial^2 \phi}{\partial x^2} = \frac{\phi_{x+\delta} 2\psi_x + \phi_{x-\delta}}{2\delta} \tag{6.5}$$

Here the spatial steps are uniform in x, y and z. Each point is assigned a scaling value, related to the step size between it and the centre value. Here a to f are related to the step size neighbouring points and g is the centre point.

$$a = b = c = d = e = f = \delta, g = -6\delta \tag{6.6}$$

for three dimensions, and hence the centre point ($g_{x,y,z}\phi_{x,y,z}$) has neighbouring points,

$$\begin{aligned} &a_{x,y,z}\phi_{x-\delta,y,z} \\ &b_{x,y,z}\phi_{x+\delta,y,z} \\ &c_{x,y,z}\phi_{x,y-\delta,z} \\ &d_{x,y,z}\phi_{x,y+\delta,z} \\ &e_{x,y,z}\phi_{x,y,z-\delta} \\ &f_{x,y,z}\phi_{x,y,z+\delta} \end{aligned} \tag{6.7}$$

The charge density relating to this will be defined as $h_{x,y,z}$ which is proportional to the source term. The relation between all these elements is given by,

$$\begin{aligned} h_{x,y,z} = a_{x,y,z}\phi_{x-\delta,y,z} + b_{x,y,z}\phi_{x+\delta,y,z} \\ + c_{x,y,z}\phi_{x,y-\delta,z} + d_{x,y,z}\phi_{x,y+\delta,z} \\ + e_{x,y,z}\phi_{x,y,z-\delta} + f_{x,y,z}\phi_{x,y,z+\delta} \\ + g_{x,y,z}\phi_{x,y,z} \end{aligned} \tag{6.8}$$

The iterative procedure is defined as solving the previous equation for $\phi_{x,y,z}$.

$$\begin{aligned} \phi^*_{x,y,z} = \frac{1}{g_{x,y,z}}(h_{x,y,z} - a_{x,y,z}\phi_{x-\delta,y,z} - b_{x,y,z}\phi_{x+\delta,y,z} \\ - c_{x,y,z}\phi_{x,y-\delta,z} - d_{x,y,z}\phi_{x,y+\delta,z} \\ - e_{x,y,z}\phi_{x,y,z-\delta} - f_{x,y,z}\phi_{x,y,z+\delta}) \end{aligned} \tag{6.9}$$

Then ta weighted average can by constructed as,

$$\phi^{new}_{x,y,z} = \omega\phi^*_{x,y,z} + (1-\omega)\phi^{old}_{x,y,z} \tag{6.10}$$

The residual at any stage is

$$\begin{aligned} \xi_{x,y,z} = a_{x,y,z}\phi_{x-\delta,y,z} + b_{x,y,z}\phi_{x+\delta,y,z} \\ + c_{x,y,z}\phi_{x,y-\delta,z} + d_{x,y,z}\phi_{x,y+\delta,z} \\ + e_{x,y,z}\phi_{x,y,z-\delta} + f_{x,y,z}\phi_{x,y,z+\delta} \\ + g_{x,y,z}\phi_{x,y,z} - h_{x,y,z} \end{aligned} \tag{6.11}$$

The final SoR algorithm is then equation 6.10 or

$$u^{new}_{x,y,z} = \phi^{old}_{x,y,z} - \omega\frac{\xi_{x,y,z}}{g_{x,y,z}} \tag{6.12}$$

The residual is used to decide when the system is sufficiently relaxed, and hench when to terminate the program. The final variable ω above, is the relaxation constant. This variable controls how fast the system relaxes and varies between zero and two. This variable works by altering how much of the corrected solution $\phi^*_{x,y,z}$ is used with the old solution $\phi^{old}_{x,y,z}$. A relaxation constant of zero would mean that the corrected solution is

ignored and the new solution is equal to the old solution and thus the system will never change from its starting conditions. For values between zero and one, the method of relaxation is called under relaxation, as the system underestimates the new solution and hence is slow to converge. Using a relaxation constant of one is neither over relaxation or under relaxation, it takes the old value of u and corrects it with the corrected solution, this method of relaxation is guaranteed to produce a converged array. The method used in this thesis is over relaxation, with ω set between one and two, meaning that the system makes an over correction to the old value. This method allows for greatest convergence speed, however if not set correctly, the over relaxed method can cause the system to become unstable and deviate from a solutionl therefore selecting a correct relaxation constant is essential, not only for speed of the simulation but also to maintain a converging model.

There are several other standard methods used to increase the convergence speed of a SoR algorithm (such as Chebyshev acceleration [80]) which are used in this model, however will not be discussed as they do not give any greater insight into the workings of the SoR algorithm.

6.2 Testing potential decay in vacuum from various charge distributions

6.2.1 Point charge

To test the consistency of the simulation, first a point charge is considered. As the decay from a point charge in 3D space is well known, it is the perfect initial test for the simulation, and is given by the following equation.

$$\frac{-Q}{4\pi\epsilon_0 r} \tag{6.13}$$

To replicate this in the simulation, a 3D grid is defined with the centre cell acting as a point charge which is scaled accordingly with the grid step size. The remaining grid is considered a vacuum. From running this simulation, figure 6.2 is taken from a cross section through the centre of the grid, showing the point charge in the centre and the potential decay around it.

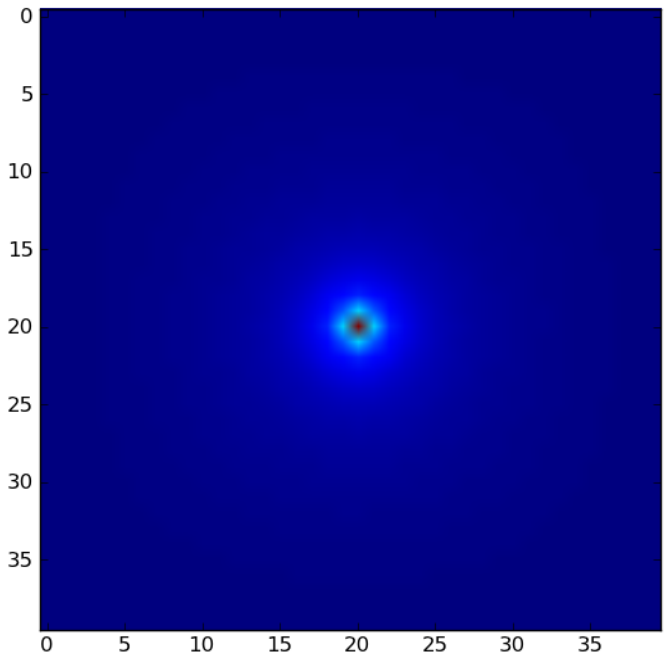

Figure 6.2: Cross section of a simulation of the potential decay around a point charge.

Figure 6.3 shows a line profile taken through the point charge for multiple simulations using differing step sizes, with a theoretical decay in cyan. This shows that the simulation produces a final result which resembles that of the given equation 6.13. The differing step sizes are used to show that the simulation is invariant under spatial scaling. The only deviation from the theoretical fit is of that near the boundaries of the simulation. The boundary conditions are set to zero for this simulation, which leads to a slight deviation at distances close to that of the total size of the simulation grid and at the centre, where the grid does not have enough resolution to calculate the potential

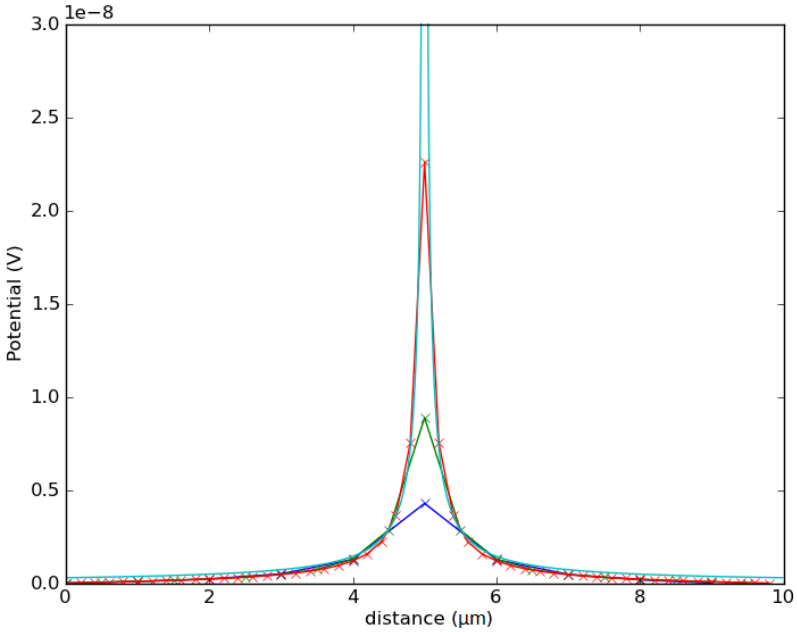

Figure 6.3: Line profile across the simulated point charge showing the potential decay for multiple grid step sizes, theoretical decay shown in cyan.

6.2.2 Line of charge

Delta function

The potential decay from a line of charge will now be calculated and then used to test the physics of the simulation. First several approximations will be used to calculate the decay from different geometries of charged geometries in a vacuum. The potential decay can be calculated using Poissons equation, and as this system is considered to be in vacuum, there is an absence of charges and therefore Poissons equation is equal to zero and becomes Laplaces equation.

$$-\nabla^2 V = 0 \tag{6.14}$$

All of the geometries considered here will be charged strips of infinite length in the y axis, in an attempt to replicate the charge from a step edge of a substrate. The first geometry that will be considered is the simplest implementation, a delta function. The strip is infinitely thin in the x axis and infinitely long in the y axis and is positioned at zero on the z axis with zero thickness, with the x position of the delta function being x_0,

as shown in figure 6.4.

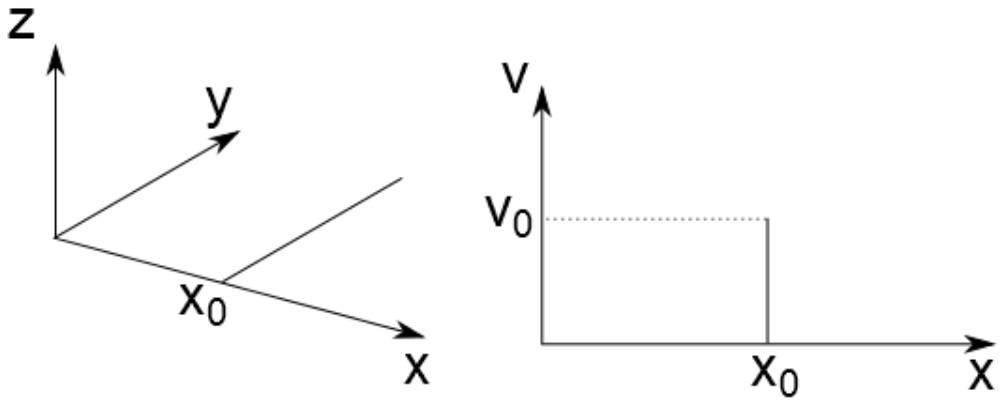

Figure 6.4: Diagram of the delta function, centred about the x_0 point and infinite in the y axis.

Here x_0 is taken as zero for simplicity, the form of the delta function is given by the following equation.

$$V(x,0) = V_0\delta(x) \tag{6.15}$$

As the distribution is infinite in the y axis, Laplaces equation becomes

$$\frac{d^2V}{dx^2} + \frac{d^2V}{dz^2} = 0 \tag{6.16}$$

Therefore, only the x and z axis are required. Next a Fourier transform of the delta function is taken in the x axis.

$$\hat{V}(k_x,z) = A_{k_x}e^{k_xZ} + B_{k_x}e^{-k_xz} \tag{6.17}$$

where $k_x \geqslant 0$. As the potential must approach zero for a potential decay as z approaches infinity, the constant A must be zero and therefore

$$\hat{V}(k_x,z) = B_{k_x}e^{-|k_x|z} \tag{6.18}$$

$$V(x,z) = B_{k_x}e^{-|k_x|Z}\int_{-\infty}^{\infty} dk_x B_{k_x}e^{-|k_x|z}e^{ik_xx} \tag{6.19}$$

The potential at the surface is already known and from this the constant B can be found.

$$V(x,0) = V_0\delta(x) = \int dk_x B_{k_x} e^{ik_x x} \tag{6.20}$$

Using Fourier analysis

$$B_{k_x} = \frac{1}{2\pi}\int dx V(x,0) e^{-ik_x x} \tag{6.21}$$

and therefore,

$$B_{k_x} = \frac{1}{2\pi} \tag{6.22}$$

Now that both constants are known, the potential decay in the z axis can be found. The potential for z is now given by.

$$V(x,z) = \frac{V_0}{2\pi}\int dk_x e^{-|k_x|z} e^{ik_x x} \tag{6.23}$$

As the width of a delta function is zero, this becomes,

$$\begin{aligned} V(0,z) &= \tfrac{V_0}{2\pi}\textstyle\int dk_x e^{-|k_x|z} \\ &= \tfrac{V_0}{\pi}\textstyle\int_0^\infty e^{-k_x z} dk_x \\ &= \tfrac{V_0}{\pi}\ \tfrac{e^{-k_x z}}{-z}\Big|_0^\infty \\ &= \tfrac{V_0}{\pi z} \end{aligned} \tag{6.24}$$

Figure 6.5 shows the potential decay from a potential of V_0 using a delta function

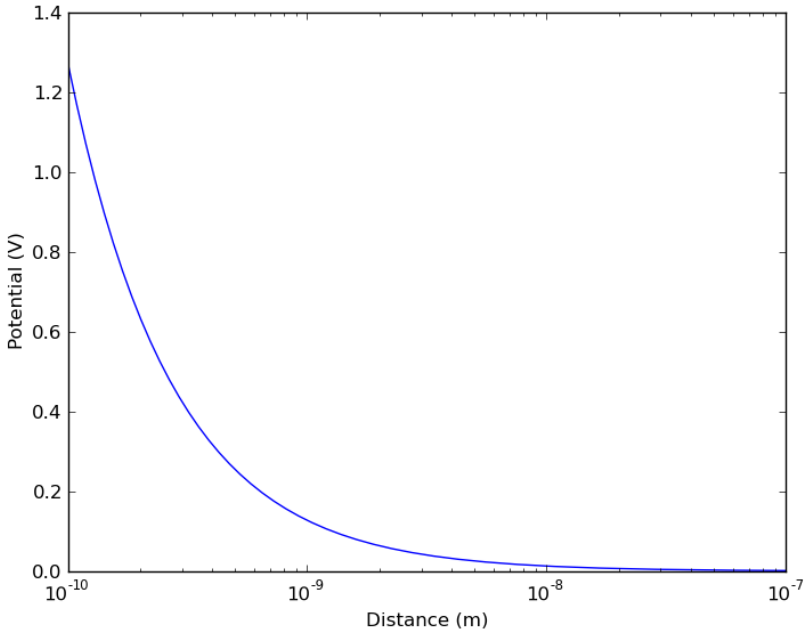

Figure 6.5: Potential decay of the delta function with distance.

From this it is obvious that for a 1D potential in a 3D system, the potential decay directly above the charge is only dependant on the surface charge and the height from the surface.

Top-Hat function

Now a more realistic geometry will be considered, here a top-hat function is used instead of a delta function. The rest of the geometry remains the same, where the function is in the x axis, infinite in the y axis and positioned at zero on the z axis and at x_0 on the x axis, as shown in figure 6.6.

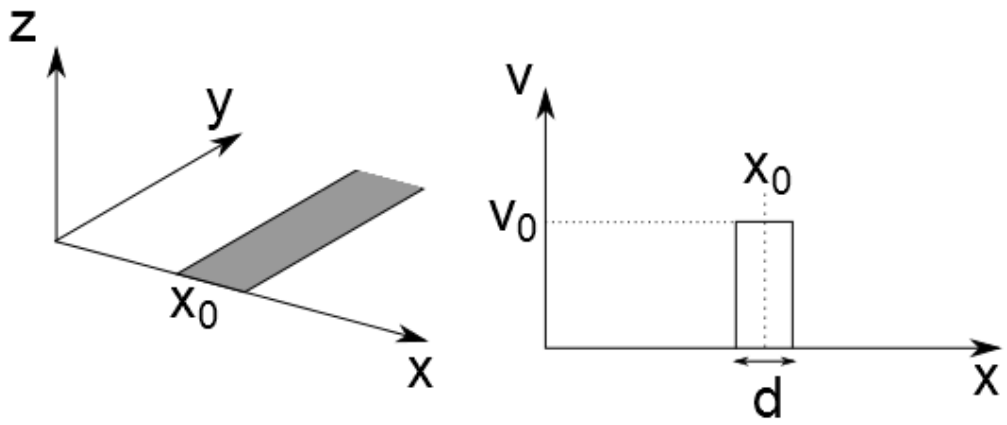

Figure 6.6: Diagram of the top-hat function, centred about the x_0 point and infinite in the y axis.

This is created using two Heaviside step functions, as shown by the following,

$$V(x,y,0) = V_0\left[\theta\left(x_0 + \frac{d}{2} - x\right) - \theta\left(x_0 - \frac{d}{2} - x\right)\right] \tag{6.25}$$

where x_0 is the center of the step. The same starting approximations are made as with the delta function, where the constant A is zero, therefore B can be calculated by using the equation 6.19 and setting z to zero and the known starting condition where z is zero.

$$V(x,0) \quad = V_0\left[\theta\left(x_0 + \tfrac{d}{2} - x\right) - \rho\left(x_0 - \tfrac{d}{2} - x\right)\right] \quad = \int dk_x B_{k_x} e^{ik_x x} \tag{6.26}$$

Using Fourier analysis

$$\begin{aligned} B_{k_x} \quad &= \tfrac{1}{2\pi}\int dx V(x,0) e^{-ik_x x} \\ &= \tfrac{V_0}{2\pi}\int_{z_0-d/2}^{x_0+d/2} e^{-ik_x x} dx \\ &= \tfrac{V_0}{2\pi}\ \tfrac{e^{-ik_x x}}{-ik_x}\Big|_{x_0-d/2}^{x_0+d/2} \\ &= \tfrac{V_0 d e^{-k_x x_0}}{2\pi} sinc(k_x d/2) \end{aligned} \tag{6.27}$$

$$V(x_0,z) = \frac{2V_0}{\pi} arctan\left(\frac{d}{2z}\right) \tag{6.28}$$

Now using a Taylor expansion the potential decay becomes

$$\begin{aligned} V(x_0, z) &\approx V_0 \left(1 - \tfrac{4}{\pi}\tfrac{z}{d} + \tfrac{16}{3\pi}\left(\tfrac{z}{d}\right)^3 + \ldots\right) \\ &\approx V_0 \left(\tfrac{1}{\pi}\left(\tfrac{d}{z} - \tfrac{1}{12}\left(\tfrac{d}{z}\right)^3 + \tfrac{1}{80}\left(\tfrac{d}{z}\right)^5 + \ldots\right)\right) \end{aligned} \tag{6.29}$$

Here it can be seen that the dominating term of the decay is given by the first term of the Taylor expansion and given by

$$V(x_0, z) \approx \frac{V_0 d}{\pi z} \tag{6.30}$$

Using this dominating term, it is obvious that the surface potential V_0 cannot be determined from the potential decay alone, it also requires information about the width of the potential at the surface before the surface potential V_0 can be calculated. Therefore it is not possible to determine the surface potential from scaling back the potential from measurements taken above the surface, without taking into account the lateral size of the potential at the surface. Figure 6.7 shows the simulated decay from a top-hat function against the analytical decay. This figure shows a good agreement between analytical and simulated decay, there is however a slight deviation between results at distances away from the surface, this is due to the boundary conditions set in the simulation.

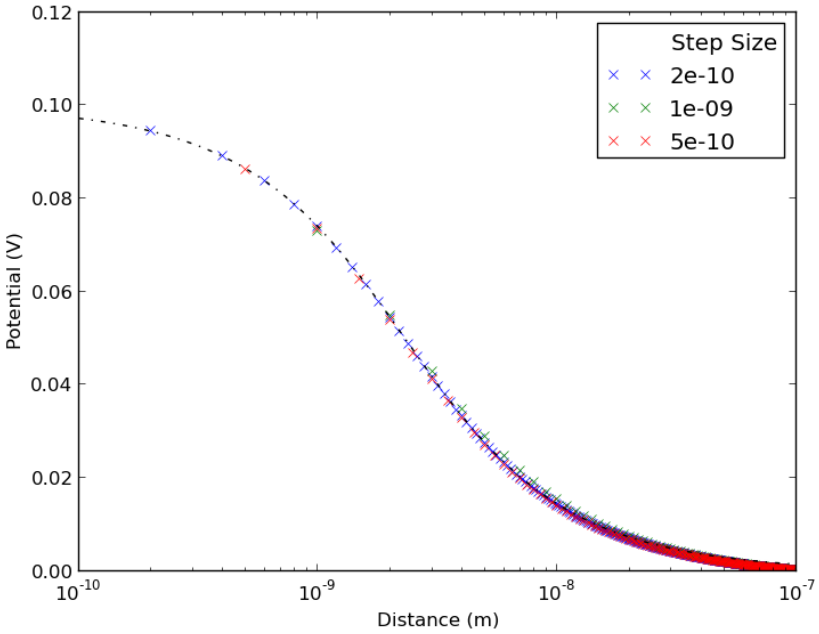

Figure 6.7: Simulation of decay from a surface potential modelled as a top-hat function. The dashed black line indicates an analytical solution where as the crosses represent simulated values. Colours indicate different step sizes used in the simulation.

Gaussian step decay

For a slightly more realistic potential, consider a strip of potential, infinite in the y axis and a Gaussian distribution in the x axis, set at zero position on the a and z axis, shown in figure 6.8

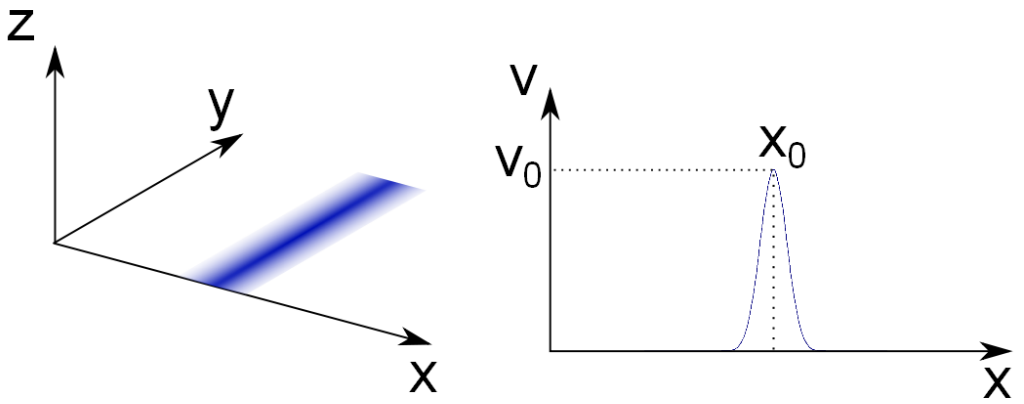

Figure 6.8: Diagram of the Gaussian function, centred about the x_0 point and infinite in the y axis.

$$V(x,0) = V_0 e^{-x^2/2\sigma^2} \tag{6.31}$$

x_0 is again set to zero for simplicity. Here the value of the constant B is given by,

$$\begin{aligned} B_{k_x} &= \tfrac{1}{2\pi} \int dx v_0 e^{-x^2/2\sigma^2} e^{-ik_x x} \\ &= \tfrac{v_0}{2\pi} \sqrt{2\pi\sigma^2} e^{-k_x^2\sigma^2/2} \end{aligned} \tag{6.32}$$

Therefore the potential becomes,

$$\begin{aligned} V(x,z) &= \tfrac{V_0\sigma}{\sqrt{2\pi}} \int_{-\infty}^{\infty} dk_x e^{-kx^2\sigma^2/2} e^{-|k_x|z} e^{ik_x x} \\ &= V_0 e^{z^2/2\sigma^2} efc(z/\sqrt{2r^2}) \end{aligned} \tag{6.33}$$

With the Taylor expansion

$$V(0,z) \approx V_0 \left[\frac{\sqrt{2}}{\pi} \left(\frac{\sigma}{z} - \left(\frac{\sigma}{z}\right)^3 3 \left(\frac{\sigma}{z}\right)^5 + \dots \right) \right] \tag{6.34}$$

Which has the dominating term

$$V(0,z) = \frac{V_0 \sqrt{(2)}\sigma}{\pi z} \tag{6.35}$$

Here again the dominating term is a function of the height from the surface and of the width σ of the potential in x. Therefore the potential cannot be separated from the width of the potential and therefore knowledge of the lateral extent of the potential at the surface is required to calculate the magnitude of the potential at the surface. Figure 6.9 shows the simulated Gaussian potential decay against the analytical decay. There is a good agreement between the simulation and analytical solution, however there is some slight deviation, again due to the simulation boundary conditions and resolution.

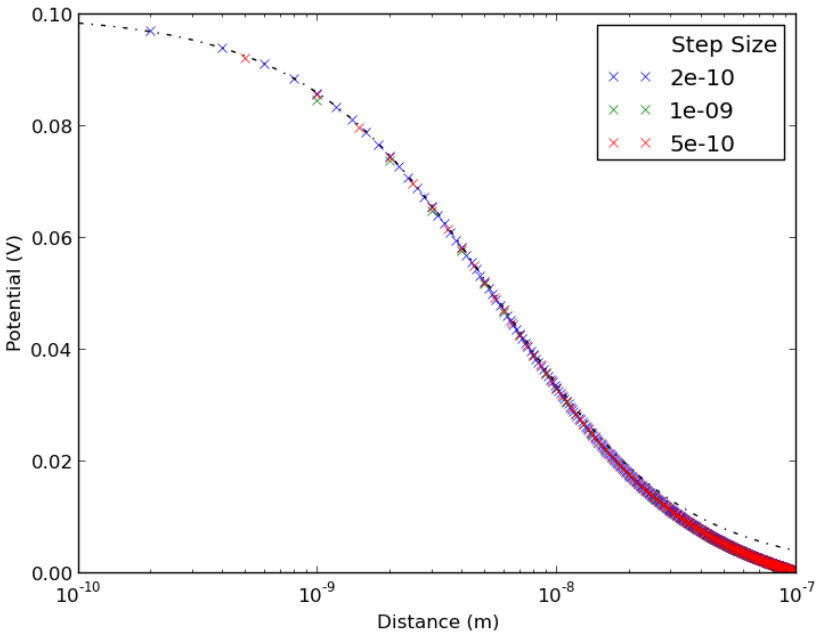

Figure 6.9: Simulation of decay from a surface potential modelled as a Gaussian function. The dashed black line indicates an analytical solution where as the crosses represent simulated values. Colours indicate different step sizes used in the simulation.

6.3 Screening of a planar, uniform potential distribution by graphene layers

6.3.1 Our model

Now that the simulation has been shown to be self-consistent and accurately follow the analytical solutions for several systems, the simulation will now include graphene as an overlayer[81]. First a one dimensional simulation will be performed, to simulate the decay of potential from an infinite surface with a uniform potential in plane. The axis across the surface is wrapped, the new form is given by

$$U_{x-1,y,z} = U_{x+1,y,z} = U_{x,y,z} \tag{6.36}$$

and

$$U_{x,y-1,z} = U_{x,y+1,z} = U_{x,y,z} \tag{6.37}$$

with these variables corresponding to figure 6.1. In this way, the simulation is able to create a pseudo-infinite surface and hence potential variation will only occur along the z axis. Graphene can easily be introduced to this simulation by creating regions within the simulation grid where the density no longer equals zero (as with a vacuum) but related to the density of states of graphene. This region is equal to the thickness of a graphene layer, as shown by figure 6.10

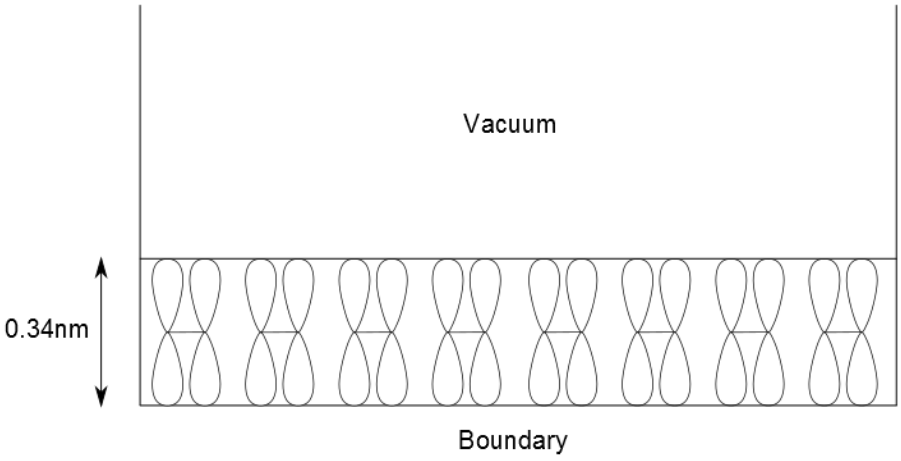

Figure 6.10: Cross section of a simulation grid for graphene. The external potential is applied along the boundary, then the simulation calculates the decay through the graphene and the vacuum. A thickness of 0.34nm is assigned as graphene as this is the van der Waals diameter of a carbon atom.

Here the external potential is applied along the boundary of the simulation grid and the potential decays through the graphene then the vacuum. A region of 0.34nm for graphene is used as this is the van der Waals diameter of a carbon atom. For a first approximation graphene is thought of as having no doping and therefore the equation 6.4 becomes

$$\rho^{ind} = -e\left[n_0(e\phi(r))\right] \tag{6.38}$$

Here it can be seen that the potential within the system directly affects the calculation of the density of states, and therefore affects the amount of screening of potential. As with before, the simulation is an iterative process and is repeated until the system becomes stable (Change in calculated induced density between iterations approaches zero). Figure 6.11 shows the effects of varying surface potential of the substrate on graphene, here a single layer of graphene is used in the simulation. The graphs are normalised to one, so that the different screening behaviours may be compared. The dashed line shows the surface of graphene, left of the dashed line shows potential decay within graphene whereas right of the line shows the decay outside of graphene.

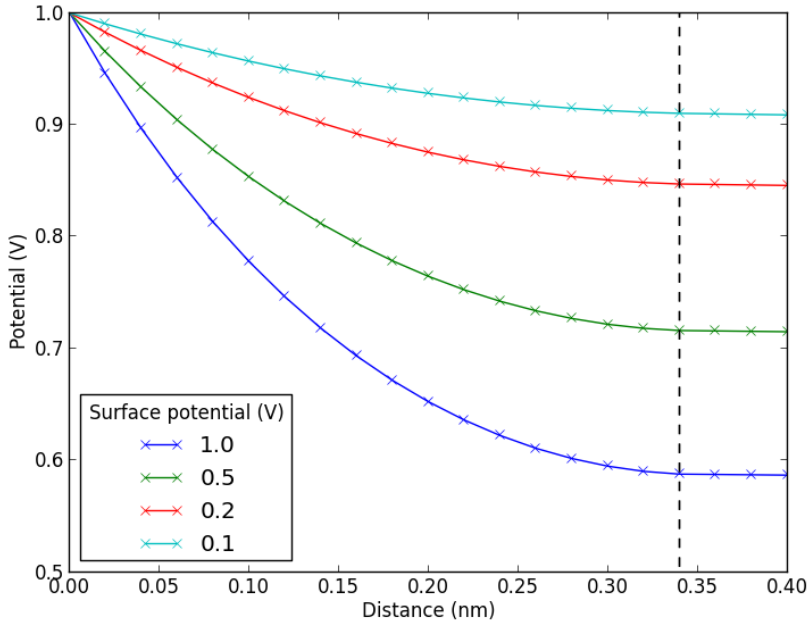

Figure 6.11: Potential decay through an infinite sheet of mono-layer graphene for differing substrate surface potentials, The surface potentials have been normalised to one so that a comparison can be made between potential decays.

Figure 6.12, shows the amount of screening occurring through a monolayer of graphene against the bias that is screened. As shown in the figure, the screening is highly dependent on the bias being screened. Here low values are slightly unrealistic as doping from non-uniformity in the graphene will most likely be larger than the bias being screened. This increase in screening with increased surface bias holds true until the energy rises above the linear region of the graphene band structure.

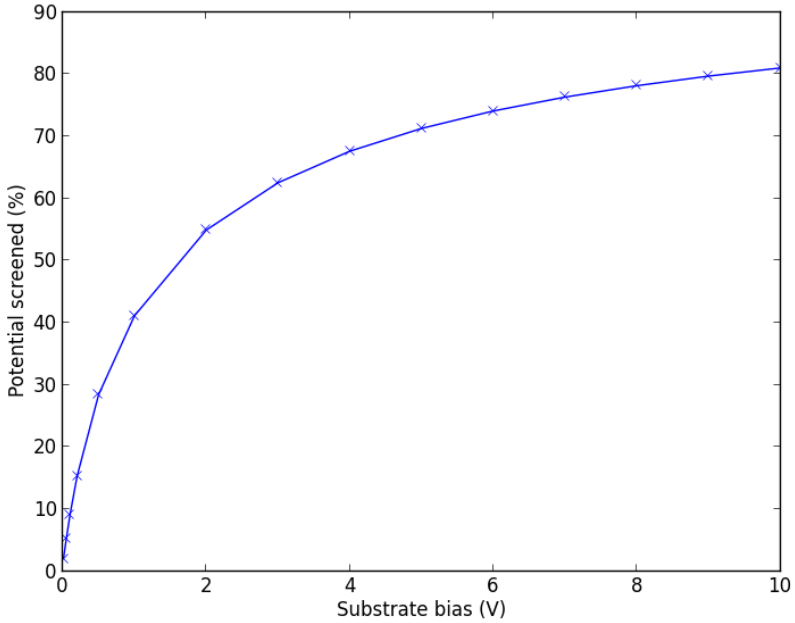

Figure 6.12: The percentage screening at the surface of graphene of the substrate surface plotted against the substrate surface bias.

Next doping the graphene will be considered, here the parameter μ is used for the doping level as shown in equation 6.4. The effect of μ is that it will induce a higher or lower density of carriers within the graphene depending on the polarity of the doping and the polarity of the potential being screened. Figure 6.13 shows the effects of a screening within graphene when the graphene is doped. Here the substrate surface potential is kept constant. As with before, the dashed line represents the surface of the graphene. Notice that the polarity of μ creates either an increased or decreased screening with respect to zero μ.

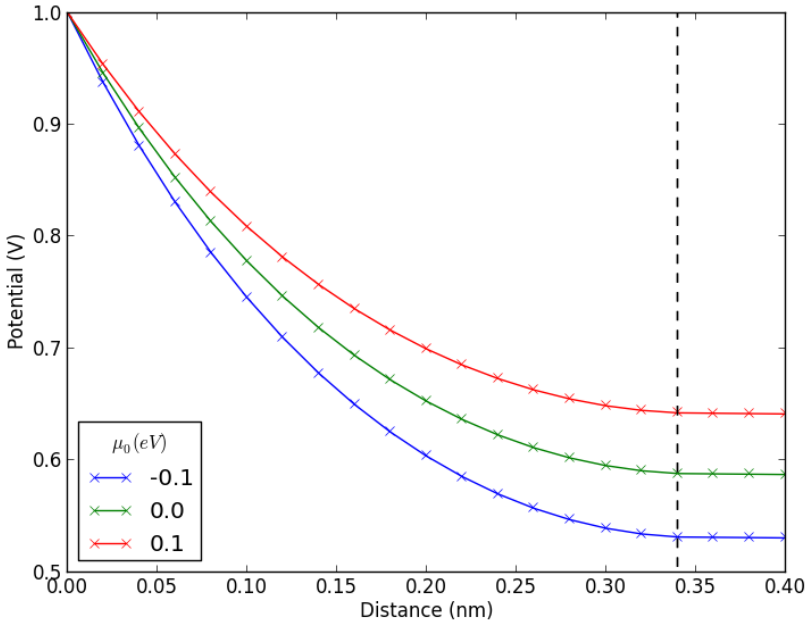

Figure 6.13: The effect of dopants on the screening behaviour of graphene.

Next the stacking of graphene will be considered. This is an important step as many systems consist of multiple layers of graphene. Here the difference between two monolayers of graphene stacked directly on top of each other and bi-layer graphene will be considered. Bi-layer graphene contains four bands in its structure, the first set meet at the zero energy point, the second exist above and below the energy $\pm$ t$'$, as shown in figure 1.8. To begin with, the situation where the energy is above that of t' will be considered. Here the total number of occupied states as determined by the chemical potential in bi-layer graphene is,

$$n_{0bi} = \frac{2E^2}{(\hbar V_f)^2 \pi} \tag{6.39}$$

and the total number of occupied states as determined by the chemical potential below t' in bi-layer graphene is given by,

$$n_{0bi} = \frac{E(E+t')}{(\hbar V_f)^2 \pi} \tag{6.40}$$

where thickness is the thickness of an individual graphene layer which corrects for the thickness the equation is spread over. Here as the equation corresponds to a bi-

layer, the thickness of mono-layer graphene is multiplied by a factor of two. The total number of occupied states above t' resembles that of the mono-layer band structure and the second set of bands in bi-layer graphene means that there are double the number of electrons when comparing it to mono-layer graphene. However, as this is spread over double the distance of mono-layer graphene the equations are equal and therefore the screening between bi-layer graphene and a mono-layer graphene stack of two layers will be equal, as shown by the following for mono-layer,

$$n_{0mono} = \frac{E^2}{(\hbar V_f)^2 \pi}. \tag{6.41}$$

This is easier explained by looking at the number of states in the system against energy (Shown in figure 6.14). Here the total number of occupied states for a bilayer (function of energy) is shown against the number of occupied states of a double stack of mono-layer graphene. Notice that the bilayer graphene has states even at zero energy, however the gradient of the bilayer is less than the mono-layer stack below t′ above which the number of states match exactly.

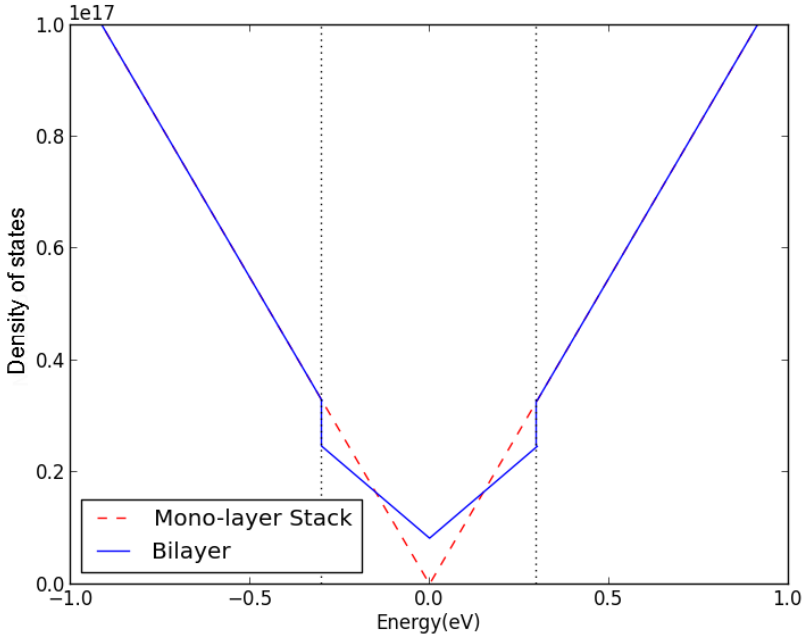

Figure 6.14: Density of states of AB stacked bi-layer graphene against that of mono-layer graphene.

The resulting decay for mono-layer and bi-layer graphene with energies above the t′

value is shown in figure 6.15.

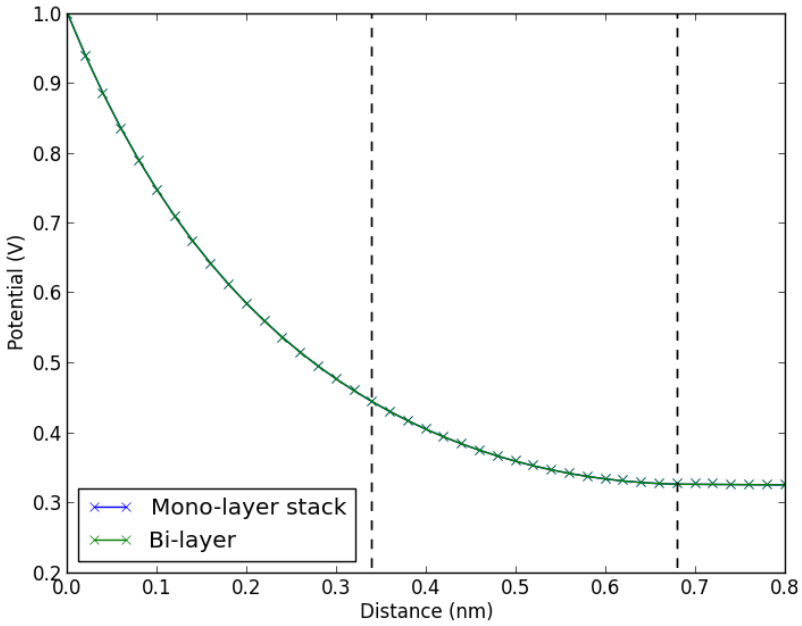

Figure 6.15: The screening through bi-layer graphene and a double mono-layer stack of graphene above t′, as expected the two simulations match exactly.

Note that here the dashed line shows the surface of the graphene layers, the first showing the first layer and the second at 0.68nm showing the surface of the second layer. As expected both the mono-layer stack and the bilayer graphene simulations match exactly. Next, we consider the situation where the energy is below t′ is explored. Here the situation is different, the equations for a mono-layer stack and bilayer graphene do not match and therefore a difference in screening will be introduced. Figure 6.16 shows the results of this simulation.

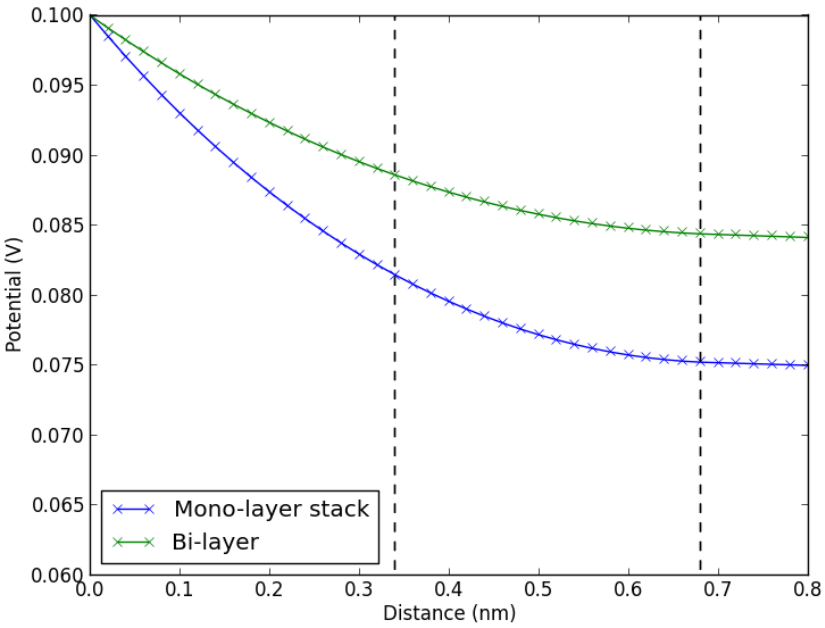

Figure 6.16: The screening through bi-layer graphene and a double mono-layer stack of graphene below t′, here there is a difference of approximately 10%.

The results of this clearly show a difference in screening of approximately ten percent. This value of screening however will also change depending on the variables in the system (i.e. Substrate surface potential and doping level). Altering these variables and measuring the percentage difference in screening between the simulated bi-layer graphene and the mono-layer stack results in the following surface plot,

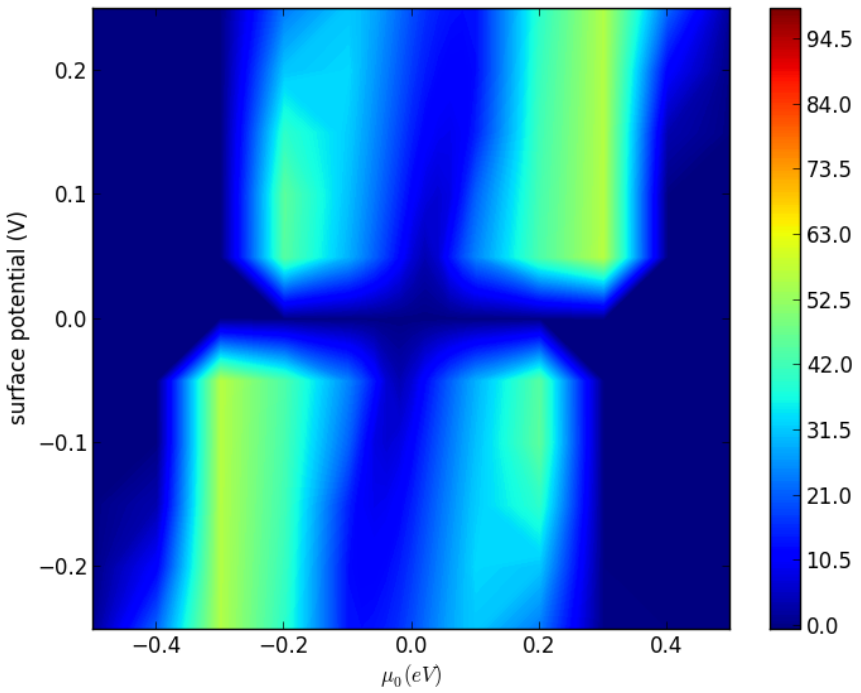

Figure 6.17: The percentage screening difference between the bi-layer and mono-layer stack models for variable μ_0 and V.

Here the doping level is displayed on the x axis and the substrate surface potential on the y axis. The surface represents the percentage of screening between the bi-layer and mono-layer stack models at the surface of the graphene, the colour bar represents the percentage screening. This shows that large levels of doping cause the difference between the two models to become zero, this is because of the energy reaching higher levels than the t′ values, thus causing the second set of bands to affect the number of states. The overall effect of the difference between the two models is insignificant for small doping values, or combinations of surface potentials and doping levels that cause the overall energy to exceed the value of t′. From this point forward the approximation will be made that n-layers can be considered to be mono-layer stacks. However, for a two layer stack care will be taken in selecting parameters that will not cause the bilayer to be greatly different from the mono stack (as shown by the four regions in the figure). For increasing layers past bilayer, the layers become increasingly decoupled.

6.3.2 Comparison to literature

As mono-layer stacks have been shown to be accurate when calculating the density of bi-layer graphene, next the stage is to implement n-layers of stacked mono-layer graphene. This is fairly simple and only involves the extending of the graphene z range. The simulation will now be compared to experimental values from literature [11]. Here the experiment results were obtained from differing thicknesses of graphene placed on a silicon wafer with an insulating SiO_2 interface between the silicon and graphene. The substrate surface charge on the graphene was due to charges within the SiO_2 interface. Here the graphene had a large lateral extent and the substrate surface charge was considered uniform, because of this, the system can be thought of as having only one variable, z. This can be described by the model presented in the previous section. Next the simulation was compared to the experimental values by performing simulations for different layers of graphene thickness and parameters of doping and substrate surface potential. Here the literature fits the decay through many layers of graphene to an inverse power law with the exponent of the inverse power law being equal to two, as shown in equation 6.42.

$$V = \frac{-10.3k}{D^2} \tag{6.42}$$

where k is the dielectric constant of the graphene/SiO_2 interface and D is the distance from the surface of the substrate. The simulation however, showed that not all parameters produced data that could reliably fitted to a power law. Large doping values greatly decreased the R squared values of the fits. The simulation therefore suggests that a power law is only reliably describes the screening through graphene for low dopant values. It was found that a surface substrate potential of approximately -3.5V best matched the experimental values. Figure 6.18 shows the values of the fitted power law exponents for different dopant values, the surface potential is set to -3.5V.

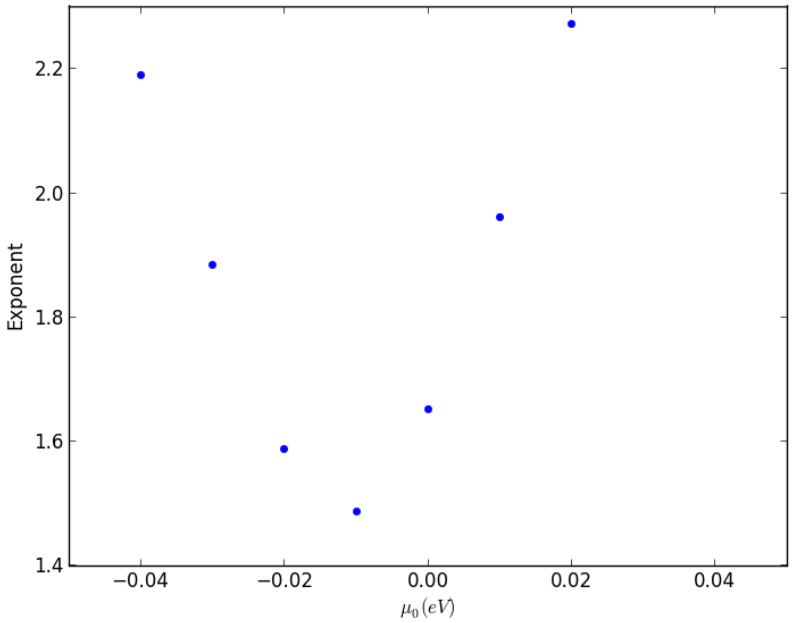

Figure 6.18: The exponent of a power law fit through simulated data for varying dopant levels.

The results from this show that the exponent is parabolic with dopant level, here it is clear that a value of approximately 0.01 or just below -0.03eV will fit to the experimental data. The fit for -0.03eV has a significantly lower R squared value than the fit of 0.01eV, and therefore the value of 0.01eV was selected to compare to the experimental data. The literature also proposes a one dimensional nonlinear Thomas-Fermi model[82], which is shown in figure 6.19 as lines. Each line represents screening as a function of background dielectric constants, where k=2 (red), 2.5 (black) and 3(blue). The blue markers show results from the simulation using a doping level of 0.01eV and a potential of -3.5V.

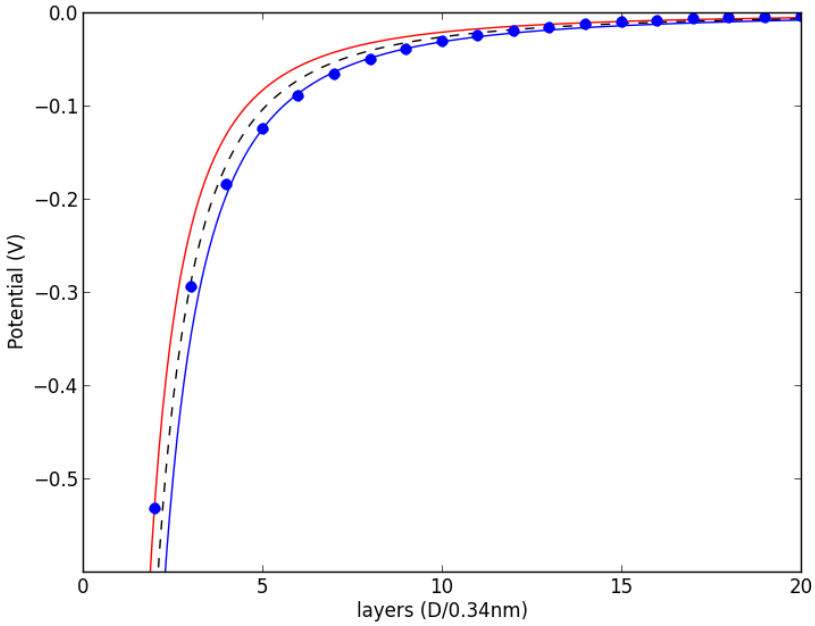

Figure 6.19: Simulation data (Blue points) for a surface potential of -3.5V and a dopant level of 0.01eV. Lines show fits from experimental data.

As shown in this figure the fit is reasonable, however not exact. This results shows that the approximation of mono-layer stacked graphene is acceptable and further validates the simulation.

6.4 Screening of localised potential distributions by graphene layers

6.4.1 Modelling experimental data

Now that the simulation has been shown to be able to reproduce data from literature, the simulation will now be extended to work with data previously shown in this thesis. Here the focus is on surface potentials that vary with lateral extent (e.g. on x), however are continuous along another axis (e.g. on y),i.e lines of charge. This will allow the simulation to be modelled in two dimensions, the decay from the surface (along z) and the axis of varying charge along the surface is y. To estimate the surface potential width the STM image 6.20 will be considered. Here bi-layer graphene is placed on a KBr substrate. The substrate contains a square atomic indentation in its surface.

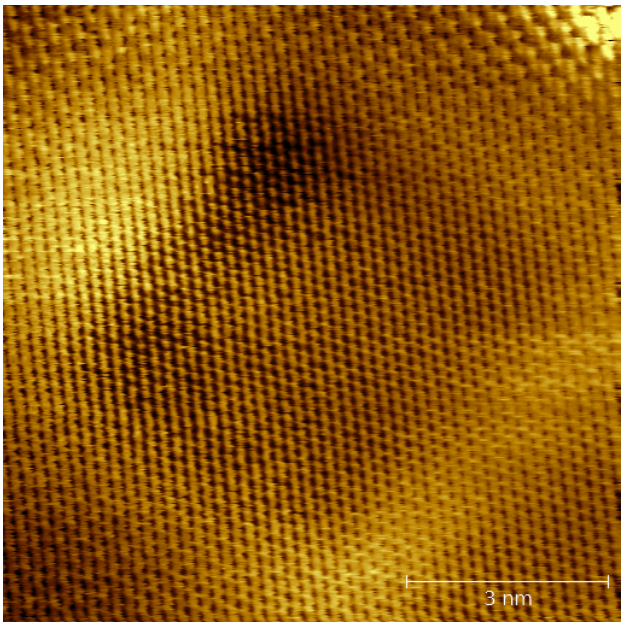

Figure 6.20: An STM scan of an area of bi-graphene covering a KBr surface, the surface contains a square depression creating significant surface potential along its edges.

Although the potential variation in the bi-layer graphene cannot be measured using STM, the change in the local density of state (LDOS) can be observed, which directly relates to the potential variation within graphene. Therefore the measured width across the step edges in the STM image can be used to find the potential width across a step edge, shown in figure 6.21.

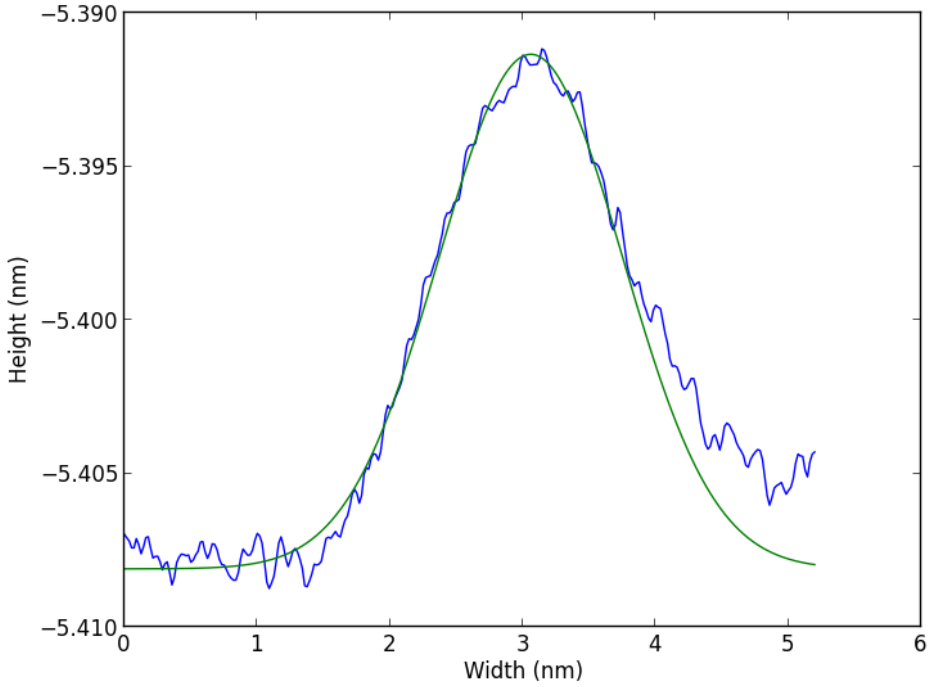

Figure 6.21: An averaged height trace taken from the STM image across of bi-layer graphene above a step edge (blue). Green shows a Gaussian fitted to the data. Several estimations of the width were made, approximating the correct full width half maximum (FWHM) of the Gaussian to be between 2.1nm and 2.3nm.

Here the trace over the STM image shows that the width of the potential over the step has a Gaussian σ term of between 0.9 and 1 nm.. However this is not the true potential width of the step, as it is measured above bi-layer graphene placed on the step. The potential width above the step however, can be discovered by running multiple simulations for bilayer graphene above a step edge with varying width and potential. The remaining unknown parameters is the doping level μ_0 within graphene, this can be measured directly from a STM spectroscopy measurement, which gave a value of approximately 25mV. Now multiple simulations were performed using multiple values of potential width and magnitude with bi-layer graphene, as shown in figure 6.22.

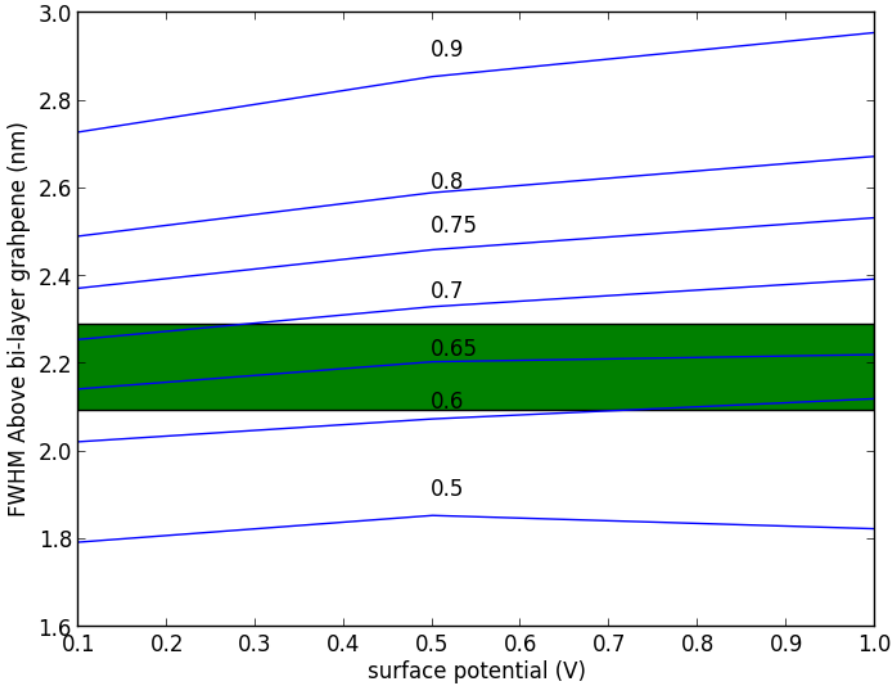

Figure 6.22: The results from multiple simulations to calculate the FWHM above bi-layer graphene, using different values of substrate surface potential magnitude and width. x and y axis show the substrate surface potential and FWHM above bi-layer graphene respectively. Blue lines indicate the FWHM above the bilayer graphene using differing values of surface potential width (notated by their Gaussian sigma term). The green box indicates acceptable values of surface potential width as previously found from STM data.

Here the x and y axis show the substrate surface potential and the FWHM above the graphene bi-layer repectivley. The multiple lines within the figure correspond to different values of surface potential width (Gaussian σ terms). Here the width above bi-layer is known, so the surface potential width can be found to be around this value, shown by the green box. Here the approximate value of surface potential width is 0.65nm.

Previously the effects of the measuring tip were not considered. Now however, since the potentials being measured are generated over an atomic step in a crystal lattice, the physical size of the tip is of greater importance as it will create a broadening of the measured surface potential and will affect the magnitude of the measured potential. The data sheet for the tip approximates the tip radius to be 28 $\pm$10 nm (Asylum research ASYELEC-01), this is significantly larger than the atomic step.

To account for the tip size, the simulation data will be convoluted with a tip function.

As the error on the approximation is significantly large, the value given in the data sheet cannot be considered reliable, therefore the tip needs to be measured. As the surface features of the substrate are well known and are very fine structures, they can be used to estimate the size of the tip.

As shown with the STM image, the lateral size of the potential is very small compared to the size of the tip. To measure the tip size, a blind estimation algorithm is preformed on the SKPM data using Gwyddion (A SPM visualization and analysis tool [83]) along with an estimate using the tip geometry from the manufacturers specification. The blind estimation algorithm takes the manufacturers specification and is able to model the tip by iterating over the entire surface of the scan, and measuring the slope and direction of surface features relative to the tip. In this way the algorithm is able to model both the slope of the tip and the size of the apex. This method works best for large surface features, but as shown here is able to give a reasonable model for small surface features. As shown in figure 6.23 the blind estimation is performed. In figure (a) the sample surface is show, figure (b) shows the estimated tip shape is shown.

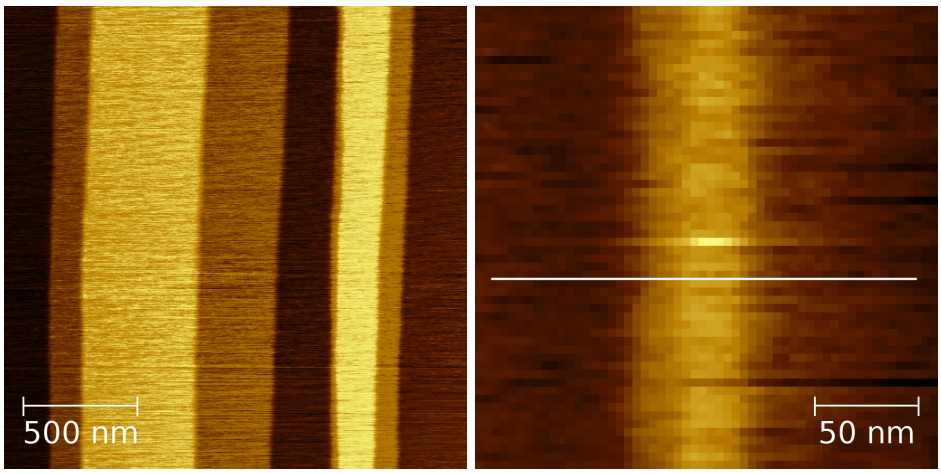

(a) (b)

Figure 6.23: (a) Shows the topography scan above a bare KBr surface, (b) shows the tip modelled from the surface (a). White line on (b) indicates where data was extracted from for figure 6.24.

The tip appears as a line in the vertical as there is no vertical data in the original image for the algorithm to be performed on, and therefore cannot make an estimation on the tips dimensions in this direction.

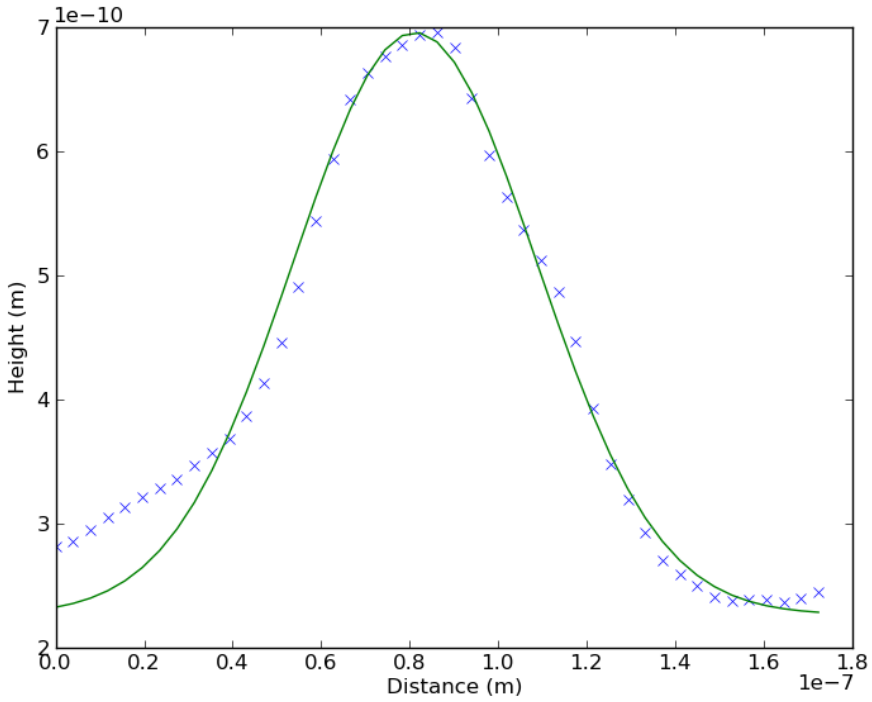

Figure 6.24: An averaged cross section of the tip model, blue crosses indicate extracted tip, green shows a Gaussian fitted to the data.

The surface potential will now be estimated by taking into account the tip size. First a simulation is performed using the potential width estimated from the STM data (from figure 6.24), and an initial value of surface potential is chosen. Figure 6.25 shows a map of the simulated potential variation across a bare edge parrallel to the x axis and at height z above the surface.

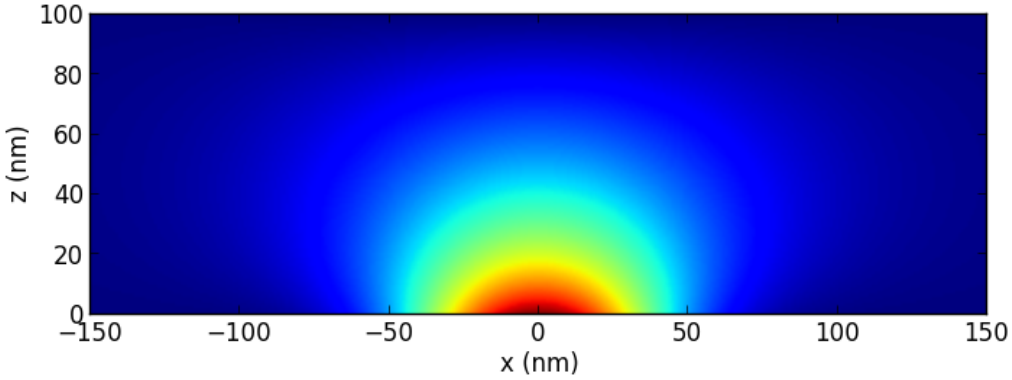

Figure 6.25: Map of convolved simulated potential, potential applied at the substrate (z = 0).

This potential is now convolved using the tip function to create a simulation that is comparable to the measured experimental data. The experimental data is extracted from a terrace edge at each height above the substrate, using a Gaussian fitting routine[83], giving the two fitting parameters maximum potential V_0 and the width σ. The extracted experimental data can now be compared to the convoluted simulation data, here the measured parameters from the experimental data are reconstructed into a Gaussian and compared to the convoluted simulation at each measured height (as in the set of images in figure 5.3) using the coefficient of determination (R squared).

This process is then repeated using a range of surface potential values as input in the simulation. Once this process has finished, the simulation that produces the lowest R squared value is considered to be best fitting to the experimental data, and thus the value of surface potential V_0 used in the simulation parameters is estimated to be the source surface potential of the experimental data. This process is now used to estimate the surface potential of the experimental data shown in figure 6.26. The two figures here show the convoluted simulation (blue) compared to the experimental data (green) for, (a) the potential of and (b) the width as a function of height (i.e. distance above surface).

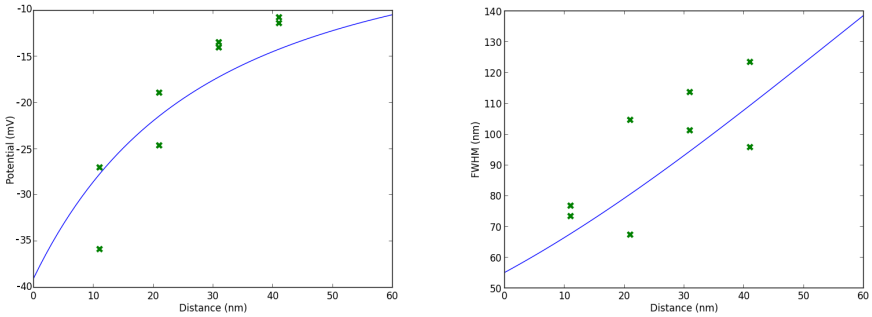

(a) (b)

Figure 6.26: Figure (a) shows the extracted potential data above the bare KBr substrate at differing heights (blue points) extracted from figure 5.3, with a simulation that has been convoluted with the tip model (blue). (b) shows the measured full width half maximum from the same data points as (a) (green), with the convoluted simulation full width half maximum (blue).

Figure 6.27 shows the potential as a function of height for the convoluted simulation and experimental data, with the simulation prior to the convolution (red), to highlight the magnitude of the convolving effect

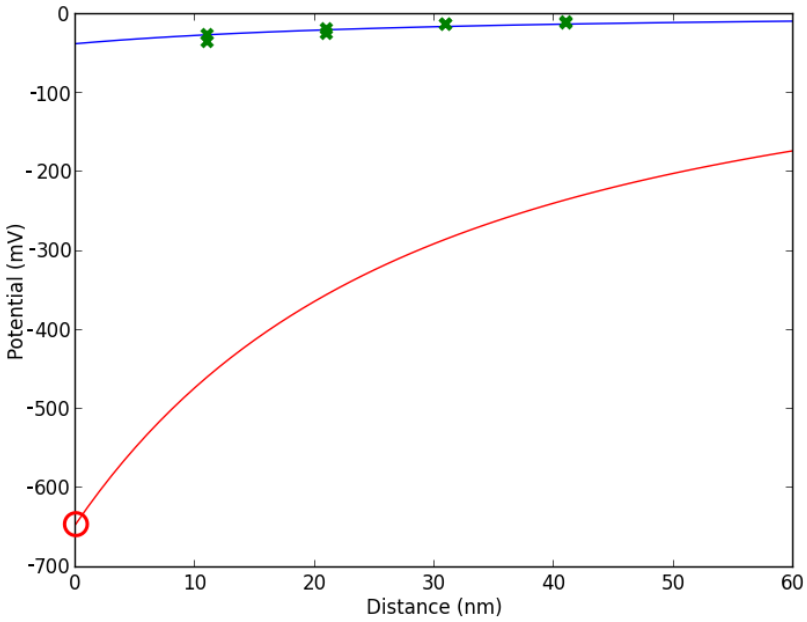

Figure 6.27: The potential as a function of height as determined by the iterative procedure as described in text (red), convoluted with the tip (blue) fitting the experimental data (green crosses). Simulated at the surface of the substrate with a surface potential of -650mV (Circle).

Now that the surface potential has been successfully extracted for a terrace on a bare substrate, the potential variation through graphene will be explored. Here the potential is extracted from experimental data taken above graphene covering KBr terrace step edges. The first scan that will be analysed contains a region of four layer graphene and the bare substrate, figure 5.12 show the topography and the SKPM scan of this region. The area covered with the four layer graphene is the bottom left, which can clearly be seen in the SKPM scan due to the magnitude of the screening caused by four layers of graphene, previously shown in figure 5.12.

Figures 6.28(a) and 6.28(b) show the experimental potential and the width of the potential varying with the height above the surface of the bare section of the substrate. These points are then fitted using a simulation using the same method as previously discussed.

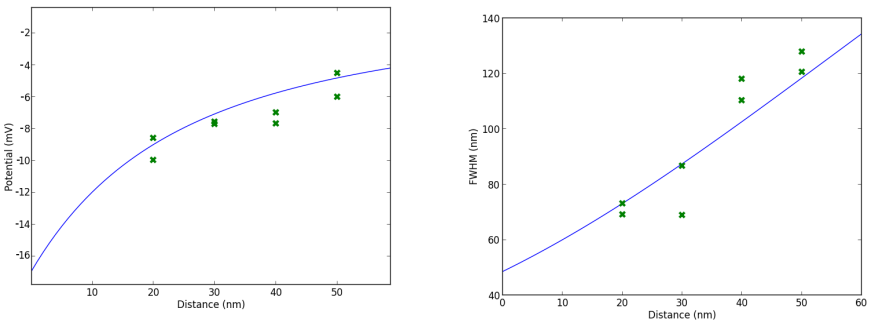

(a) (b)

Figure 6.28: Experimental data (a) potential and (b) potential width above the bare KBr substrate. Blue lines indicate the simulated decay convoluted with the modelled tip, that fitted the data.

Figure 6.29 shows the experimental data (green), the simulation describing the convolution with the tip (blue), and the deconvoluted variation of the potential (red), all as a function of the distance from the surface.

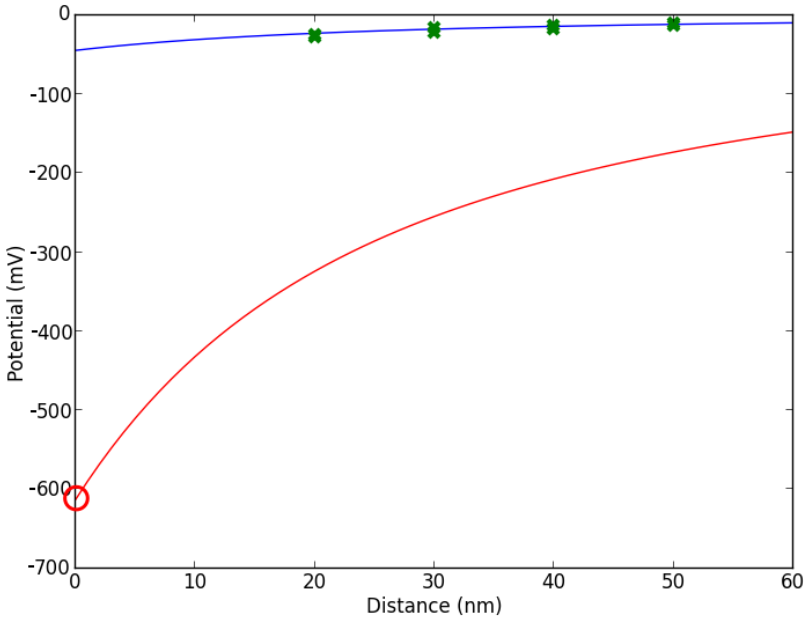

Figure 6.29: The reversal of the convolution process (shown in red), revealing the true surface potential of -614mV (marked with a circle) of the bare KBr terrace.

We note that the resulting values from fig 6.27 and 6.29 agree, which gives confidence in the method. Now that the surface potential of the bare substrate has been determined, the simulation used this value to predict the decay of the potential through the region of four layer FLG. Figure 6.30 shows the potential at the substrate (blue) and at the surface of the four layer graphene (green); this highlights the magnitude of the screening through the multiple layers of FLG. In this case the four layer FLG was modelled as a stack of independent layers, as in section 6.3.

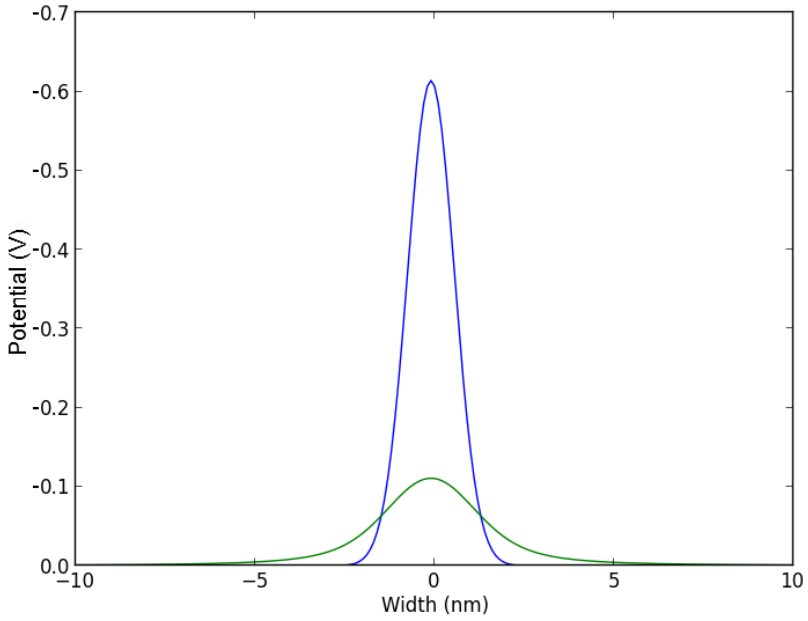

Figure 6.30: The simulation of screening through four layers of graphene using a surface potential of -614mV. Blue shows the potential at the surface of the substrate, green shows the potential at the surface of the four graphene layers, showing a surface potential of -111mV.

The simulation for the four layers is now convoluted using the same tip function as used with the bare substrate from the same scan, as shown in figures 6.31(a) and 6.31(b). The convoluted simulation approximates the experimental data, therefore the simulation and convolution has correctly approximated the experimental system.

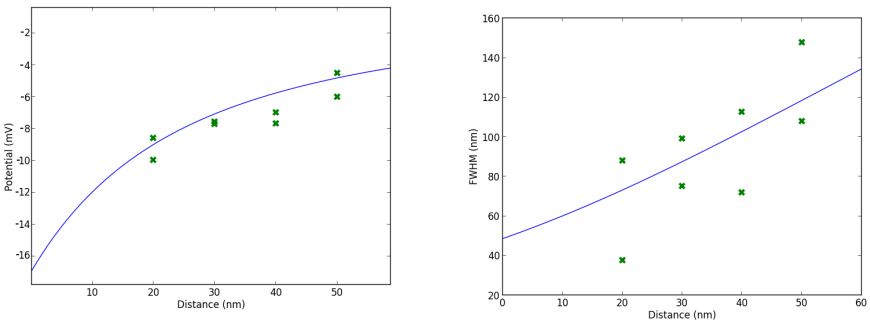

(a) (b)

Figure 6.31: Measured experimental data for potential magnitude (a) and width above the four graphene layers (b). Blue lines indicate the simulated decay convoluted with the modelled tip.

Next, an image containing regions of two and three layers of graphene is analysed (figure 5.14). Here there are no terrace edges that are not covered by graphene, therefore the surface potential must be approximated from data extracted above the graphene. Figures 5.14 (a) and (b) show the topographic and SKPM images of the bi- and tri-layers of graphene, with the bi- and tri- regions indicated by contours.

First the potential through the bi-layer FLG will be considered. As with previous experimental data, the surface potential without the effects of the tip is unknown and therefore simulations using a range of surface potentials are performed and convoluted to estimated the substrate surface potential. Figure 6.32 shows the convoluted simulation with the experimental data for the potential and potential width varies with the distance above the surface for the bi-layer FLG.

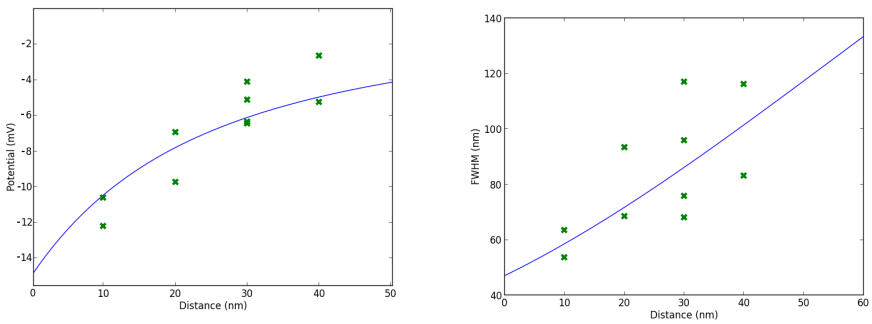

(a) (b)

Figure 6.32: Potential (a) and potential width (b) as a function of distance above the surface, experimental data pointes in green, and convoluted simulation in blue for bi-layer FLG.

By using different values as input for the source potential at the substrate surface and deconvoluting the results from figure 6.32, a value of -450mV was obtained at the bare substrate, -153mV and -135mV at the surface of the bi- and tri-layer FLG, as shown in figure 6.33.

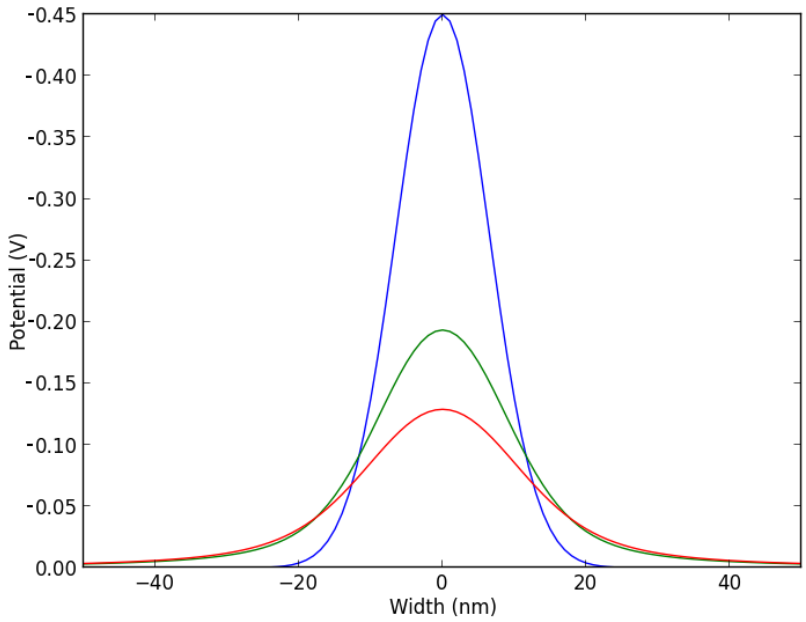

Figure 6.33: Potential at the surface of the substrate (blue), above the bi-layer (green) and above the tri-layer (red), With potentials -450mV, -193mV and -139mV respectively.

Figure 6.34 shows the simulated tri-layer convoluted and plotted against the experimental data, here the simulation is shown to fit the experimental after convolution.

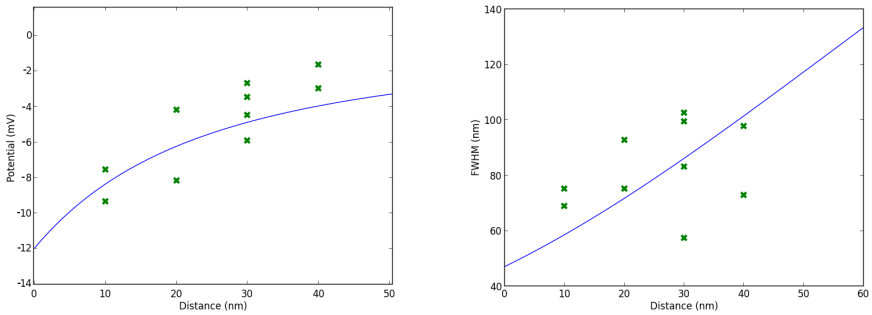

(a) (b)

Figure 6.34: Potential (a) and potential width (b) as a function of distance above the surface, experimental data pointes in green, and convoluted simulation in blue for tri-layer FLG.

6.4.2 Pure simulation

Now that the simulation has been shown to produce reliable results as compared to experimental data through different thicknesses of few layer graphene, the simulation will be run for different parameters, to further explore the nature of graphene screening. First the screening of potential as a function of number of graphene layers will be explored. Here three potential values are used as parameters, 0.1, 0.5 and 1.0V. The potential width is set to that of what is expected to be produced by a terrace step edge, i.e. 0.65nm for the σ term and using 0.025V for the μ_0 term. The number of graphene layers is ranged from zero to ten, then the screening percentage is taken from each layer and plotted in figure 6.35. For the measured surface potential 0.5V, the potential is shown to fall to approximately 0.3V, which compares well to DFT and charge dipole models performed on similar steps [50].

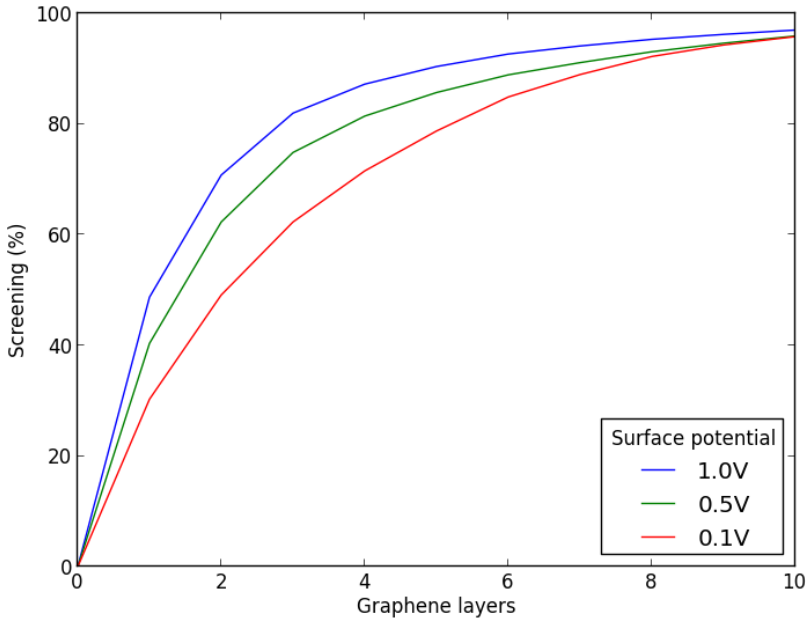

Figure 6.35: Percentage screening as a function of number of graphene layers for 1.0V (blue), 0.5V (green) and 0.1V (red). using 0.65nm for the σ term of the potential width and 0.025V for the μ_0 term.

Here it is shown again that larger potentials induce a larger amount of screening through graphene. The reason for the drop of percentage screening with increasing layers is due to the potential drop caused by the screening, after each layer there is less

potential to induce screening in the next layer of graphene and therefore the screening is less significant. Screening not only affects the potential but also the potential width. Figure 6.36 shows the full-width-half-maximum of the potential as a function of number of graphene layers.

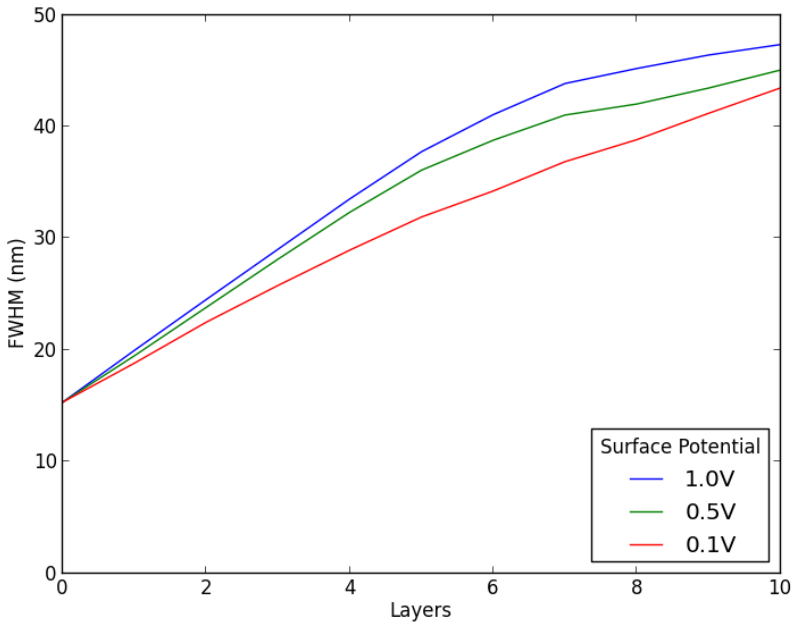

Figure 6.36: Potential width as a function of graphene layers for different potentials, 1.0V (blue), 0.5V (green) and 0.1V (red).

As shown at zero layers, each set of simulations uses the same starting width, however the screening by graphene causes a broadening of the potential width. The higher potential causes a greater broadening than the lower potentials, therefore the increased screening also increases the magnitude of the broadening.

6.5 Summary of modelling results

In summary, the numerical implementation of the Thomas-Fermi model for potential screening by graphene layers that was implemented in this chapter yielded the following main results:

- As a test, the model was able to describe previous data of screening of 2D, uniform potential distributions [11].

- As an original result, the model is able to model local electrostatic sources, with lateral variations, which are situations not covered by any previous work. It highlighted that in such cases screening effects depend not only on the magnitude of the potential but also on the lateral spread of the potential.

- The percentage of screening depends on both the doping regime of graphene and the magnitude of the potential being screened. We also mapped the parameter space of chemical potential (doping level) and surface potential for which screening by multilayer graphenes can or cannot be approximated by stacks of independent monolayers. For example, the model shows that at high doping levels but below the onset of the second parabolic bands in bilayer graphene, there is substantial difference, up to about 50%, in the percentage screening difference between interacting and non-interacting layers in the stacks.

- Using this model in conjunction with experimental data sets of surface potential it was possible to determine the unknown magnitude of localized potentials generated by nanostructures in ionic surfaces and the induced potential felt by the graphene electrons.

- Importantly, the model is in broad agreement with ab-initio modelling by DFT of real systems, such as polar edges of terraces of ionic surfaces[50].

Appendix A

Implementation of the relaxation model

Full simulation code for the relaxation model used in chapter 6

```
PROGRAM GRAPHENE_SOR

IMPLICIT NONE

! SOR ALGORITHM FOR SINGLE AND BILAYER GRAPHENE
! MUST BE SUPPLIED WITH 4 INPUT PARAMETERS
! 1 SURFACE POTENTIAL
! 2 SURFACE POTENTIAL LATERAL EXTENT, WIDTH - TOP HAT FUNCTION, SIGMA - GAUSSIAN FUNCTION
!   GIVEN IN ANGSTROMS
! 3 NUMBER OF GRAPHENE LAYERS
! 4 MU_0 GRAPHENE

! EXAMPLE COMPILE AND RUN
! COMPILE WITH GFORTRAN!# gfortran -o OUT Graphene_SoR.f90
! RUN !# ./OUT 1.0 1.0 1.0 0.1

! NOTES
! USE FOR 3D WILL REQUIRE EXTRA WORK FOR THE WHOLE SIMULATION GRID TO BE SAVED, SAVING IS CURRENTLY VERY BASIC
! CODE IS NOT LINEAR, INCREASING SIMULATION GRID SIZE WILL SIGNIFICANTLY INCREASE RUN TIME
! TO RUN 1D SIMULATIONS SET M=1, N = 1, (ZELEMENTS, 1, 1) = U,RHO
!       2D SIMULATIONS SET M1=1, (ZELEMENTS, 1, XELEMENTS) = U,RHO


! SIMULATION GRID SELEMENTS
INTEGER :: L = 500 !Z
INTEGER :: M = 1
INTEGER :: N = 500 !X

! L -Z , M - Y, N - X
! THIS SHOULD ALWAYS EQUAL THE ELEMENTS L, M AND N
DOUBLE PRECISION, DIMENSION(500,1,500) :: U,RHO

INTEGER :: I,J,K

INTEGER :: NX,NY,NZ
DOUBLE PRECISION :: AX,BX,AY,BY,AZ,BZ,T
DOUBLE PRECISION :: XSTEP,YSTEP,ZSTEP
REAL :: W

REAL :: CELLPOT
REAL :: STEPWIDTH
CHARACTER(LEN=100) :: STEPWIDTHIN,MIDXIN, LAYERS, MUNAUGHTIN
```

```
CHARACTER(LEN=10)  ::  CELLPOTIN

INTEGER  ::  NIN

INTEGER  ::  NCELLS
REAL  ::  CELLSPACE

INTEGER  ::  NLOOP, IT, IMOD
INTEGER  ::  TOL
INTEGER  ::  NCTEST, BOUNCE

INTEGER  ::  THSTART, THEND,  GMUSGN
DOUBLE PRECISION  ::  ANORM, RES, PREV
DOUBLE PRECISION  ::  SIGMA, GAUMU, GMID, PI
DOUBLE PRECISION  ::  E, HBAR, E0
DOUBLE PRECISION  ::  VF, ER, GTHICK, N0, N0MOD, SFIND, SGN, GMU, NLAYERS
DOUBLE PRECISION  ::  AGAU, BGAU, CGAU
DOUBLE PRECISION  ::  ODDEVEN, PM, STEPWIDTHL, MIDX
DOUBLE PRECISION  ::  TBI, TPRIME, ABI, GBI, BIGMU, N0BI, GCONST, N0BIMOD, N0BIHIGH
DOUBLE PRECISION  ::  MUNAUGHT
LOGICAL  ::  USEBILAYER, USEGAUSSIAN
NIN = IARGC()

E = -1.6E-19
HBAR = 1.05457E-34 ! IN J
HBAR = 6.58211928E-16
E0 = 8.854187817E-12 ! IN J
PI = 3.14159265359

CALL GETARG(3,LAYERS)
READ(LAYERS,*) NLAYERS

CALL GETARG(4,MUNAUGHTIN)
READ(MUNAUGHTIN,*) MUNAUGHT

print *,LAYERS
print *,MUNAUGHT
USEBILAYER= .FALSE.

! SUBSTRATE POTENTIAL
USEGAUSSIAN = .FALSE.

! GRAPHENE CONSTANTS----------------------------------
VF = 1E6
ER = 2.5
GTHICK = 1.5E-10
GTHICK = 3.4E-10

GMU = -MUNAUGHT*E
IF (GMU >=0.0) THEN
  GMUSGN = 1
ELSE
  GMUSGN = -1
END IF
GCONST = (HBAR**2)*(VF**2)
N0 = GMUSGN*(((GMU/E)**2)/(PI*(HBAR*VF)**2))*(1.0/GTHICK)
! END GRAPHENE CONSTANTS ------------------------------------

! BI-LAYER GRAPHENE CONSTANTS -------------------------
TBI = ABS(-3.0*E) ! EV
TPRIME = ABS(-0.3*E)
ABI = 2.46 !ANG
GBI = (SQRT(3.0)*TBI*ABI)/(2.0)
BIGMU = 0.1*E

BIGMU = (-MUNAUGHT*E)

IF (BIGMU >=0.0) THEN
  GMUSGN = 1
ELSE
  GMUSGN = -1
END IF

! CALCULATE THE DOPING WITHIN BI-LAYER GRAPHENE
! N0BI AND N0BIHIGH - DOPING BELOW AND ABOVE TPRIME
```

```
N0BI = GMUSGN*(abs(BIGMU/E)*(abs(BIGMU/E)+TPRIME))/(PI*GCONST)*(1.0/(2.0*GTHICK))
N0BIHIGH = GMUSGN*2.0*(((BIGMU/E)**2)/(PI*GCONST))*(1.0/(2.0*GTHICK))

! SIMULATION STEP SIZE
XSTEP = 1.0E-10
YSTEP = 1.0E-10
ZSTEP = 1.0E-10

! SET EMPTY SIMULATION ARRAYS
DO I=1,L
  DO J=1,M
    DO K=1,N
      U(I,J,K) = 0.0
      RHO(I,J,K) = 0.0
    END DO
  END DO
END DO

NZ = L
NY = M
NX = N

! FIRST ARG FROM COMMAND LINE - SUBSTRATE SURFACE POTENTIAL
CALL GETARG(1,CELLPOTIN)
READ(CELLPOTIN,*) CELLPOT

! COMMAND LINE ARG - POTENTIAL WIDTH TOP HAT - SIGMA TERM GAUSSIAN
CALL GETARG(2,STEPWIDTHIN)
READ(STEPWIDTHIN,*) STEPWIDTH
STEPWIDTHL = STEPWIDTH

! POTENTIAL WIDTH MODIFIER
STEPWIDTH = STEPWIDTH*1E-10

! THE VALUE THE ANORM VALUE MUST FALL BELOW BEFORE THE MAIN LOOP EXISTS
TOL = 1000

! RELAXATION TERM - SHOULD BE SET BETWEEN 1 and 1.99
W = 1.5

! SOR SETUP
AX = NEAREST(1.0/(XSTEP**2),1.0)
BX = AX

AY = NEAREST(1.0/(YSTEP**2),1.0)
BY = AY

AZ = NEAREST(1.0/(ZSTEP**2),1.0)
BZ = AZ

T = -(AX+BX+AY+BY+AZ+BZ)

! SETUP BACKGROUND POTENTIAL
NCELLS = INT(STEPWIDTH/XSTEP)

IF (NCELLS < -2000) THEN
  NCELLS = 1000000
END IF

IF (MODULO(NCELLS,2)==0) THEN
  CELLSPACE = NCELLS/2.0
ELSE
  CELLSPACE = (NCELLS-1.0)/2.0
END IF

! FIND MIDDLE OF X AXIS
ODDEVEN = MODULO(NX-STEPWIDTHL,2.0)
PM = FLOOR(STEPWIDTHL/2.0)

! TOP HAT SETUP
THSTART = FLOOR(NX/2.0)-FLOOR((STEPWIDTH*1E10*((1E-10)/XSTEP))/2.0)
THEND = THSTART + STEPWIDTH*1E10*((1E-10)/XSTEP)

! GAUSSIAN SETUP
SIGMA = 0.65131
```

```
GAUMU = 1.0987E-9
GMID = NX/2.0

SIGMA = 1.0987E-9
SIGMA = STEPWIDTH

AGAU = CELLPOT
BGAU = GMID
CGAU = SIGMA

! APPLY POTENTIALS TO SURFACE
! GAUSIAN FUNCTION
IF (USEGAUSSIAN .EQV. .TRUE.) THEN
  DO K=1,NX
    U(1,1,K) = AGAU*EXP(-((K*XSTEP-BGAU*XSTEP)**2)/(2.0*CGAU**2))
  END DO
ELSE
  ! TOP-HAT FUNCTION
  DO K=1,NX
    IF ((K >= THSTART) .AND. (K <= THEND)) THEN
      U(1,1,K) = CELLPOT
    ELSE
      U(1,1,K) = 0.0
    END IF
  END DO
END IF

! UNIFORM BACKGROUND POTENTIAL
!DO K=1,NX
!     U(1,1,K) = CELLPOT
!END DO

! BOUNCE STOPS A SIMULATION IF IT BECOMES STUCK IN A UNRELAXED STATE
BOUNCE = 0

ANORM = 0.0
RES = 0.0
PREV = 1E30

! MAIN ALGORITHM
DO NLOOP = 1,10000000
  ! IT - USED TO PRODUCE A CHECKERBOARD ITERATION ACROSS THE SIMULATION ARRAY
  DO IT=0,1
    ANORM = 0.0
    DO I=1,NZ
      DO K=1,NX
        ! CALCULATE DENSITY
        ! BI-LAYER
        IF (USEBILAYER .EQV. .TRUE.) THEN
          ! CHECK IF SIMULATION IS WITHIN THE GRAPHENE
          IF ((I*ZSTEP) <= (NLAYERS*GTHICK+1*ZSTEP)) THEN
            SFIND = BIGMU + E*U(I,1,K)
            IF (SFIND < 0) THEN
              SGN = -1
            ELSE IF (SFIND > 0) THEN
              SGN = 1
            ELSE
              SGN = 0
            END IF
            ! DOS IS DIFFERENT IF WE ARE ABOVE OR BELOW TPRIME
            IF (ABS(SFIND) < ABS(TPRIME)) THEN
              N0BIMOD = SGN*((1.0*abs(SFIND/E)*(abs(SFIND/E)+TPRIME))/(PI*GCONST))
              RHO(I,1,K) = (-E*(N0BIMOD-N0BI))
            ELSE
              N0BIMOD = SGN*2.0*(((SFIND/E)**2)/(PI*GCONST))*(1.0/(2.0*GTHICK))
              RHO(I,1,K) = (-E*(N0BIMOD-N0BIHIGH))
            END IF
          ELSE
            ! IF WE ARE OUTSIDE OF THE GRAPHENE THE DOS IS ZERO
            RHO(I,1,K) = 0.0
          END IF
        ELSE
          ! MONO-LAYER STACKS
          ! CHECK IF SIMULATION IS WITHIN GRAPHENE
          IF ((I*ZSTEP) <= (GTHICK*NLAYERS+1*ZSTEP)) THEN
```

```
            ! CALCULATE SGN FUNCTION
            SFIND = (GMU + E*U(I,1,K))
            IF (SFIND < 0) THEN
              SGN = -1
            ELSE IF (SFIND > 0) THEN
              SGN = 1
            ELSE
              SGN = 0
            END IF
            ! Rho induced = -e(n0(mu + e*psi(r)) - n0(mu))
            N0MOD = ((SGN*(SFIND/E)**2)/(PI*(HBAR*VF)**2))*(1.0/GTHICK)
            RHO(I,1,K) = (-E*(N0MOD-N0))
          ELSE
            ! IF WE ARE OUTSIDE OF THE GRAPHENE THE DOS IS ZERO
            RHO(I,1,K) = 0.0
          END IF
        END IF
      END DO
    END DO

    ! CALCULATE NEW VALUE OF POTENTIAL
    DO I=2,(NZ-1)
      ! CHECKERBOARD ITERATION
      IMOD = MODULO((IT+I),2)
      DO K=2+IMOD,(NX-1),2
        ! MAIN SOR ALGORITHM
        RES = AZ*U(I+1,1,K) + AZ*U(I-1,1,K) + AY*U(I,1,K) + AY*U(I,1,K) + AX*U(I,1,K+1) + AX*U(I,1,K-1) + T*U(I,1,K)
        RES = RES + (RHO(I,1,K))/(E0*ER)
        ANORM = ANORM + ABS(RES)
        U(I,1,K) = U(I,1,K)-W*(RES/T)
      END DO
    END DO

  END DO


  ! PRINT OUT DEBUG VALUES
  IF (MODULO(NLOOP,1000) == 0) THEN
    PRINT *,W,NLOOP,ANORM,RES!,RHO(1,1,10)!,U(1,1,1)
    IF (ANORM >= PREV) THEN
      BOUNCE = BOUNCE +1
    ELSE
      PREV = ANORM
    END IF
  END IF

  ! IF WE REACH OUR END CONDITIONS, EXIT THE LOOP
  IF (ANORM < TOL) THEN
    EXIT
  END IF
  IF (BOUNCE >20) THEN
    EXIT
  END IF
END DO

! OPEN FILE FOR WRITING
OPEN(UNIT=1,FILE="2D_OUT_TEST",STATUS='REPLACE')

! WRITE FILE HEADER
IF (USEGAUSSIAN .EQV. .TRUE.) THEN
    WRITE (1,*)'x',XSTEP,'y',YSTEP,'z',ZSTEP,'W',STEPWIDTH,'GAU',CELLPOT,'V_SECOND',NLAYERS,'L',MUNAUGHT,'muN'
    WRITE (*,*)'x',XSTEP,'y',YSTEP,'z',ZSTEP,'W',STEPWIDTH,'GAU',CELLPOT,'V_SECOND',NLAYERS,'L',MUNAUGHT,'muN'
ELSE
    WRITE (1,*)'x',XSTEP,'y',YSTEP,'z',ZSTEP,'W',STEPWIDTH,'STEP',CELLPOT,'V_SECOND',NLAYERS,'L',MUNAUGHT,'muN'
    WRITE (*,*)'x',XSTEP,'y',YSTEP,'z',ZSTEP,'W',STEPWIDTH,'STEP',CELLPOT,'V_SECOND',NLAYERS,'L',MUNAUGHT,'muN'
END IF

! WRITE OUTPUT TO FILE, THIS WILL NOT WORK FOR A 3D SIMULATION
DO I=1,NZ
  DO J=1,NY
    DO K=1,NX
      WRITE(1,'(F45.40,X)',ADVANCE='NO') U(I,J,K)
    END DO
    WRITE(1,*)
  END DO
```

```
END DO

END PROGRAM GRAPHENE_SOR
```

Bibliography

[1] JR Williams, Tony Low, MS Lundstrom, and CM Marcus. Gate-controlled guiding of electrons in graphene. *Nature nanotechnology*, 6(4):222–225, 2011.

[2] JR Williams, L DiCarlo, and CM Marcus. Quantum hall effect in a gate-controlled pn junction of graphene. *Science*, 317(5838):638–641, 2007.

[3] G Trambly de Laissardiere, Didier Mayou, and Laurence Magaud. Localization of dirac electrons in rotated graphene bilayers. *Nano letters*, 10(3):804–808, 2010.

[4] Cheol-Hwan Park, Li Yang, Young-Woo Son, Marvin L Cohen, and Steven G Louie. Anisotropic behaviours of massless dirac fermions in graphene under periodic potentials. *Nature Physics*, 4(3):213–217, 2008.

[5] Matthew Yankowitz, Jiamin Xue, Daniel Cormode, Javier D Sanchez-Yamagishi, K Watanabe, T Taniguchi, Pablo Jarillo-Herrero, Philippe Jacquod, and Brian J LeRoy. Emergence of superlattice dirac points in graphene on hexagonal boron nitride. *Nature Physics*, 8(5):382–386, 2012.

[6] Jens Martin, N Akerman, G Ulbricht, T Lohmann, JH Smet, K Von Klitzing, and Amir Yacoby. Observation of electron–hole puddles in graphene using a scanning single-electron transistor. *Nature Physics*, 4(2):144–148, 2007.

[7] CR Dean, AF Young, I Meric, C Lee, L Wang, S Sorgenfrei, K Watanabe, T Taniguchi, P Kim, KL Shepard, et al. Boron nitride substrates for high-quality graphene electronics. *Nature nanotechnology*, 5(10):722–726, 2010.

[8] Stefan Egger, Adelina Ilie, Yiton Fu, Jeffrey Chongsathien, Dae-Joon Kang, and Mark E Welland. Dynamic shadow mask technique: A universal tool for nanoscience. *Nano letters*, 5(1):15–20, 2005.

[9] R Bennewitz, S Schär, V Barwich, O Pfeiffer, E Meyer, F Krok, B Such, J Kolodzej, and M Szymonski. Atomic-resolution images of radiation damage in kbr. *Surface science*, 474(1):L197–L202, 2001.

[10] Marcelo A. Kuroda, J. Tersoff, and Glenn J. Martyna. Nonlinear screening in multilayer graphene systems. *Phys. Rev. Lett.*, 106:116804, Mar 2011.

[11] Sujit S Datta, Douglas R Strachan, EJ Mele, and AT Charlie Johnson. Surface potentials and layer charge distributions in few-layer graphene films. *Nano letters*, 9(1):7–11, 2008.

[12] PB Visscher and LM Falicov. Dielectric screening in a layered electron gas. *Physical Review B*, 3(8):2541, 1971.

[13] Cheol-Hwan Park, Young-Woo Son, Li Yang, Marvin L Cohen, and Steven G Louie. Electron beam supercollimation in graphene superlattices. *Nano letters*, 8(9):2920–2924, 2008.

[14] Hung-Chieh Cheng, Ren-Jye Shiue, Chia-Chang Tsai, Wei-Hua Wang, and Yit-Tsong Chen. High-quality graphene p- n junctions via resist-free fabrication and solution-based noncovalent functionalization. *ACS nano*, 5(3):2051–2059, 2011.

[15] Gordon W. Semenoff. Condensed-matter simulation of a three-dimensional anomaly. *Phys. Rev. Lett.*, 53:2449–2452, Dec 1984.

[16] AH Castro Neto, F Guinea, NMR Peres, Kostya S Novoselov, and Andre K Geim. The electronic properties of graphene. *Reviews of modern physics*, 81(1):109, 2009.

[17] Cristina Bena and Gilles Montambaux. Remarks on the tight-binding model of graphene. *New Journal of Physics*, 11(9):095003, 2009.

[18] Andre K Geim and Konstantin S Novoselov. The rise of graphene. *Nature materials*, 6(3):183–191, 2007.

[19] P. R. Wallace. The band theory of graphite. *Phys. Rev.*, 71:622–634, May 1947.

[20] JC Slonczewski and PR Weiss. Band structure of graphite. *Physical Review*, 109(2):272, 1958.

[21] Stephanie Reich, Christian Thomsen, and Janina Maultzsch. *Carbon nanotubes: basic concepts and physical properties*. John Wiley & Sons, 2008.

[22] Kostya S Novoselov, Andre K Geim, SV Morozov, D Jiang, Y_ Zhang, SV Dubonos, IV Grigorieva, and AA Firsov. Electric field effect in atomically thin carbon films. *science*, 306(5696):666–669, 2004.

[23] KSA Novoselov, Andre K Geim, SVb Morozov, Da Jiang, MI Katsnelson IV Grigorieva, SV Dubonos, and AA Firsov. Two-dimensional gas of massless dirac fermions in graphene. *nature*, 438(7065):197–200, 2005.

[24] Xu Du, Ivan Skachko, Anthony Barker, and Eva Y Andrei. Approaching ballistic transport in suspended graphene. *Nature nanotechnology*, 3(8):491–495, 2008.

[25] Edward McCann, David SL Abergel, and Vladimir I Falko. Electrons in bilayer graphene. *Solid State Communications*, 143(1):110–115, 2007.

[26] Johan Nilsson, AH Castro Neto, F Guinea, and NMR Peres. Electronic properties of bilayer and multilayer graphene. *Physical Review B*, 78(4):045405, 2008.

[27] Edward McCann. Asymmetry gap in the electronic band structure of bilayer graphene. *Physical Review B*, 74(16):161403, 2006.

[28] Eduardo V Castro, KS Novoselov, SV Morozov, NMR Peres, JMB Lopes dos Santos, Johan Nilsson, F Guinea, AK Geim, and AH Castro Neto. Electronic properties of a biased graphene bilayer. *Journal of Physics: Condensed Matter*, 22(17):175503, 2010.

[29] Jeroen B Oostinga, Hubert B Heersche, Xinglan Liu, Alberto F Morpurgo, and Lieven MK Vandersypen. Gate-induced insulating state in bilayer graphene devices. *Nature materials*, 7(2):151–157, 2007.

[30] EA Henriksen and JP Eisenstein. Measurement of the electronic compressibility of bilayer graphene. *Physical Review B*, 82(4):041412, 2010.

[31] Taisuke Ohta, Aaron Bostwick, Thomas Seyller, Karsten Horn, and Eli Rotenberg. Controlling the electronic structure of bilayer graphene. *Science*, 313(5789):951–954, 2006.

[32] JW González, H Santos, M Pacheco, L Chico, and L Brey. Electronic transport through bilayer graphene flakes. *Physical Review B*, 81(19):195406, 2010.

[33] Calvin J Tabert and Elisabeth J Nicol. Dynamical conductivity of aa-stacked bilayer graphene. *Physical Review B*, 86(7):075439, 2012.

[34] MF Craciun, S Russo, M Yamamoto, Jeroen Bart Oostinga, AF Morpurgo, and S Tarucha. Trilayer graphene is a semimetal with a gate-tunable band overlap. *Nature nanotechnology*, 4(6):383–388, 2009.

[35] Chun Hung Lui, Zhiqiang Li, Kin Fai Mak, Emmanuele Cappelluti, and Tony F Heinz. Observation of an electrically tunable band gap in trilayer graphene. *Nature Physics*, 7(12):944–947, 2011.

[36] Francesco Bonaccorso, Z Sun, T Hasan, and AC Ferrari. Graphene photonics and optoelectronics. *Nature Photonics*, 4(9):611–622, 2010.

[37] P Blake, EW Hill, AH Castro Neto, KS Novoselov, D Jiang, R Yang, TJ Booth, and AK Geim. Making graphene visible. *Applied Physics Letters*, 91(6):063124–063124, 2007.

[38] M. Dorn, P. Lange, A. Chekushin, N. Severin, and JP Rabe. High contrast optical detection of single graphenes on optically transparent substrates. *Journal of Applied Physics*, 108(10):106101–106101, 2010.

[39] Javad Rafiee, Mohammad A Rafiee, Zhong-Zhen Yu, and Nikhil Koratkar. Superhydrophobic to superhydrophilic wetting control in graphene films. *Advanced Materials*, 22(19):2151–2154, 2010.

[40] D. Beysens and C. M. Knobler. Growth of breath figures. *Phys. Rev. Lett.*, 57:1433–1436, Sep 1986.

[41] Ernst Meyer, Hans Josef Hug, and Roland Bennewitz. *Scanning probe microscopy: the lab on a tip*. Springer, 2004.

[42] P Nemes-Incze, Z Osváth, K Kamarás, and LP Biró. Anomalies in thickness measurements of graphene and few layer graphite crystals by tapping mode atomic force microscopy. *Carbon*, 46(11):1435–1442, 2008.

[43] Ricardo Garcıa and Ruben Perez. Dynamic atomic force microscopy methods. *Surface science reports*, 47(6):197–301, 2002.

[44] Jacob N Israelachvili. *Intermolecular and surface forces: revised third edition*. Academic press, 2011.

[45] R. Bennewitz, AS Foster, LN Kantorovich, M. Bammerlin, C. Loppacher, S. Schär, M. Guggisberg, E. Meyer, and AL Shluger. Atomically resolved edges and kinks of nacl islands on cu (111): Experiment and theory. *Physical Review B*, 62(3):2074, 2000.

[46] Adam S Foster, Clemens Barth, and Claude R Henry. Chemical identification of ions in doped nacl by scanning force microscopy. *Physical review letters*, 102(25):256103, 2009.

[47] P. Hohenberg and W. Kohn. Inhomogeneous electron gas. *Phys. Rev.*, 136:B864–B871, Nov 1964.

[48] W. Kohn and L. J. Sham. Self-consistent equations including exchange and correlation effects. *Phys. Rev.*, 140:A1133–A1138, Nov 1965.

[49] John P. Perdew. Density-functional approximation for the correlation energy of the inhomogeneous electron gas. *Phys. Rev. B*, 33:8822–8824, Jun 1986.

[50] Ying Wu. unpublished.

[51] A. Mayer. Formulation in terms of normalized propagators of a charge-dipole model enabling the calculation of the polarization properties of fullerenes and carbon nanotubes. *Phys. Rev. B*, 75:045407, Jan 2007.

[52] Clemens Barth and Claude R Henry. Surface double layer on (001) surfaces of alkali halide crystals: a scanning force microscopy study. *Physical review letters*, 98(13):136804, 2007.

[53] Clemens Barth and Claude R Henry. Imaging suzuki precipitates on nacl: Mg 2+(001) by scanning force microscopy. *Physical review letters*, 100(9):096101, 2008.

[54] MP Delplancke-Ogletree, Min Ye, René Winand, Jean-François De Marneffe, and Robert Deltour. Influences of thermal annealing and humidity exposure on surface structure of (100) single-crystal mgo substrate. *Journal of materials research*, 14(05):2133–2137, 1999.

[55] J Estel, H Hoinkes, H Kaarmann, H Nahr, and H Wilsch. On the problem of water adsorption on alkali halide cleavage planes, investigated by secondary ion mass spectroscopy. *Surface Science*, 54(2):393–418, 1976.

[56] PB Barraclough and PG Hall. The adsorption of water vapour by lithium fluoride, sodium fluoride and sodium chloride. *Surface Science*, 46(2):393–417, 1974.

[57] M Luna, F Rieutord, NA Melman, Q Dai, and M Salmeron. Adsorption of water on alkali halide surfaces studied by scanning polarization force microscopy. *The Journal of Physical Chemistry A*, 102(34):6793–6800, 1998.

[58] Dror Sarid. *Scanning Force Microscopy*. New York: Oxford University Press, 1994.

[59] CH Lei, A. Das, M. Elliott, and J.E. Macdonald. Quantitative electrostatic force microscopy-phase measurements. *Nanotechnology*, 15(5):627, 2004.

[60] C. Staii, A.T. Johnson Jr, and N.J. Pinto. Quantitative analysis of scanning conductance microscopy. *Nano Letters*, 4(5):859–862, 2004.

[61] M. Nonnenmacher, MP Oboyle, and HK Wickramasinghe. Kelvin probe force microscopy. *Applied Physics Letters*, 58(25):2921–2923, 1991.

[62] C. Sommerhalter, T.W. Matthes, T. Glatzel, A. Jager-Waldau, and M.C. Lux-Steiner. High-sensitivity quantitative kelvin probe microscopy by noncontact ultra-high-vacuum atomic force microscopy. *Applied physics letters*, 75(2):286–288, 1999.

[63] Masao Nagase, Hiroki Hibino, Hiroyuki Kageshima, and Hiroshi Yamaguchi. Contact conductance measurement of locally suspended graphene on sic. *Applied physics express*, 3(4):045101, 2010.

[64] Cristian Staii, Alan T. Johnson, and Nicholas J. Pinto. Quantitative analysis of scanning conductance microscopy. *Nano Letters*, 4(5):859–862, 2004.

[65] JMR Weaver and David W Abraham. High resolution atomic force microscopy potentiometry. *Journal of Vacuum Science & Technology B*, 9(3):1559–1561, 1991.

[66] Tim Burnett, Rositza Yakimova, and Olga Kazakova. Mapping of local electrical properties in epitaxial graphene using electrostatic force microscopy. *Nano letters*, 11(6):2324–2328, 2011.

[67] Saidislam Kurbanov, Woo Chul Yang, and Tae Won Kang. Kelvin probe force microscopy of defects in zno nanocrystals associated with emission at 3.31 ev. *Applied physics express*, 4(2):021101, 2011.

[68] Paul Girard. Electrostatic force microscopy: principles and some applications to semiconductors. *Nanotechnology*, 12(4):485, 2001.

[69] Gavin J Jones, Asieh Kazemi, Simon Crampin, Mick Phillips, and Adelina Ilie. Surface potential variations in graphene induced by nanostructured crystalline ionic substrates. *Applied Physics Express*, 5(4):045103, 2012.

[70] R. Hoffmann. PhD thesis, University of Basel, 2001.

[71] M. Goryl, F. Buatier de Mongeot, F. Krok, A. Vevecka-Priftaj, and M. Szymonski. Leaky atomic traps: Upward diffusion of au from nanoscale pits on ionic-crystal surfaces. *Phys. Rev. B*, 76:075423, Aug 2007.

[72] R. Yakimova group. personal communication.

[73] Naokazu Kitamura, Atsushi Oshiyama, and Osamu Sugino. Atomic and electronic structures of deformed graphite sheets. *Journal of the Physical Society of Japan*, 67(11):3976–3984, 1998.

[74] Laurent Nony, Enrico Gnecco, Alexis Baratoff, Audrius Alkauskas, Roland Bennewitz, Oliver Pfeiffer, Sabine Maier, A Wetzel, Ernst Meyer, and Ch Gerber. Observation of individual molecules trapped on a nanostructured insulator. *Nano Letters*, 4(11):2185–2189, 2004.

[75] Thilo Glatzel, Lars Zimmerli, Shigeki Kawai, Ernst Meyer, Leslie-Anne Fendt, and Francois Diederich. Oriented growth of porphyrin-based molecular wires on ionic crystals analysed by nc-afm. *Beilstein journal of nanotechnology*, 2(1):34–39, 2011.

[76] Mikhail I Katsnelson. Graphene: carbon in two dimensions. *Materials today*, 10(1):20–27, 2007.

[77] Llewellyn H Thomas. The calculation of atomic fields. In *Mathematical Proceedings of the Cambridge Philosophical Society*, volume 23, pages 542–548. Cambridge Univ Press, 1927.

[78] Charles Kittel and Paul McEuen. *Introduction to solid state physics*, volume 8. Wiley New York, 1976.

[79] Neil W Ashcroft and N David Mermin. *Solid State Physics (Holt, Rinehart and Winston, New York, 1976)*. 2005.

[80] William H. Press, Saul A. Teukolsky, William T. Vetterling, and Brian P. Flannery. *Numerical Recipes in FORTRAN; The Art of Scientific Computing*. Cambridge University Press, New York, NY, USA, 2nd edition, 1993.

[81] M Salis. Thomas-fermi screening in graphene. *arXiv preprint cond-mat/0701108*, 2007.

[82] MI Katsnelson. Nonlinear screening of charge impurities in graphene. *Physical Review B*, 74(20):201401, 2006.

[83] David Necas and Petr Klapetek. Gwyddion: an open-source software for SPM data analysis. *Central European Journal of Physics*, 10:181–188, 2012.